Tunable Substrate Integrated Waveguide Bandpass Filter and Amplitude Tuner Based on Microwave Liquid Crystal Technology

Dem Fachbereich Elektrotechnik und Informationstechnik
der Technischen Universität Darmstadt
zur Erlangung des akademischen Grades eines
Doktor-Ingenieurs (Dr.-Ing.)
genehmigte Dissertation

von

Ananto Eka Prasetiadi, M.T.
Geboren am 30.12.1989 in Palo Alto, CA, den USA

Referent:	Prof. Dr.-Ing. Rolf Jakoby
Korreferent:	Prof. Dr.-Ing. Michael Höft

Tag der Einreichung:	20.06.2017
Tag der mündlichen Prüfung:	13.09.2017

D17
Darmstadt 2017

Erklärung laut 9 PromO

Ich versichere hiermit, dass ich die vorliegende Dissertation allein und nur unter Verwendung der angegebenen Literatur verfasst habe. Die Arbeit hat bisher noch nicht zu Prüfungszwecken gedient.

Darmstadt, den 20.06.2017

Hereby I declare that I authored the present PhD-thesis alone and exclusively under the use of the literature denoted. The present PhD-thesis has by now not been used in any exam.

Darmstadt, June 20, 2017

PREFACE

This dissertation summarizes my research at the Institute of Microwave Engineering and Photonics (IMP), Technische Universität Darmstadt, Darmstadt, Germany. The work cannot be accomplished without help of the colleagues and friends.

First of all, I would like to acknowledge my supervisor, Prof. Dr.-Ing Rolf Jakoby, who gave me an opportunity to do the research at IMP. His advice and guidance helped me to finish the dissertation and in general, to be a better researcher.

I would like to express my appreciation to the liquid crystal (LC) resarch group at IMP: Matthias Jost, Matthias Nickel and Roland Reese, who also helped reviewing this dissertation. I also would like to thank Dr. Alexander Gäbler, Dr. Onur Hamza Karabey, Dr. Sebastian Strunck, Dr. Christian Weickhmann, Tobias Franke and Wenjuan Hu for the fruitful discussions and supports during my time at IMP, TU Darmstadt. Furthermore, the realization of the devices in this work cannot be done without the assistance from Peter Kießlich, Andreas Semrad, Silke Schober and Karin Boye.

Some parts of this work were also a cooperation with several institutions. Therefore, I would like to thank the following colleagues for the excellent teamwork at the Liquida K Project:

- Bärbel Schulz, Andreas Heunisch and Dr. Torsten Rabe from the Federal Institute for Materials Research and Testing (BAM),
- Matthias Quibeldey and Dr. Rüdiger Follmann from IMST GmbH,
- Dr. Anke Pagels-Kerp from the German Aerospace Center (DLR).

I also would like to express my gratitude to the German Academic Exchange Service (DAAD) and the Indonesian-German Scholarship Program for the financial support during my study in Germany.

Last but not least, my special thanks are extended to my family and Indonesian friends in Darmstadt, who always support and help me during my stay in Germany.

Darmstadt, 20.06.2017 Ananto Eka Prasetiadi

ABSTRACT

Tunable microwave devices are needed to fulfill the requirement of the modern wireless systems. In this work, two major devices have been developed: a tunable filter and an amplitude tuner. Specifically synthesized liquid crystals (LC) have been employed as tuning elements for those devices due to their low loss property at frequency bands above 10 GHz, where printed circuit board (PCB) and low temperature co-fired ceramic (LTCC) technologies are employed for the hardware implementation.

By inserting the LC inside a filter structure, a tunable filter is obtained, so that the center frequency can be altered by using either magnetic alignment or electric biasing. To achieve a low loss filter with a high quality factor (Q-factor) and maintain the compactness, substrate integrated waveguide (SIW) structure is combined with the LC as the tuning element. Consequently, some magnetically aligned structures, which are implemented by using PCB technology, are verified first because of their simplicity. To begin with, a single resonator, which is the important constituent of the filter, is designed, fabricated and measured, resulting in a device with unloaded Q-factor of 102 to 105.6 and a tuning range of 412 MHz around a frequency of 22 GHz. In addition, 3 resonators are cascaded, forming a 3-pole Chebyshev filter. Following results are yielded: center frequency range of 21.45 to 22.06 GHz, insertion loss of 6 dB and fractional bandwidth of 2.81 to 3.54 %. Furthermore, electrically biasing systems for these PCB-based devices, have also been investigated by using glass fabrication technique. A simple demonstrator, which utilizes a tunable delay line structure, provides the following results: FoM of 32 °/dB and a response time of 5 s.

In contrary to the PCB technology, the LTCC technology enables the integration of both the microwave and biasing structures. A single resonator is fabricated first with unloaded Q-factor of 68 to 100, a tuning range of 840 MHz (30.16 to 31 GHz) and a response time faster than 2 s. A 3-pole Chebyshev filter is also fabricated with the following results: operating frequency of 29.4 to 30.1 GHz, fractional bandwidth of 11.2 to 11.6 % and insertion loss 2 to 4 dB.

The second device, which is the amplitude tuner, changes the amplitude of the input signal in dependence of an applied voltage. For this purpose, tunable resistors and varactors can be employed. However, with the usage of LC, a device with a lower power consumption can be obtained at frequencies above 10 GHz. The proposed amplitude tuner uses the interference concept, splitting the input signal into two branches and at the end, combining it together again at the output port. By using a tunable LC phase shifter in one of the branches, the output amplitude is controllable. Therefore, the required subcomponents are the phase shifters, power divider and combiner as well as transitions. The amplitude tuner is fabricated with the LTCC technology, yielding a device with amplitude range of 11 to 30 dB at around 30 GHz. Thus, an LC-based amplitude tuner operating at the lower millimeter wave band is achieved for the first time.

KURZFASSUNG

Steuerbare Mikrowellenkomponenten erlauben eine flexible Anpassung in modernen drahtlosen Systemen. Zwei Komponenten wurden in dieser Arbeit entwickelt: ein steuerbares Filter und ein Amplitudensteller. Als Steuerelement wurden Flüssigkristalle (engl. *liquid crystal*, LC) speziell synthetisiert für den Mikrowellenbereich eingesetzt, da diese LCs niedrige Verluste für Frequenzen über 10 GHz aufweisen. Die Komponenten wurden in *Printed Circuit Board* (PCB) und *Low Temperature Co-fired Ceramic* (LTCC) Technologie realisiert.

Durch Einfügen von LC in der Filterstruktur wird ein steuerbares Filter ermöglicht. Hierbei ist die Mittenfrequenz vom Filter sowohl mit einem magnetischen als auch elektrischen Netzwerk steuerbar. Um ein verlustarmes Filter mit hoher Güte (Q-Faktor) zu erreichen und gleichzeitig die Kompaktheit beizubehalten, wurde ein *Substrate Integrated Waveguide* (SIW) mit dem LC als Steuerelement kombiniert. Um dieses neuartigen Filter zu untersuchen, wurden Zunächst einige einfache PCB-Strukturen nur mit magnetischen Biasing entwickelt. Dazu wurde ein einzelner Resonator entworfen, hergestellt und gemessen. Die Ergebnisse sind: Güte von 102 bis 105.6, eine Steuerbarkeit von 412 MHz bei einer Arbeitsfrequenz von 22 GHz. Zusätzlich wurde 3 Resonatoren miteinander kaskadiert, die ein 3-pol Tschebyscheff-Filter bilden. Folgende Ergebnisse wurden erzielt: Arbeitsfrequenzbereich von 21.45 bis 22.06 GHz, Verlust von 6 dB und Bandbreite von 2.81 bis 3.54 %. Als erster Test wurde auch ein elektrisches Ansteuernetzwerk für diese PCB-basierten Komponenten anhand eines einfachem Verzögerungsleitung (Phasenschieber) hergestellt und untersucht mit folgendem Ergebniss: FoM von 32 °/dB und Schaltzeit von 5 s.

Im Gegensatz zur PCB-Technologie, hat die LTCC-Technologie den Vorteil, die Ansteuersschaltung einfacher in die SIW-Filterstruktur integrieren zu können. Ein einzelner Resonator wurde hierzu Zunächst hergestellt: Güte von 68 bis 100, Steuerbereich von 840 MHz (30.16 bis 31 GHz) und Schaltzeit besser als 2 s. Anschließend erfolgte die Realisierung eines 3-pol Tschebyscheff-Filter mit folgenden Charakteristika: Arbeitsfrequenz von 29.4 bis 30.1 GHz, Bandbreite von 11.2 bis 11.6 % und Verluste von 2 bis 4 dB.

Die zweite Komponente, der Amplitudensteller, ändert die Amplitude des Eingangssignals abhängig von der Steuerspannung. Für diese Zweck können sowohl steuerbare Widerstände als auch Varaktoren verwendet werden. Um ein Gerät mit geringer Leistungsaufnahme bei Frequenzen über 10 GHz zu erhalten, sind LC-basierte Komponenten besonders vielversprechend. Der vorgeschlagene Amplitudensteller verwendet das Interferenzkonzept, welches das Eingangssignal in zwei Zweige aufteilt und wieder am Ausgangsport addiert. Durch die Verwendung eines steuerbaren LC-Phasenschiebers in einem der Zweige ist die Ausgangsamplitude steuerbar. Diese Amplitudenstellerteilkomponenten wurden entworfen: Phasenschieber, Leistungsteiler und Kombinierer sowie die Übergänge. Der Amplitudensteller wurde mit der Hilfe der LTCC-Technologie hergestellt mit einem Amplitudeneinstellbereichs von 11 bis 30 dB bei einer Arbeitsfrequenz um 30 GHz. Damit wurde ein LC-basierter Amplitudenschieber im unteren Millimeterwellenband zum ersten Mal implementiert.

CONTENTS

1

INTRODUCTION

Motivation

Wireless systems play an important role nowadays, for instance in communication, electronic warfare and radar systems, and will be expanding in the future. Since the requirement of the wireless systems become more complex, for example for supporting multiple wireless services [ZYP$^+$07], tunable microwave devices are needed in their RF frontends for reconfigurability. By using tunable devices, their device parameters can be controlled, for example operating frequency, their amplitude or phase, resulting in multipurpose microwave frontend transceivers.

A typical frontend transceiver is depicted in Fig. 1.1 [Dre10,MNS$^+$16]. As can be seen in Fig. 1.1, tunable microwave devices have a potential to reduce the size and complexity of the transceiver. For example, a tunable bandpass filter can replace a filter bank, which contains n fixed bandpass filters with different center frequencies $(f_1,f_2,...,f_n)$ and switches. This is important when lightweight components are desirable as in satellite systems.

To obtain a tunable device, tuning elements have to be integrated into a non-tunable device. Several prominent tuning elements have been applied in constructing a tunable microwave component, for example mechanical tuning elements [SA51], ferrites [CD85], semiconductors [ASE10], microelectromechanical systems (MEMS) [RER$^+$09] and functional materials such as ferroelectrics [ZSM$^+$11] and liquid crystals. In the early years of microwave technology, mechanically tunable devices are commonly found. However, adding a mechanical tuning element makes a bulky device, which is unpractical. The same problem also occurs for ferrite materials, for example yttrium-iron-garnet (YIG), because magnets are needed for tuning.

Electrical tuning elements offer smaller devices and much less power consumption compared to the aforementioned tuning elements. Semiconductor based elements, such as PIN diodes or semiconductor-based varactors, offer a low production cost, fast tuning speed and high tunability. Nevertheless, they are lossy (especially at high frequency), non-linear and have a low power handling capability. On the other hand, MEMS has a better property in term of losses. Due to the small moving elements as the most important part of its operational principle, MEMS suffers from realibility issue from enviromental conditions and requires a complex packaging. Another technology which

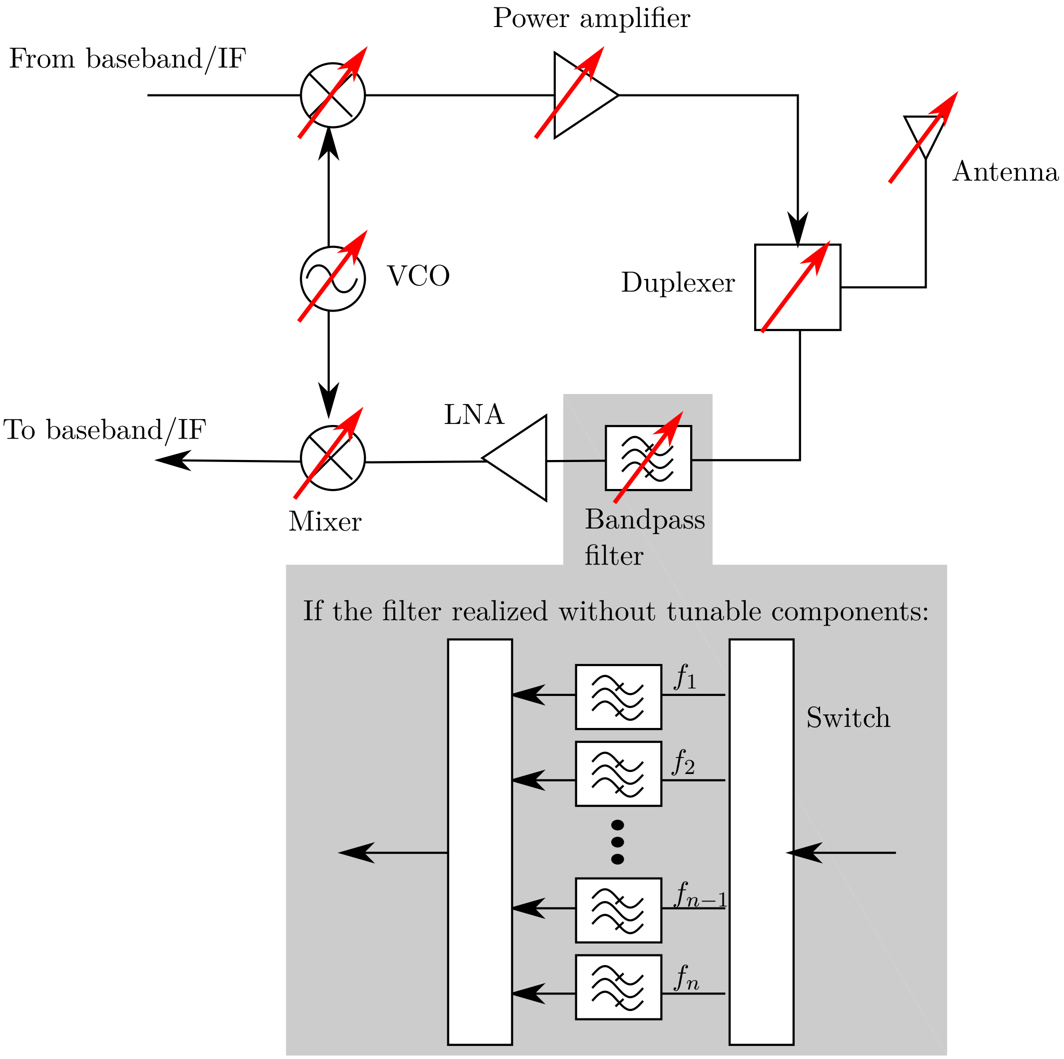

Figure 1.1.: Typical tunable frontend wireless transceiver. The usage of tunable components can reduce the size and complexity of the transceiver significantly, replacing, for example, conventional filter banks as depicted above.

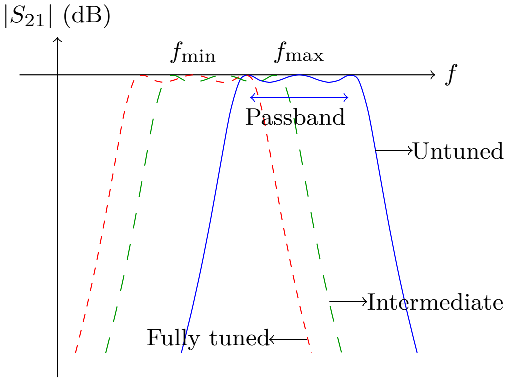

Figure 1.2.: Operation principle of a filter with a tunable center frequency, from f_{max} to f_{min}.

can be used is ferroelectric material, such as barium strontium titanate (BST), where its permittivity changes when biasing voltage is applied. Despite its good linearity and power handling capability, this material has a high losses for applications above 10 GHz.

Liquid crystal (LC), specifically synthesized for microwaves, has been utilized since 2002 to create tunable microwave devices such as phase shifters [WLJ02], filters [GGK$^+$10, FGPJ14], antennas [Kar14] and polarizers [SKGJ12]. The technology is similar to the liquid crystal display (LCD) technology, which is commonly used in our everyday life. Tuning can be achieved through LC molecular orientation which has a different relative permittivity in each orientational state. For tuning purpose, electric and magnetic fields can be employed, making this technology flexible. LC exhibits continuous tuning property unlike PIN Diode [ASE10] or MEMS switch [SAE11]. Moreover, the loss is decreasing with increasing operating frequency of the device, typically suitable above 10 GHz. This makes LC a promising tuning element since the future communication and wireless systems will use the available frequency band at higher frequency, for example in the millimeter wave and terahertz range [WJCL13].

Due to its advantages, LC is chosen for realizing tunable microwave devices in this work. Two devices will be presented: a tunable filter and an amplitude tuner.

Tunable Liquid Crystal Filter Based on Substrate Integrated Waveguide Structure

As already seen in Fig. 1.1, filter is an important component in the modern communication systems. A filter selects signals in a certain frequency band (passband area) and rejects unwanted signals outside the passband, called stopband. A tunable filter can be created by inserting some tuning elements into a fixed filter. Since most of them are lossy, insertion of these tuning elements degrades the quality of the filter, which can be described by its quality factor (Q-factor). Specifically synthesized LCs exhibit low loss properties at microwaves and millimeter waves, which make them promising tuning elements for a filter operating at high frequency bands.

Apart from the tuning element, the structure or topology of the filter itself should be considered, whether using planar or nonplanar structure. For the most of planar structure, microstrip line (MSL) structures are commonly exploited, which can be fabricated by similar process as in display technology [Kar14]. Many kind of filters and resonators (which are the basic components to realize the filters) can be realized using this MSL technique. For example, the firstly reported LC-based microwave filter [BML$^+$06] is using this technology. MSL-based dual behavior resonators, which have transmission pole and zero concurrently, are employed for the filter. The other resonators, such as microstrip patch [YFB$^+$12], periodically loaded line [GGK$^+$10], dual ring resonator [MFBJ10] and parallel coupled line resonator [YMS12], have also been reported using this MSL technique. However, the Q-factor of the planar resonators are relatively low, typically not exceeding a Q of 40 due to system-inherently high losses of planar structures.

On the other hand, nonplanar structures, such as waveguides, have inherently higher Q-factors compared to the planar structures. The size of waveguide filters are usually bulky so that the filters are not preferable for certain application where size is important, such as in a user mobile terminal. The usage of LC in a waveguide structure has also been reported [FGPJ14] and the Q-factors are better than 170 around 20 GHz.

In recent years, substrate integrated waveguide (SIW) structures have attracted many researchers due to their trade-off properties between conventional planar and waveguide structures. They have lower Q-factors and higher losses compared to the waveguides, but higher Q-factors and lower losses compared to planar structures by the potential of similar low cost fabrication [CW14]. For the fabrication, these structures can be implemented by using printed circuit board (PCB) or low temperature co-fired ceramic (LTCC) technology which are commonly known as the fabrication techniques for planar structures.

Several attempts have been made to realize tunable SIW filter, for example by using microelectromechanical systems (MEMS) [SAE11] or tunable varactor technology [SMTB11], which yielded Q-factors ranging from 40–150 in the range of 1–3 GHz. Combination of SIW structure with LC as tuning element, which has not been implemented up to now, will yield a tunable device with higher Q-factor above 10 GHz. In this work, the combination of both technologies is proposed which uses PCB and LTCC technology.

Liquid Crystal Based Amplitude Tuner

A lot of the current researches in microwave LC focus on tunable phase shifters and their applications, for example in tunable phased array antennas or smart antennas [KGSJ12, WNG$^+$13b, HKG$^+$14, SGK$^+$15, JSH$^+$15]. An illustration of a phased array antenna is depicted in Fig. 1.3. Adding a tunable phase shifter before each antenna element can modify the beam direction ϕ_0 of the array system. Such a phase shifter

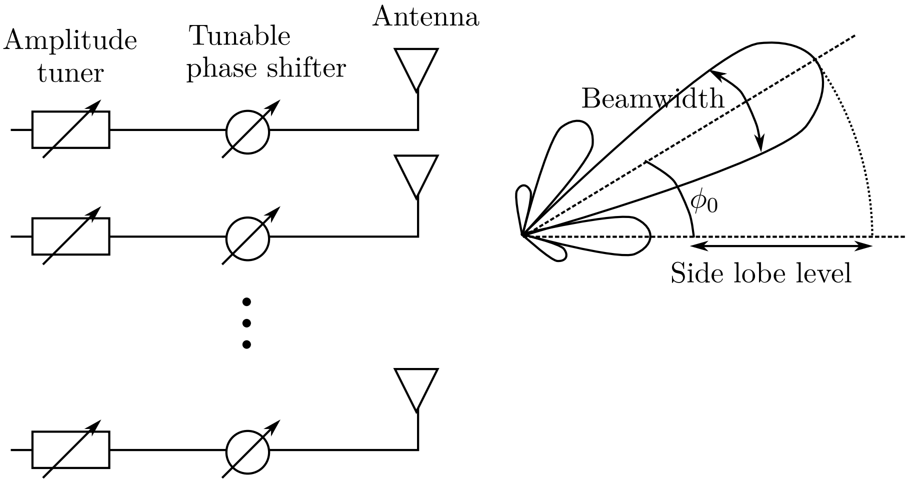

Figure 1.3.: An example of a phased array antenna system with a typical radiation pattern. Tunable phase shifter and amplitude tuner are added in each antenna element. By tuning both element, the radiation pattern can be altered, for example the beam direction ϕ_0, beamwidth and sidelobe level.

enables us to perform an electronically beamsteering of the antenna. Especially in high frequency, LC is preferable for this purpose since it exhibits continuous tuning property.

In some applications, phase tuning alone is not sufficient. The amplitude of the signal in each array can be tuned as well in order to achieve an analog beamforming, including beamsteering. By amplitude tuning, the unwanted sidelobes of the phased array antenna, as well as the beamwidth, can be controlled (see Fig. 1.3), for example by using uniform, Dolph-Chebyshev or binomial amplitude distribution [Bal12]. Therefore, a circuit that change the amplitude of the signal electronically is desired, i.e. an amplitude tuner.

Besides beamforming application in smart antenna systems, amplitude tuner is also commonly used in a clutter cancellation circuit for radar or life detection systems [SL02, TOD14, CKL$^+$12]. In a life detection system, for example, the system transmit microwave signals to the objects, so that backscattered signals can be analyzed, as can be seen in Fig. 1.4. The backscattered signals are phase-modulated by human breathing and heartbeat vibration, enabling the detection of life signs. However, the clutters have larger influences on the backscattered signals. In [CKL$^+$12], it is shown that the detection sensitivity can be enhanced by using a clutter cancellation system, which operates at millimeter wave band. As a subcomponent of the system (see Fig. 1.4), a high frequency amplitude tuner is important.

There are two approaches to construct an amplitude tuning device: active and passive. Active devices, i.e. microwave amplifiers, can be exploited for those purpose. However, the amplifiers are expensive especially for array applications with hundred or even thousand antenna elements. Instead of giving power gain, amplitude tuning also can be achieved by reducing the amplitude of input signal using a passive device or variable

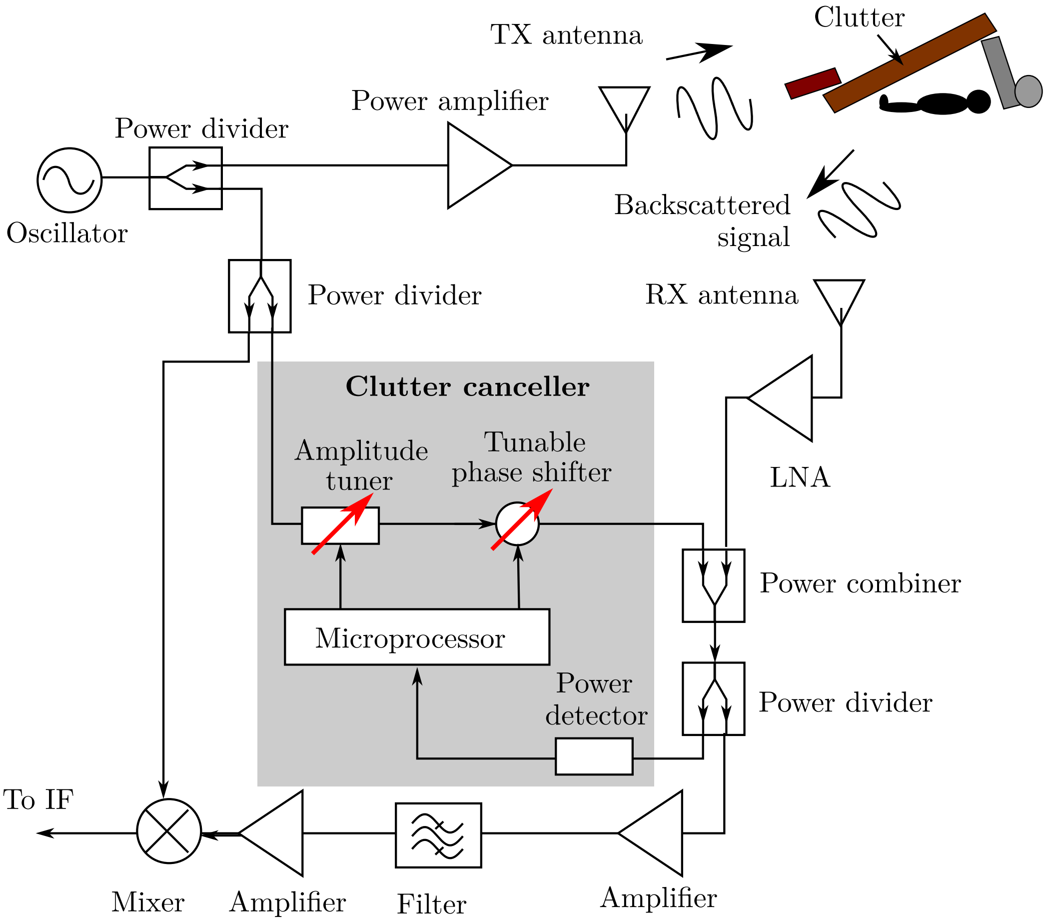

Figure 1.4.: A typical block diagram for a clutter cancellation system [TOD14, CKL+12], which uses amplitude tuner and tunable phase shifter.

attenuator. The common method is to use a tunable resistor, which can be implemented by using PIN diodes or field-effect transistors (FET) [Wal94, SZ05]. However, these tunable resistors need biasing current in order to tune the resistance, leading to a nonzero power consumption.

Recent researches show tunable capacitors or varactors can be employed to make an amplitude tuner [TW02, BG12, CC15]. To the best of the author's knowledge, most of those devices are working in a low frequency band, typically below 12 GHz. These are not suitable for millimeter wave applications. LC is a potential candidate to replace these tuning elements due to its low loss property at higher operating frequencies. Therefore, a planar amplitude tuner using LC as the tuning element is presented for the first time. The amplitude tuner is fabricated in LTCC technology.

Thesis Outline

After this introduction chapter, this dissertation is organized as follows.

Chapter 2 will focus on the introduction of the liquid crystal theory. A working principle about liquid crystal for microwave applications will be presented.

The discussion of the LC-based tunable SIW filters and amplitude tuner will be divided by the fabrication technology: PCB in Chapter 3 and LTCC in Chapter 4. Chapter 3 provides the fundamental investigations of the tunable SIW filters, starting from a single resonator to 3 resonators (or 3-pole) bandpass filter. For tuning purpose, LC alignment with magnets is employed, which is quite simple for a proof of concept. However, an electrical biasing method is preferred for a more compact device. Therefore, some efforts have been made to include the electric biasing system in the PCB-based LC-filled SIW filter.

Another alternative to include the electric biasing system is by using LTCC technology, providing more realible structure compared to the PCB. In Chapter 4, two components are realized by using this LTCC technology: the SIW filter and amplitude tuner. The work on LTCC devices is a part of the Liquida K Project, which is a cooperation between the Institute of Microwave Engineering and Photonics of TU Darmstadt, the German Aerospace Center (DLR), the German Federal Institute for Materials Research and Testing (BAM), and IMST GmbH.

To conlcude all of the works, Chapter 5 will be made as the last chapter. The significant results from each chapter will be presented. In addition, some outlooks for further developments of this work will be given at the end.

2

FUNDAMENTALS OF LIQUID CRYSTAL (LC) MATERIALS FOR MICROWAVE APPLICATIONS

As we know, materials in nature can be classified into different phases or states, for example, solid, liquid and gas. A solid state material has strong intermolecular forces which make the molecules stay close together. The molecules are ordered in certain positions and have the tendency to orient to a specific direction. These positional and orientational order properties can be found in crystals. Unlike solid materials, liquids have weaker intermolecular forces, making their molecules movable. Therefore, liquid molecules do not have any regular arrangement. Liquids also adapt their form into the form of the container. Gases have similar properties as liquids but their molecules are well separated so that they fill the container entirely. The phase of a material can change, depending on its pressure and temperature.

Intermediate phase or mesophase between those three categories may also exist. Liquid crystal is one of them which lies between the solid and liquid state. It can flow like a liquid but at the same time its molecules have a certain arrangement like a crystal. The molecules may have a disk-like shape (also called discotic) or an elongated rod-like shape (calamitic) with long and short axes. The last one has an important role in order to make a tunable microwave device. In this chapter, the most important physical properties are explained (Section 2.1) as well as the liquid crystal response to the external electric and magnetic fields (Section 2.2). These responses are important for tuning purpose. The possible tuning methods are discussed in Section 2.3. Finally, some examples of liquid crystal based microwave devices are given in Section 2.4.

2.1 DIRECTOR AND ORDER PARAMETER OF LIQUID CRYSTAL

The phase of the liquid crystal material depends on the temperature. The liquid crystal, which possess this property, is called thermotropic liquid crystal. The liquid crystal phase is formed between the melting point T_m and clearing point T_c. Below T_m, the phase of the matter will be solid with regular arrangement (positional and orientational order). On the other side, the phase of matter will be totally isotropic if the temperature is above T_c. There, no positional or orientational order are present. In-between both

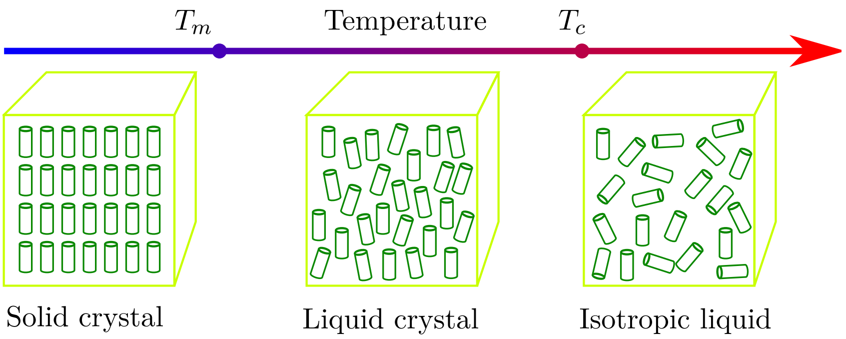

Figure 2.1.: Phase schematic of LC material, using rod-like shape representation [YW06].

phases, liquid crystals have no positional order like the isotropic liquid[1] but still show an orientational ordering property like in solid crystal. This state of liquid crystal is called nematic phase, which is the simplest and most common form of liquid crystal. Most of the works on tunable microwave devices based on liquid crystal are using nematic liquid crystal. In this work, the term liquid crystal (LC) refers to this nematic phase, having rod-like molecules. The molecular arrangement of each phase can be seen in Fig. 2.1 [YW06].

Regarding LC, there are two terms which need to be explained: the director and the order parameter. The LC director $\vec{n}$ is a unit vector, describing the preferred direction of LC molecules along the longer axis in a small volume, which is illustrated in Fig. 2.2a. The molecules themself may be moving due to thermal motion, for example orienting in the direction of $\vec{a}$ as shown in Fig. 2.2b [Kar14]. Nevertheless, the time-averaged direction is the same.

The order parameter S describes quantitatively how the LC is arranged. If the materials are highly ordered like in a solid crystalline structure, the value of S should be 1. The other extreme value of S is 0 when there is no orientational order as in the isotropic liquid. Average values of a second order Legendre polynomial P_2 match to this requirement, so that the order parameter S can be defined as [YW06]:

$$\begin{aligned} S &= \langle P_2\left(\cos(\theta)\right)\rangle = \left\langle \frac{1}{2}\left(3\cos^2(\theta)-1\right)\right\rangle \\ &= \frac{\int_0^\pi \left(\frac{1}{2}(3\cos^2(\theta)-1)f(\theta)\sin(\theta)\right)d\theta}{\int_0^\pi \left(f(\theta)\sin(\theta)\right)d\theta}, \end{aligned} \tag{2.1.1}$$

where θ is the angle between the director $\vec{n}$ and the direction of a molecule $\vec{a}$ (see Fig. 2.2b). $f(\theta)$ is an orientational distribution function. The LC used in this work depends only on the polar angle θ, not on the azimuthal angle ϕ. Thus, this kind of LC

---

[1] Liquid crystals may also have partial positional order, which means the molecules are situated in some layered structures. This state is called smectic phase. This type of liquid crystal is beyond the scope of this dissertation since it is untunable.

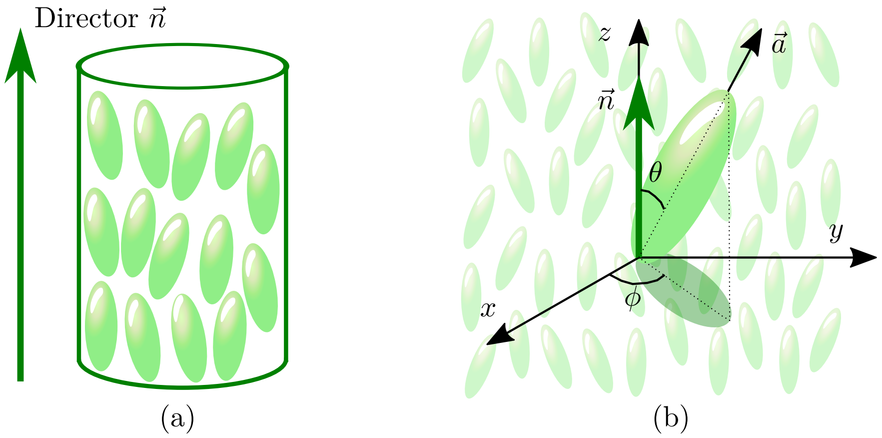

Figure 2.2.: (a) The concept of LC director $\vec{n}$. (b) A model of a liquid crystal molecule in cartesian coordinate xyz orienting in the direction of $\vec{a}$. The director $\vec{n}$ itself orienting in the direction of z and create an angle θ to the longer axis of the LC. The molecule has an azimuthal angle of ϕ.

is called an uniaxial material. Note, also the sign of the director ($\vec{n}$ or $-\vec{n}$) brings no physical difference [SS74].

The value of order parameter S depends on the temperature. This is described by Landau-de Gennes and Maier-Saupe theory. The details can be found on [YW06], [SS74] which is beyond the scope of this work.

2.2 ELECTROMAGNETIC PROPERTIES OF LIQUID CRYSTAL

Dielectric Properties of LC

As dielectric materials, the most important property of LC for microwave applications is the relative permittivity ε_r. It is related to the polarizability of the dielectric material as a response to the applied external electric field. Macroscopically, the electric polarization $\vec{P}$ is related to the molecular material polarizability tensor $\overset{\leftrightarrow}{\alpha}_p$ and internal field constant tensor $\overset{\leftrightarrow}{K}$ [Göl10]:

$$\vec{P} = N\overset{\leftrightarrow}{\alpha}_p\overset{\leftrightarrow}{K}\vec{E}, \tag{2.2.1}$$

where N is the molecular number density and both tensors can be expressed as followings:

$$\overset{\leftrightarrow}{\alpha}_p = \begin{bmatrix} \alpha_{p,\perp} & 0 & 0 \\ 0 & \alpha_{p,\perp} & 0 \\ 0 & 0 & \alpha_{p,\parallel} \end{bmatrix} \tag{2.2.2}$$

$$\overset{\leftrightarrow}{K} = \begin{bmatrix} K_\perp & 0 & 0 \\ 0 & K_\perp & 0 \\ 0 & 0 & K_\parallel \end{bmatrix}. \tag{2.2.3}$$

The symbol $\perp$ and $\parallel$ denote the perpendicular and parallel to the longer molecular axis. Since both of them correspond to the molecular axis $\vec{a}$ (see Fig. 2.2b), these tensors could be aligned to the cartesian coordinates xyz by using the rotation matrix R:

$$R = \begin{bmatrix} \cos(\theta)\cos(\phi) & -\sin(\phi) & \sin(\theta)\cos(\phi) \\ \cos(\theta)\sin(\phi) & \cos(\phi) & \sin(\theta)\sin(\phi) \\ -\sin(\theta) & 0 & \cos(\theta) \end{bmatrix}, \tag{2.2.4}$$

so that:

$$\vec{P} = NR\overset{\leftrightarrow}{\alpha}_p\overset{\leftrightarrow}{K}R^{-1}\vec{E}. \tag{2.2.5}$$

Another equation relates the macroscopic electric polarization $\vec{P}$ with the electric field $\vec{E}$ (see [Ell93], [Poz11]):

$$\vec{P} = \varepsilon_0\chi_e\vec{E}. \tag{2.2.6}$$

χ_e or $\overset{\leftrightarrow}{\chi}_e$ in a tensor form for anisotropic materials is called electric susceptibility. By multiplying R, $\overset{\leftrightarrow}{\alpha}_p$, $\overset{\leftrightarrow}{K}$ and R^{-1} from Eq. 2.2.5 and comparing to Eq. 2.2.6, it is clear that this electric susceptibility of LC depends on the orientation angle θ of each molecule. By averaging and using Eq. 2.1.1, the variable ϕ from Eq. 2.2.4 is cancelled out and the electric susceptibility tensor can be rewritten as [YW06, Kar14]:

$$\left\langle \overset{\leftrightarrow}{\chi}_e \right\rangle = \frac{N}{3\varepsilon_0} \begin{bmatrix} \begin{matrix}\alpha_{p,\perp}K_\perp(2+S)+\\ \alpha_{p,\parallel}K_\parallel(1-S)\end{matrix} & 0 & 0 \\ 0 & \begin{matrix}\alpha_{p,\perp}K_\perp(2+S)+\\ \alpha_{p,\parallel}K_\parallel(1-S)\end{matrix} & 0 \\ 0 & 0 & \begin{matrix}\alpha_{p,\perp}K_\perp(2-2S)+\\ \alpha_{p,\parallel}K_\parallel(1+2S)\end{matrix} \end{bmatrix}. \tag{2.2.7}$$

By knowing the electric susceptibility, the relative permittivity ε_r of a material can be obtained by $\varepsilon_r = 1 + \chi_e$. This relation is only valid for isotropic materials which have ε_r and χ_e in a scalar form. For anisotropic materials, we can recall the definition of the dielectric displacement $\vec{D}$ [Poz11]:

$$\vec{D} = \varepsilon_0\vec{E} + \vec{P} = \varepsilon_0\left(\overset{\leftrightarrow}{I} + \overset{\leftrightarrow}{\chi}_e\right)\vec{E} = \varepsilon_0\overset{\leftrightarrow}{\varepsilon}_r\vec{E}, \tag{2.2.8}$$

with $\overset{\leftrightarrow}{I}$ being the identity matrix tensor. Hence:

$$\left\langle \overset{\leftrightarrow}{\varepsilon_r} \right\rangle = \left\langle \overset{\leftrightarrow}{I} + \overset{\leftrightarrow}{\chi_e} \right\rangle$$
$$= \begin{bmatrix} \begin{matrix} 1 + \frac{N}{3\varepsilon_0}(\alpha_{p,\perp}K_\perp(2+S) \\ +\alpha_{p,\parallel}K_\parallel(1-S)) \end{matrix} & 0 & 0 \\ 0 & \begin{matrix} 1 + \frac{N}{3\varepsilon_0}(\alpha_{p,\perp}K_\perp(2+S) \\ +\alpha_{p,\parallel}K_\parallel(1-S)) \end{matrix} & 0 \\ 0 & 0 & \begin{matrix} 1 + \frac{N}{3\varepsilon_0}(\alpha_{p,\perp}K_\perp(2-2S) \\ +\alpha_{p,\parallel}K_\parallel(1+2S)) \end{matrix} \end{bmatrix}. \tag{2.2.9}$$

From Eq. 2.2.9, we have two different values for the relative permittivity, which could be written as:

$$\varepsilon_{r,\perp} = 1 + \frac{N}{3\varepsilon_0}\Big(\alpha_{p,\perp}K_\perp(2+S) + \alpha_{p,\parallel}K_\parallel(1-S)\Big) \tag{2.2.10}$$

and

$$\varepsilon_{r,\parallel} = 1 + \frac{N}{3\varepsilon_0}\Big(1 + \alpha_{p,\perp}K_\perp(2-2S) + \alpha_{p,\parallel}K_\parallel(1+2S)\Big). \tag{2.2.11}$$

The difference between these values is called anisotropy [YW06],

$$\Delta\varepsilon_r = \varepsilon_{r,\parallel} - \varepsilon_{r,\perp} = \frac{N}{\varepsilon_0}\Big(\alpha_{p,\parallel}K_\parallel - \alpha_{p,\perp}K_\perp\Big)S, \tag{2.2.12}$$

which is proportional to the order parameter S defined in Eq. 2.1.1.

The material permittivity itself may have a complex value: $\varepsilon = \varepsilon' - j\varepsilon''$. The additional imaginary part represents the material losses or heat dissipation caused by damping in vibration of the dipole moment. The losses cannot be distinguished from the conductor losses mechanism, which is represented by the material conductivity σ. From following Maxwell's equation:

$$\nabla \times \vec{H} = j\omega\vec{D} + \vec{J} = j\omega\left(\varepsilon' - j\left(\varepsilon'' + \frac{\sigma}{\omega}\right)\right)\vec{E}, \tag{2.2.13}$$

the ratio between the imaginary and the real part can be defined as loss tangent ($\tan\delta$), which is commonly used to describe the losses of the material in microwave applications [Poz11]:

$$\tan\delta = \frac{\omega\varepsilon'' + \sigma}{\omega\varepsilon'}. \tag{2.2.14}$$

For LC, $\tan\delta$ also shows anisotropic properties as presented in [Göl10]. Typically, the loss tangent at perpendicular state $\tan\delta_\perp$ is higher than for the parallel state $\tan\delta_\parallel$. This loss decreases with increasing frequency, which makes the LC interesting for high frequency applications, typically above 10 GHz [Kar14].

Magnetic Properties of LC

LC also exhibits anisotropic magnetic properties. When a magnetic field $\vec{H}$ is applied to the material, the molecules have a magnetic polarizability $\overset{\leftrightarrow}{\kappa}$ [Göl10]:

$$\overset{\leftrightarrow}{\kappa} = \begin{bmatrix} \kappa_\perp & 0 & 0 \\ 0 & \kappa_\perp & 0 \\ 0 & 0 & \kappa_\parallel \end{bmatrix}. \tag{2.2.15}$$

$\kappa_\perp$ and $\kappa_\parallel$ represent the magnetic polarizability at the perpendicular and parallel state, respectively. Eq. 2.2.15 is defined according to the molecular axis $\vec{a}$, however, it can be transformed into xyz axes using rotation matrix R from Eq. 2.2.4.

Similar to the electric properties, the magnetic susceptibility tensor $\overset{\leftrightarrow}{\chi_m}$ can be defined as:

$$\overset{\leftrightarrow}{\chi_m} = N\overset{\leftrightarrow}{\kappa} = N \begin{bmatrix} \kappa_\perp + \frac{1}{3}(1-S)\Delta\kappa & 0 & 0 \\ 0 & \kappa_\perp + \frac{1}{3}(1-S)\Delta\kappa & 0 \\ 0 & 0 & \kappa_\perp + \frac{1}{3}(2S+1)\Delta\kappa \end{bmatrix}, \tag{2.2.16}$$

with:

$$\Delta\kappa = \kappa_\parallel - \kappa_\perp. \tag{2.2.17}$$

Therefore, the anisotropy could be defined as [YW06]:

$$\Delta\chi_m = \chi_{m,\parallel} - \chi_{m,\perp} = N\Delta\kappa S. \tag{2.2.18}$$

The value of $\Delta\chi$ is usually positive, while the values of $\chi_{m,\parallel}$ and $\chi_{m,\perp}$ are small and negative (magnitude around 10^{-5} in SI units [YW06]). Therefore, the relative permeability μ_r in tensor form,

$$\overset{\leftrightarrow}{\mu_r} = \overset{\leftrightarrow}{\chi_m} + \overset{\leftrightarrow}{I}, \tag{2.2.19}$$

is close to the identity matrix tensor $\overset{\leftrightarrow}{I}$. Athough the anisotropy is negligible, this property can be utilized for magnetic alignment of the LC molecule, resulting in an orientation change so that the relative permittivity ε_r experienced by microwave fields is altered.

2.3 ALIGNMENT METHODS OF LIQUID CRYSTAL

The relative permittivity (and also permeability) tensor of LC described in Sec. 2.2 is defined for the director $\vec{n}$ aligned towards the z-axis. For arbitrary orientation of the director $\vec{n}$, the tensor could be rewritten by using the rotation matrix R from Eq. 2.2.4 so that [Göl10]:

$$\widetilde{\varepsilon_r} = R\overleftrightarrow{\varepsilon_r}R^{-1}. \tag{2.3.1}$$

It is obvious from Eq. 2.3.1 that the relative permittivity experienced by the microwave field depends on the angle between the director and the microwave field. By changing the orientation of the director, this angle will also change, resulting in a change in relative permittivity. Thus the electrical property of an LC-based device will be changing as well and a tunable microwave device is obtained.

Therefore, aligning the director into certain orientations is an important thing to consider when designing tunable LC devices. The common methods for aligning the LC director are using a mix of alignment layer and external fields, or using fully external electro- or magnetostatic fields. Before discussing further about the alignment methods, the elastic continuum theory of LC will be pointed out first, which explains the alignment of the LC directors.

Continuum Theory and Free Energy Formulation of LC

In this theory, LC is treated as a continuum, which means the material fills the entire possible space and is continuously distributed. Thus, a local director can be defined at every small volume or point. At the equilibrium state, the energy of the system, which is described by the Gibbs free energy, should be minimized at constant temperature and pressure according to the second law of thermodynamics. However, the energy will increase if there is a change in the director's orientation. Therefore, the directors will align to the new direction, which gives the minimum energy [YW06], [Kar14].

Athough aligned in a certain direction, spatial variation or deformation of directors may appear due to external forces. The basic deformations are splay, twist and bend, which are shown in Fig. 2.3.

These deformations energy which their contribution can be written as:

$$\begin{aligned} f_{\text{elastic}} &= f_{\text{splay}} + f_{\text{twist}} + f_{\text{bend}} \\ &= \frac{1}{2}K_{11}\left(\nabla \cdot \vec{n}\right)^2 + \frac{1}{2}K_{22}\left[\vec{n} \cdot \left(\bigtriangledown \times \vec{n}\right)\right]^2 + \frac{1}{2}K_{33}\left[\vec{n} \times \left(\bigtriangledown \times \vec{n}\right)\right]^2 . \end{aligned} \tag{2.3.2}$$

Eq. 2.3.2 is a fundamental equation of the continuum theory for nematic LCs, where K_{11}, K_{22} and K_{33} are called the Oseen-Frank elastic constants for splay, twist and bend deformations [dJ79], [YW06].

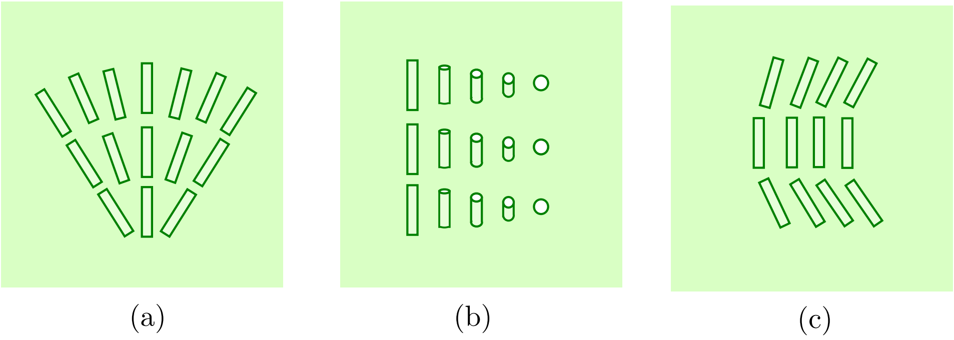
(a) (b) (c)

Figure 2.3.: Possible deformations of the LC directors: (a) splay, (b) twist and (c) bend. Each of them has an elastic constant of K_{11}, K_{22} and K_{33}, respectively.

Besides these LC deformations, another factor contributing to the free energy of LC is the anchoring energy due to the contact with the LC container. According to the Rapini-Papoular model, the free energy can be formulated as [YW06]:

$$f_{\text{surface}} = \frac{1}{2} W_p \sin^2\left(\theta - \theta_0\right) + \frac{1}{2} W_a \sin^2\left(\phi - \phi_0\right), \tag{2.3.3}$$

where W_p and W_a are the polar and azimuthal anchoring strength, respectively. θ_0 and ϕ_0 represent the preferred orientation. Generally, the polar anchoring strength is one or two order of magnitude larger than the azimuthal anchoring strength [WFJD07].

In this work, the external electric and magnetic alignment fields give the highest contribution to the free energy. With presence of an electric field, the change of the free energy per unit of volume can be written as: [Kar14]:

$$f_{\text{electric}} = -\frac{1}{2}\varepsilon_0 \left(\left\langle \vec{E}^2 \right\rangle \varepsilon_{r,\perp} + \Delta\varepsilon_r \left\langle \left(\vec{n} \cdot \vec{E} \right)^2 \right\rangle \right). \tag{2.3.4}$$

Similarly, the contribution of the external magnetic field can be expressed as:

$$f_{\text{magnetic}} = -\frac{1}{2}\mu_0 \left(\left\langle \vec{H}^2 \right\rangle \mu_{r,\perp} + \Delta\mu_r \left\langle \left(\vec{n} \cdot \vec{H} \right)^2 \right\rangle \right). \tag{2.3.5}$$

Now, with all of these contributing factors, the Gibbs free energy of the system can be calculated as [YW06]:

$$W_f = \int_{\text{Volume}} \left(f_{\text{elastic}} + f_{\text{surface}} + f_{\text{electric}} + f_{\text{magnetic}} \right) dV. \tag{2.3.6}$$

Biasing with Alignment Layers

The principle of this method is based on Eq. 2.3.3. The system has a minimum free energy if $\theta = \theta_0$ and $\phi = \phi_0$. Therefore, the director will follow the orientation angles

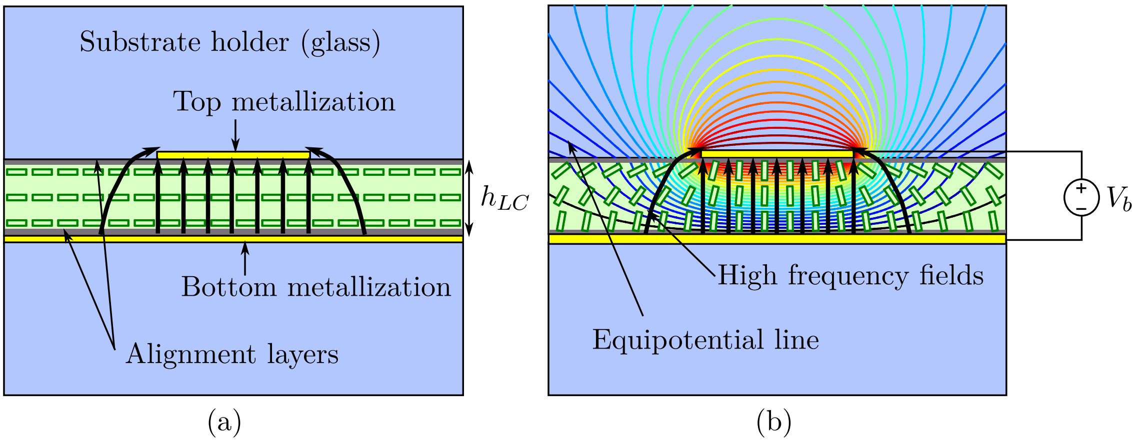

Figure 2.4.: LC-biasing with alignment layers: (a) unbiased state, the directors are anchored parallel to the surface or perpendicular to the high frequency fields, (b) biased state, the directors are parallel to the external fields (which is also in the same direction as the high frequency fields).

of θ_0 and ϕ_0. Anisotropic alignment layers can be fabricated in order to anchor the LC directors parallel to the surface ($\theta_0 = 90°$), which equals a perpendicular orientation to the high frequency electric field. As shown in Fig. 2.4, alignment layers can be created on the surface of the metallizations usually by using Nylon 6 or polyimide. These materials are spin-coated on the surface of metallization, cured and finally rubbed in a certain direction by a rubbing machine. The details of these processes can be seen in [Göl10], [Kar14]. To tune the LC directors to parallel orientation, a biasing voltage is applied, so that external electric field appears. This external field will change the orientation of the directors according to the Eq. 2.3.4, so that the directors are moving continuously towards the parallel state. The value of the voltage V_b will determine the orientation of the directors, and therefore, the effective permittivity.

However, this alignment method has a drawback on the response time, especially for the state change from parallel to perpendicular (switch off), which is done without external biasing fields. The response time is proportional to the square of the thickness of the LC layer (h_{LC}) [Göl10], [Kar14], resulting in a slow response device for comparatively thick LC layers. The height of the LC layer can be reduced, typically below 100 µm [Göl10], in order to make a fast response device, but on the other hand, the metallic loss is increased which is undesirable.

Fully Electro- or Magnetostatic Alignment of Liquid Crystal

The fully electro- or magnetostatic alignment method is used to align the directors in this work. This means the alignment layer is no longer needed. The concept of this

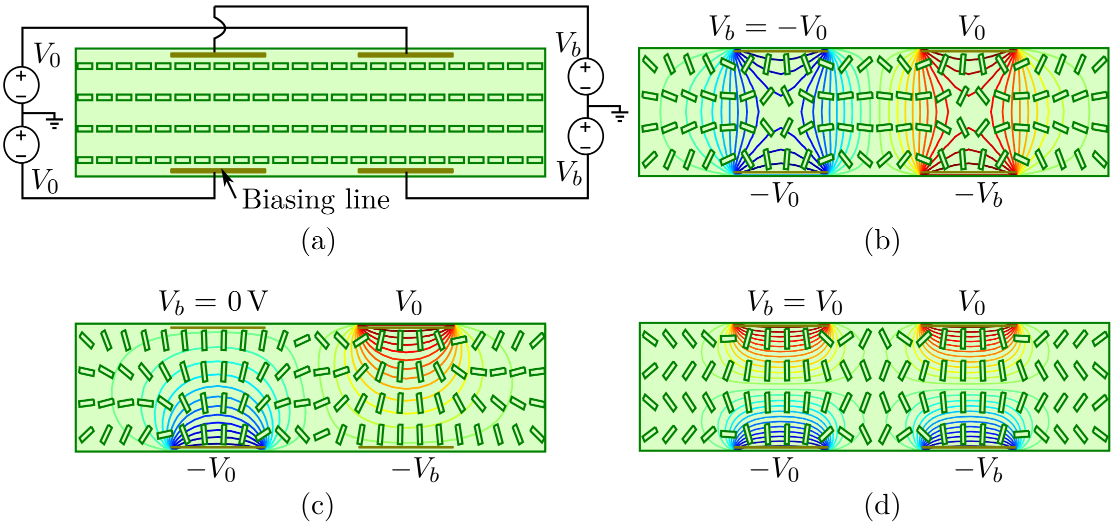

Figure 2.5.: An example of an LC-based device biased only by electric biasing fields produced by fixed voltages V_0 and tunable voltages V_b. (a) Basic biasing structure with four biasing lines or electrodes. (b) Perpendicular state ($V_b = -V_0$). (c) Intermediate state (for example when $V_b = 0\,\mathrm{V}$). (d) Parallel state ($V_b = V_0$).

alignment method is based on Eq. 2.3.4 or Eq. 2.3.5, where the LC directors follow the direction of $\vec{E}$ or $\vec{H}$-field to minimize the Gibbs free energy of the system.

In order to generate the external biasing field, several biasing lines are fabricated inside a tunable microwave device [GGM$^+$09]. The working principle is shown in Fig. 2.5. Consider four biasing lines inside the structure where the bottom-left and top-right lines are assigned with a fixed voltage of $-V_0$ and $+V_0$, respectively. Tunable voltages of $\pm V_b$ are applied on the other two biasing lines according to Fig. 2.5. When $V_b = -V_0$, the LC directors are in the perpendicular state. Increasing the voltage, for instance to 0 V, will change the LC into an intermediate state where the relative permittivity of LC is higher than in the previous case. Finally, the parallel state is achieved when $V_b = +V_0$. This biasing method is useful for a device with thick layer of LC, as the electric force is stronger than the anchoring force employed in the alignment layer method. It is also important when the fabrication process is not compatible with the fabrication process of alignment layers, for example in low temperature co-fired ceramic (LTCC) technology (will be discussed in Chapter 4).

Another possibility is a biasing using $\vec{H}$-field, requiring two permanent magnets outside the tunable microwave device. These magnets can be moved in accordance with the desired state of the LC, as shown in Fig. 2.6. Although this method is bulky and unpractical for real applications, it is possible to employ it for a lab-scale prototyping, since the fabrication of the biasing line as in the electric field method is not required.

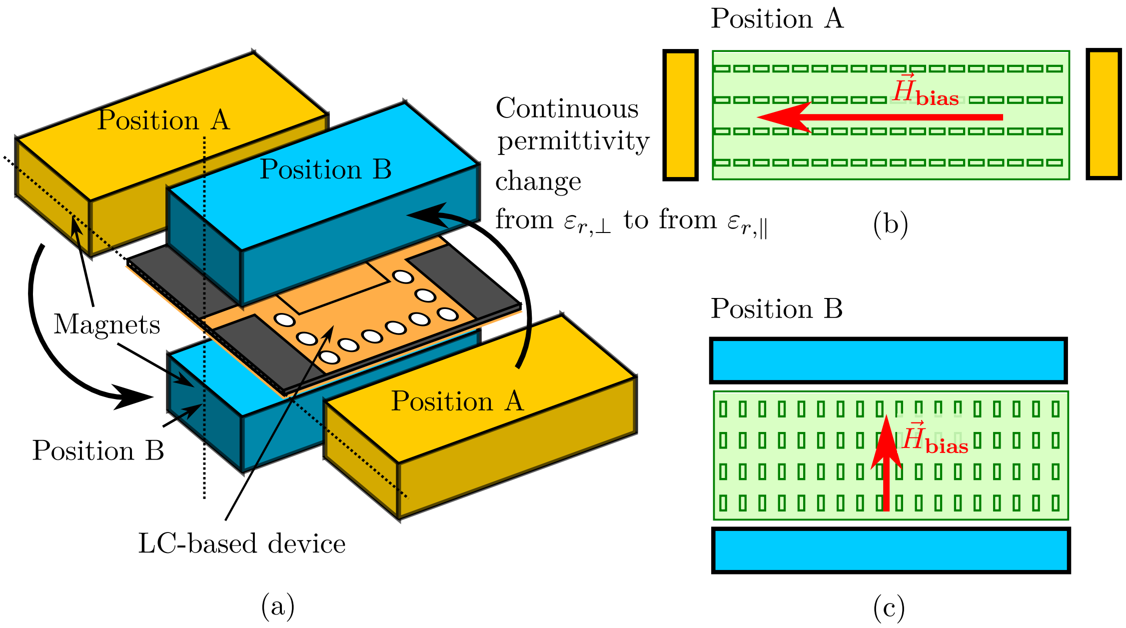

(a)

(b)

(c)

Figure 2.6.: (a) Fully magnetic alignment of a tunable microwave device based on LC using two permanent magnets. (b) Position A for the perpendicular state ($\varepsilon_r = \varepsilon_{r,\perp}$) and (c) position B for the parallel state ($\varepsilon_r = \varepsilon_{r,\|}$).

2.4 LIQUID CRYSTAL BASED MICROWAVE TRANSMISSION LINE TOPOLOGIES

In this section, several examples of LC-based microwave transmission line topologies are given. These are important to construct LC-based tunable microwave devices.

In general, the existing microwave topologies can be classified into planar and waveguide structures. Planar topologies are 2-dimensional circuits, which can be fabricated by using printed transmission line technologies [OM72, Kar14]. Several examples of planar topologies are shown in Fig. 2.7, which includes microstrip line (MSL) [Hon11], stripline [JSH$^+$15] and coplanar waveguide (CPW) [Wen69]. Most of the structures require metallization and dielectric substrate. For the fabrication, technologies such as printed circuit board (PCB) [Lee04] and low temperature co-fired ceramic (LTCC) [Wol09] can be used. In addition to their capability to print the transmission lines, some structures such as metallic vias and empty cavities are also supported. Thus, extended planar topology with vias such as grounded coplanar waveguide (GCPW) (see Fig. 2.7d) is also possible to be fabricated. Cavities are also important for realizing the LC-based tunable microwave device, which will be demonstrated in Chapter 3 and 4 in PCB and LTCC technology, respectively.

On the other hand, waveguide topologies are 3-dimensional structures, using only a single conductor or metallization (see Fig. 2.7e). Therefore, they cannot support transverse electromagnetic (TEM) mode like the previous topology examples. However,

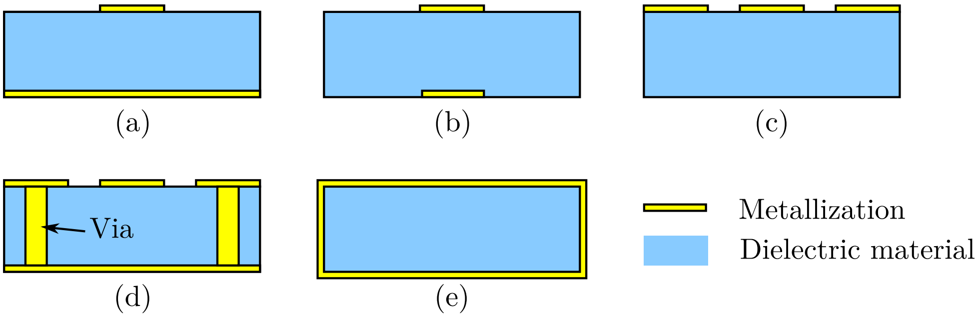

Figure 2.7.: Commonly used topology for microwave devices: (a) microstrip line (MSL), (b) stripline, (c) coplanar waveguide (CPW), (d) grounded coplanar waveguide (GCPW) and (e) waveguide (rectangular and filled with dielectric).

transverse electric (TE) and transverse magnetic (TM) modes are supported so that the waves can propagate only above a certain cutoff frequency f_c [Poz11]. Compared to the planar topologies, typical waveguide structures offer low losses and better power handling capability. Nevertheless, planar structures have some advantages over the waveguide counterpart, especially on the production cost and compactness [CW14]. The planar and waveguide structures can be combined to achieve the advantages from both. This combined structure is called substrate integrated waveguide (SIW), which will be discussed in Chapter 3.

When the dielectric material inside the planar or waveguide structure is replaced by LC, tunable microwave structures are obtained. For the planar structure, MSL topology (Fig. 2.7a) is commonly used [KFN02, Kar14], which can be fabricated by the similar glass technology used in display applications. Stripline topology (Fig. 2.7b), of which the metallic stripes have the same width, is another alternative for tunable planar topology, which has a better efficiency compared to the MSL [JSH$^+$15]. The stripline topology will be applied to construct the amplitude tuner in Chapter 4. CPW structures (Fig. 2.7c and Fig. 2.7d) with LC have also been reported [GGG$^+$09, FGK$^+$12]. Although the topology is not used for the tunable structures in this work, several devices employ the CPW structures to connect the main structure with the measurement probes. For tuning waveguide structures (Fig. 2.7e), commonly, an LC-filled line section is inserted in the center of it [GGM$^+$09, WNG$^+$13b]. Fully electrostatic biasing is preferred for this topology, because the thickness is usually larger than 100 µm.

There are several applications of these LC-filled topologies, for example phase shifter. Tunable delay line concept can be utilized, which means, the change of the LC's permittivity will also alter the electrical length of the transmission line. Hence, the phase of the output signal varies according to the permittivity of LC. The phase shift (ϕ) equation for a transmission line with phase constant β, which depends on the permittivity of the dielectric materials inside the transmission line and its topology, is [Mis01]:

$$\phi = \beta l, \tag{2.4.1}$$

where l is the physical length of the transmission line. Two extreme values of β, regarding with the tunable LC as a material inside the transmission line, are $\beta_\perp$ and $\beta_\parallel$. With the corresponding phase shift $\phi_\perp$ and $\phi_\parallel$, the maximum differential phase shift of the phase shifter could be defined as:

$$\Delta\phi_{\mathrm{max}} = \phi_\perp - \phi_\parallel = \left(\beta_\perp - \beta_\parallel\right) l = \Delta\beta l \tag{2.4.2}$$

Due to the anisotropic properties of the LC's loss tangent (Section 2.2), the figure of merit (FoM) of a tunable phase shifter can be defined as [MSW$^+$04]:

$$\mathrm{FoM} = \frac{\Delta\phi_{\mathrm{max}}}{\mathrm{IL}_{\mathrm{max}}}. \tag{2.4.3}$$

where $\mathrm{IL}_{\mathrm{max}}$ is the maximum insertion loss.

Typical planar structures have FoM ranging from 10–110 °/dB, depending on the quality of the LC and other materials, as well as the operating frequency [BMSY$^+$10, MFBJ10, FKR$^+$13, Kar14]. Higher FoM can be achieved with waveguide structure. For example, FoM up to 200 °/dB is reported in [GGM$^+$09]. Furthermore, these transmission line structures can be terminated with open or short circuit. Hence, a tunable microwave resonator is obtained, which has an important role in microwave devices such as filter. The properties of resonator will be discussed in Chapter 3.

3

TUNABLE LIQUID CRYSTAL BASED SUBSTRATE INTEGRATED WAVEGUIDE (SIW) FILTER IN PRINTED CIRCUIT BOARD (PCB) TECHNOLOGY

In this chapter, tunable LC bandpass filters will be discussed. The filters use the substrate integrated waveguide (SIW) topologies due to their low loss property compared to planar structures, as explained in Chapter 1. Therefore, the fundamentals of the SIW structure will be explained first in Section 3.1. To verify the combination of LC and SIW, LC-based resonators, which are the building block of the tunable filters, is proposed in Section 3.2, as well as 3-pole bandpass filters in Section 3.3. The magnetic alignment method (Section 2.3) is used for these devices, which is the simplest way to verify the concept. Some efforts have also been made to achieve electrically tunable SIW devices, as will be discussed in Section 3.4. All of the devices in this chapter is fabricated by using printed circuit board (PCB) technology, which is commonly used in microwave engineering.

3.1 FUNDAMENTALS OF SIW STRUCTURES

Before discussing the filter, the concept of SIW will be introduced first. A typical SIW structure is shown in Fig. 3.1. The SIW structure consists of several metallic vias on the left and the right side connecting the top metal and ground plane. The vias has a diameter of d_{via} with the pitch between adjacent vias (center to center) of p_{via}. A dielectric substrate with a relative permittivity of ε_r is used between top and ground plane. Talking about the field configuration, SIW cannot support transverse electromagnetic mode (TEM) as the top metal and ground plane are connected with metallic vias. Therefore, the fundamental mode in SIW structure is transverse electric (TE_{10}) mode, which is similar to the waveguide structure. Transverse magnetic (TM) mode is also not supported in SIW structure because the TM wave will leak out from the spacing between vias.

In order to fabricate an SIW structure which support TE_{10} mode, the following criteria should be fulfilled [CW14]:

$$d_{\text{via}} < p_{\text{via}} \leq 2d_{\text{via}} \tag{3.1.1}$$

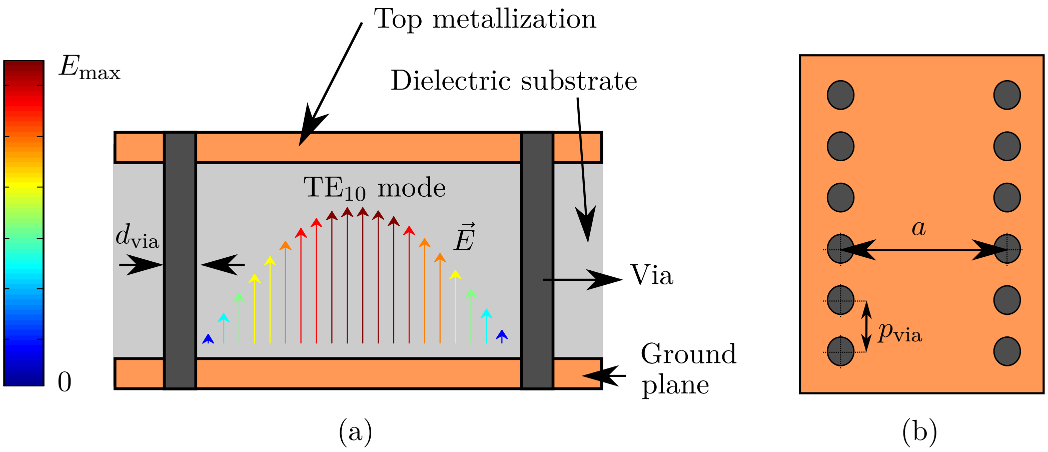

Figure 3.1.: SIW transmission line with TE$_{10}$ mode: (a) cross section, (b) top view.

$$0.05 < \frac{p_{\text{via}}}{\lambda} < 0.25. \tag{3.1.2}$$

The upper bound in Eq. 3.1.1 is related with the radiation losses. The ratio between radiation losses (α_r) and the wavenumber k_0 for the dielectric material should not exceed 10^{-4}. This is always fulfilled for $p_{\text{via}} \leq 2d_{\text{via}}$. The lower bound indicates the requirement to be met in order to realize the SIW since the pitch cannot be smaller than the diameter of the via. The Eq. 3.1.2 is formulated to avoid the bandstop effect in the operating frequencies and to minimize the number of fabricated vias, respectively for the upper and lower bound.

TE$_{10}$ mode SIW structure is equivalent to rectangular waveguide in the same mode. The dimension of the SIW structure can be mapped into the equivalent dimension of a rectangular waveguide. For example, an SIW width of a is the same as a rectangular waveguide with the effective width of a_{eff}, which is related by following mapping equation [XW05]:

$$a_{\text{eff}} = a - 1.08\frac{{d_{\text{via}}}^2}{p_{\text{via}}} + 0.1\frac{{d_{\text{via}}}^2}{a}, \tag{3.1.3}$$

with $p_{\text{via}}/d_{\text{via}} < 3$ and $d_{\text{via}}/a < 1/5$. Eq. 3.1.3 is plotted in Fig. 3.2 for several values of d_{via} and p_{via}. It is indicated from Fig. 3.2 that the effective width a_{eff} is always less than the actual width a.

Eq. 3.1.3 enables the usage of commonly used waveguide equations in SIW structure. For example, the cutoff frequency of TE$_{10}$ mode of SIW transmission line can be expressed as:

$$f_c = \frac{c}{2a_{\text{eff}}\sqrt{\varepsilon_r}} \tag{3.1.4}$$

where c is the speed of electromagnetic wave in vacuum.

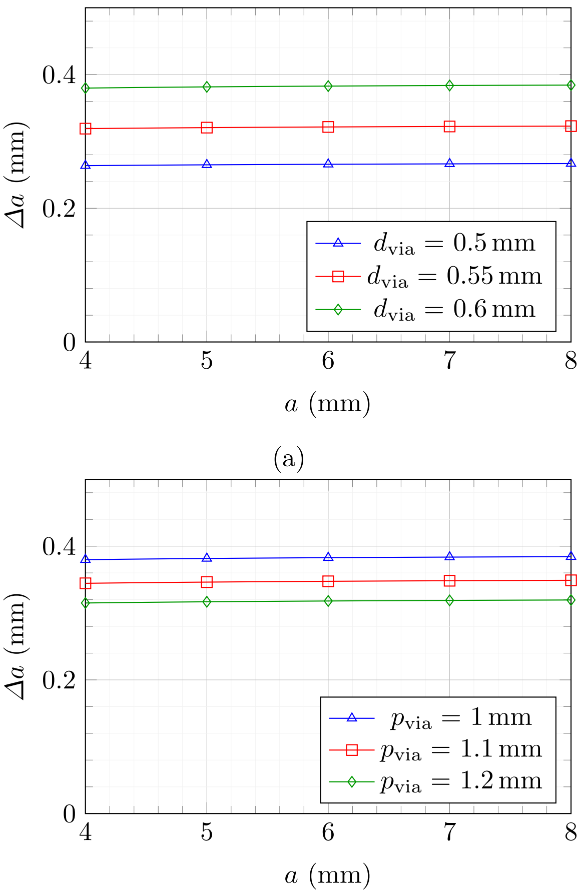

(a)

(b)

Figure 3.2.: Plot of Eq. 3.1.3 with (a) several values of d_{via}, with $p_{\text{via}} = 1\,\text{mm}$; and (b) several values of p_{via}, with $d_{\text{via}} = 0.6\,\text{mm}$. The value of Δa, which is $a - a_{\text{eff}}$, is always positive, indicating the effective width a_{eff} always smaller than the actual width a.

3.2 MAGNETICALLY TUNABLE LC-FILLED SIW RESONATOR

LC-filled SIW resonator will be investigated in this section. The theoretical aspects of the resonator will be given first in Subsection 3.2.1. Using this knowledge, a tunable resonator will be designed and analyzed in Subsection 3.2.2. The fabrication and measurement results are presented in Subsection 3.2.3.

3.2.1 *Fundamentals of Resonator*

A resonator can be constructed from a terminated transmission line at both ends, for example by short circuit, which is robust to radiation losses. When using a short circuited SIW transmission line as a resonator, the fundamental resonant mode is TE_{101}, which has a resonant frequency of:

$$f_{0,101} = \frac{c}{2\sqrt{\varepsilon_r}}\sqrt{\left(\frac{1}{a_{\text{eff}}}\right)^2 + \left(\frac{1}{l_{\text{res,eff}}}\right)^2}, \tag{3.2.1}$$

with $l_{\text{res,eff}}$ is the effective length of the resonator. Since the frequency is known from the design specification, the effective dimensions can be determined and then mapped back to SIW dimensions as described in Eq. 3.1.3.

As can be seen in Eq. 3.2.1, a change in the relative permittivity ε_r leads into a resonant frequency shift. By totally replacing the dielectric material in the SIW with LC, the resonant frequency of the resonator is controllable through LC biasing. Since the resonant frequency is inversely proportional to the square root of the relative permittivity of the material, the perpendicular state of LC gives the highest resonant frequency. Tuning towards the parallel state decreases the resonant frequency as the relative permittivity of LC is increasing. In this case, the maximum and minimum resonant frequency is determined by the relative permittivity of the LC.

However, filling the whole resonator with LC is not an effective approach to construct a tunable resonator since the LC has usually a higher losses compared to the standard non-tunable substrate. In addition, the fabrication process is more difficult for a full LC tunable SIW structure, especially for the via part. Therefore, a resonator partially filled with LC is more feasible to fabricate.

For a SIW transmission line with TE_{10} mode or a resonator with TE_{101} mode, the high frequency electric fields are concentrated in the center, as shown in Fig. 3.1. Thus, placing LC in the center surrounded by a low-loss dielectric substrate is an effective way to create a tunable device.

For a tunable resonator, there are several parameters which indicate its performance: tunability and quality factor (Q-factor).

Tunability

In this work, tunability is defined as:

$$\tau_{\text{res}} = \frac{f_{\text{max}} - f_{\text{min}}}{f_{\text{max}}} \cdot 100\%, \tag{3.2.2}$$

where f_{min} and f_{max} are the possible lowest and highest frequency and their difference, $f_{\text{max}} - f_{\text{min}}$, is called the tuning range of the resonator or filter.

The tunability of the proposed resonator is determined by the amount of LC inside it. The maximum tunability of the resonator is achieved when the LC replaces the non-tunable dielectric material completely. Thus, the tunability depends only on the relative permittivity value of LC at the extreme states. By using Eq. 3.2.1 to calculate the resonant frequency of the TE_{101}-mode resonator and substituting it into Eq. 3.2.2, it can be shown that the maximum tunability is:

$$\tau_{\text{res,max}} = \frac{\sqrt{\varepsilon_{r,\parallel}} - \sqrt{\varepsilon_{r,\perp}}}{\sqrt{\varepsilon_{r,\parallel}}} \cdot 100\%. \tag{3.2.3}$$

For instance, a TE_{101} resonator fully filled with LC GT5-series from Merck with relative permittivity of 2.39–3.27 gives a maximum tunability of 14.5 % under the perfect LC alignment conditions. The maximum tuning range itself can be varied depends on the operating frequency. The higher the operating frequency, the larger the tuning range. In the partially LC-filled resonator, the tunability reduction is expected due to the presence of the non-tunable materials.

Q-factors

In terms of power losses, Q-factor is commonly used to describe the resonator performance. Q-factor can be defined at a resonant frequency of f_0 (or $\omega_0 = 2\pi f_0$) as [Poz11, MYJ80]:

$$Q = \omega_0 \frac{\text{Average energy stored}}{\text{Energy loss per second}}. \tag{3.2.4}$$

There are several types of Q-factors: unloaded, external and loaded Q-factor [MYJ80]. The unloaded Q-factor is defined as the Q-factor when there is no external circuit. Since a resonator can be represented by the equivalent circuit in Fig. 3.3 (see the gray box) [Poz11], the unloaded Q-factor Q_u can be calculated as:

$$Q_u = \frac{\omega_0 L}{R} = \frac{1}{\omega_0 RC}. \tag{3.2.5}$$

To excite the resonant modes, the resonator should be connected with the signal source. External Q-factor describes the effect of this external circuit to the resonator. When

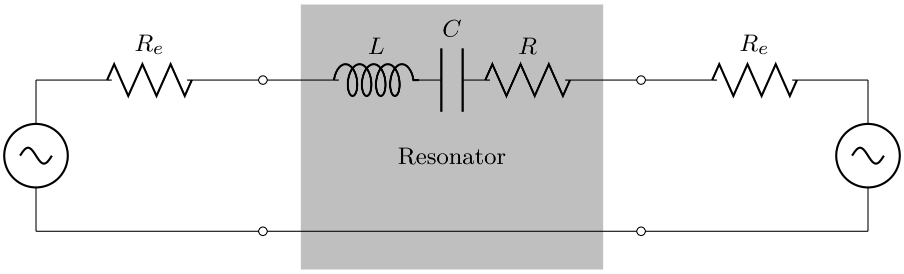

Figure 3.3.: An RLC circuit model of the resonator with double external loading (R_e).

the resonator sees an external impedance of R_e at its port, the external Q-factor Q_e for that port can be defined as:

$$Q_e = \frac{\omega_0 L}{R_e}. \tag{3.2.6}$$

The value of Q_e and R_e are determined by the coupling between the resonator and the external circuit. This is useful for designing a filter, which will be explained in Subsection 3.3.1.

Finally, the loaded Q-factor Q_L combines both the unloaded and external Q-factor. For a resonator with a load at each port in Fig. 3.3, the loaded Q-factor can be defined as the ratio between the reactance of the resonator $\omega_0 L$ and the total of the resistive loads in the circuit:

$$Q_L = \frac{\omega_0 L}{R + R_e + R_e}. \tag{3.2.7}$$

From the S-parameter measurement, especially the transmission coefficient $|S_{21}|$, the loaded Q-factor can be easily obtained by [Hon11]:

$$Q_L = \frac{f_0}{B_w} = \frac{1}{\mathrm{FBW}}, \tag{3.2.8}$$

where f_0 is the resonant frequency of the resonator, B_w is corresponding the 3 dB bandwidth and FBW is the fractional bandwidth or the ratio between B_w and f_0.

If the loaded Q-factor is already obtained, the unloaded Q-factor can be extracted. By substituting Eq. 3.2.5 into Eq. 3.2.7, the following equations can be obtained:

$$Q_u = \frac{Q_L}{1 - \dfrac{2R_e}{R + 2R_e}}. \tag{3.2.9}$$

Since the S_{21} of the resonator is:

$$S_{21} = \frac{2R_e}{R + j\left(\omega L - \dfrac{1}{\omega C}\right) + 2R_e} \tag{3.2.10}$$

and its impedance is purely resistive at the resonant frequency f_0, Eq. 3.2.9 can be modified into:

$$Q_u = \frac{Q_L}{1 - |S_{21}(f_0)|}. \tag{3.2.11}$$

From Eq. 3.2.8, Eq. 3.2.11 can be rewritten as [Hon11]:

$$Q_u = \frac{\frac{f_0}{B_w}}{1 - |S_{21}(f_0)|}. \tag{3.2.12}$$

Not only related to the insertion loss, the values of unloaded Q-factor also affect the 3-dB bandwidth of the resonator, as indicated in Eq. 3.2.12. Fig. 3.4 shows the response ($|S_{21}|$) of resonators with various value of Q_u. By using the lower Q-factor, the corresponding bandwidth will be larger. This bandwidth change will cause a passband rounding effect if the low Q-factor resonators are employed to construct a microwave filter. This makes the unloaded Q-factor of the resonator important for filter design, since the rounding effect reduce the selectivity of the filter [TL06].

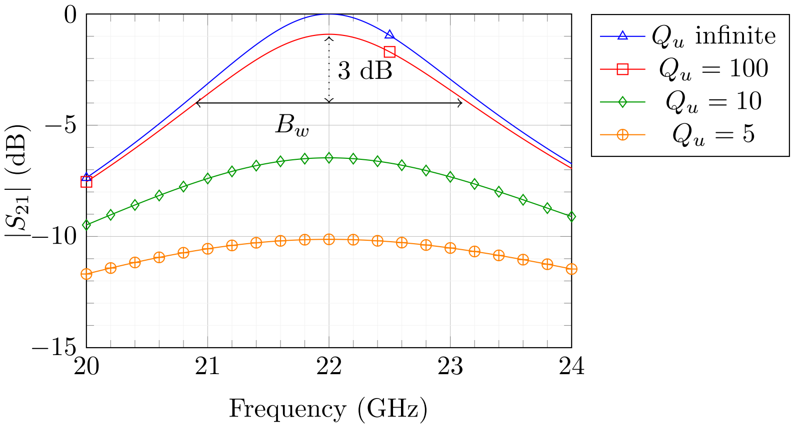

Figure 3.4.: Typical responses ($|S_{21}|$) of resonators with various unloaded Q-factor Q_u. The lower Q_u gives a larger 3-dB bandwidth B_w.

3.2.2 *Design and Analysis*

Since the structure is getting more complex, the analysis is carried out by using 3D full-wave microwave simulator such as CST Microwave Studio. Some simulations have been accomplished for a resonator operating around 20 GHz with various width of LC cavity a_{LC}. The LC used in this simulation is the GT5-series from Merck ($\varepsilon_{r,\perp} = 2.39$, $\varepsilon_{r,\parallel} = 3.27$, $\tan\delta_\perp = 0.007$ and $\tan\delta_\parallel = 0.0022$). As the non-tunable dielectric material, PCB Rogers RT/duroid RT5880 with ε_r of 2.2 and $\tan\delta$ of 0.0009 [Rog16b] is used

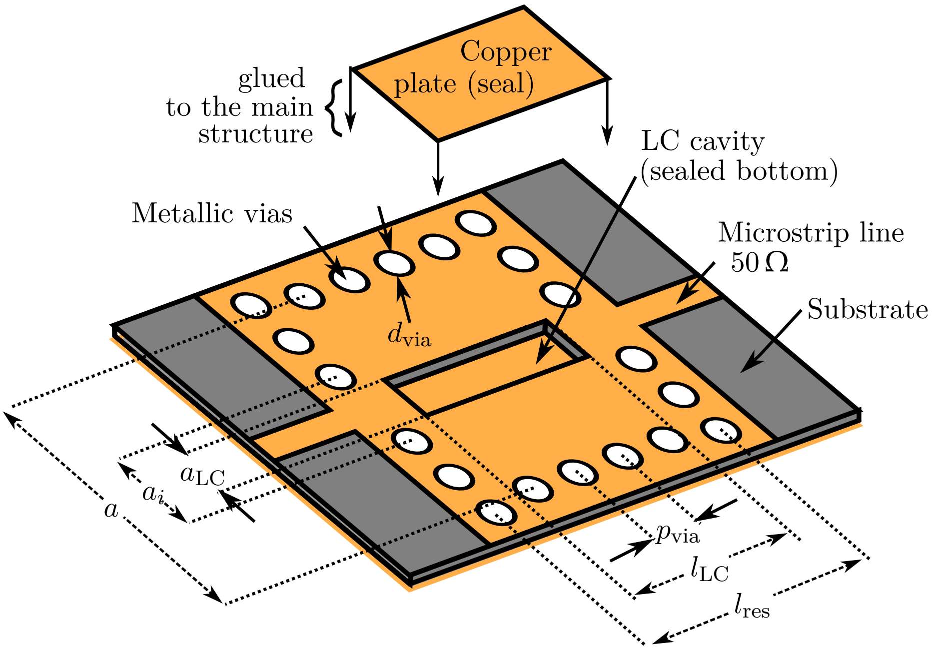

Figure 3.5.: The basic structure of a tunable SIW resonator based on LC.

in this work. A microstrip line with a line impedance of 50 Ω is employed to feed the resonator through an inductive iris with a width of a_i. For the via metallization, metallic paste LPKF ProConduct is used [LPK14]. The detailed structure is shown in Fig. 3.5 with the following dimensions: $a = 6.92\,\text{mm}$, $l_{\text{res}} = 6\,\text{mm}$, $a_i = 1.8\,\text{mm}$, $l_{\text{LC}} = 4\,\text{mm}$, $d_{\text{via}} = 0.6\,\text{mm}$ and $p_{\text{via}} = 1.2\,\text{mm}$.

With the simulation results shown in Fig 3.6a, it can be seen that the larger a_{LC} gives a better tunability which is closer to the maximum bound $\tau_{\text{res,max}}$ (the dotted line in Fig 3.6a). This is happened because most of the microwave fields are inside the LC with a bigger LC cavity. However, lower Q-factor is expected for a bigger LC cavity because of the LC dielectric losses.

Eq. 3.2.12 can be employed to analyze the Q-factor of the LC-based SIW resonator from the previous simulation. Fig. 3.6b shows the effect of a_{LC} to the Q-factor. Because of the higher losses of the LC, the Q-factor decreases as the a_{LC} increases. This means a_{LC} has to be as small as possible but still fulfill the tunability requirement. Note that the perpendicular state always has a lower Q-factor compared to the parallel state due to higher loss tangent of the LC at that state.

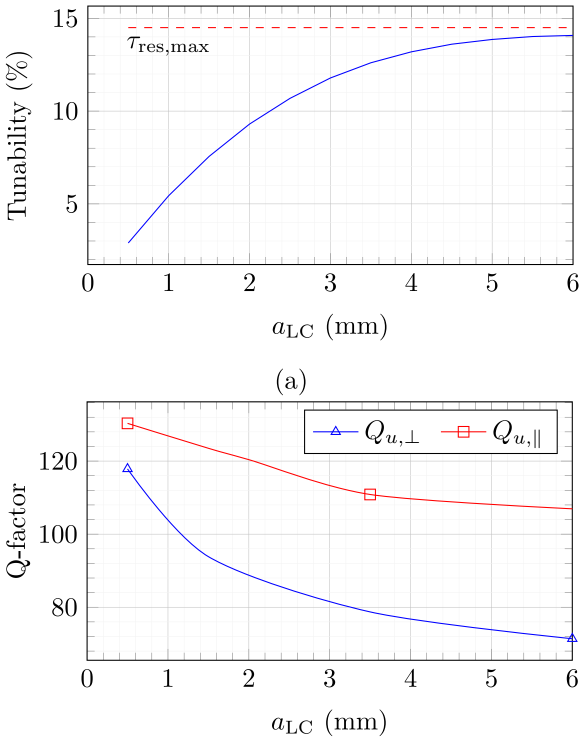

(a)

(b)

Figure 3.6.: The effect of LC cavity width (a_{LC}) to the resonator (a) tunability and (b) unloaded Q-factor.

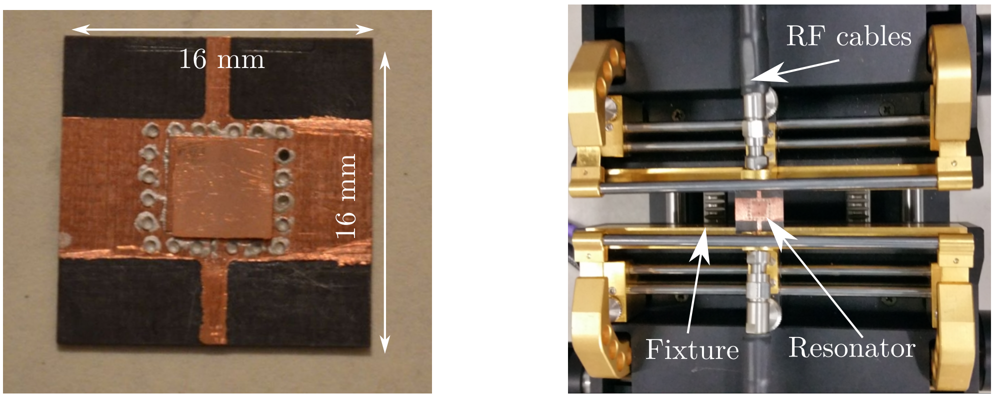

(a) (b)

Figure 3.7.: (a) The fabricated SIW resonator. (b) Measurement setup for SIW resonator.

3.2.3 *Fabrication and Measurement*

For a proof of concept, a single tunable rectangular LC-filled SIW resonator is designed and will be fabricated. For LC directors tuning, magnets are employed, which enable a rapid and simple evaluation.

Fabrication and Measurement Setup

The simulated structure in Fig. 3.5 is utilized. A rectangular hole is opened inside the rectangular SIW resonator by using a milling machine. Via holes are also created in this process and filled with LPKF ProConduct Paste for the metallization. After paste filling, the structure is baked with a temperature of 90 °C in order to harden the paste. Copper plates are glued with two components metallic glue to the PCB in order to seal the LC cavity. Before being sealed completely, two holes are drilled in the top sealing plate for LC filling purpose. The structure itself has the same dimensions as mentioned in Subsection 3.2.1 and $a_{\mathrm{LC}} = 1\,\mathrm{mm}$ is chosen. The fabricated resonator is shown in Fig. 3.7a along with the measurement setup.

A microstrip fixture is used in the measurement to connect the resonator with the cables and vector network analyzer (VNA). S-parameter measurements are performed and the unloaded Q-factor (Q_u) from each measurement can be obtained by using Eq. 3.2.12.

To change the LC's orientation, two magnets are placed near the structure in the fixture. As already discussed in Subsection 2.3, if the magnets are placed in the left and right side of the structure, the relative permittivity of LC would be $\varepsilon_{r,\perp}$. On the other hand, the relative permittivity would be $\varepsilon_{r,\parallel}$, when the magnets are placed on the top and bottom of the structure.

Measurement of the Unfilled Resonator

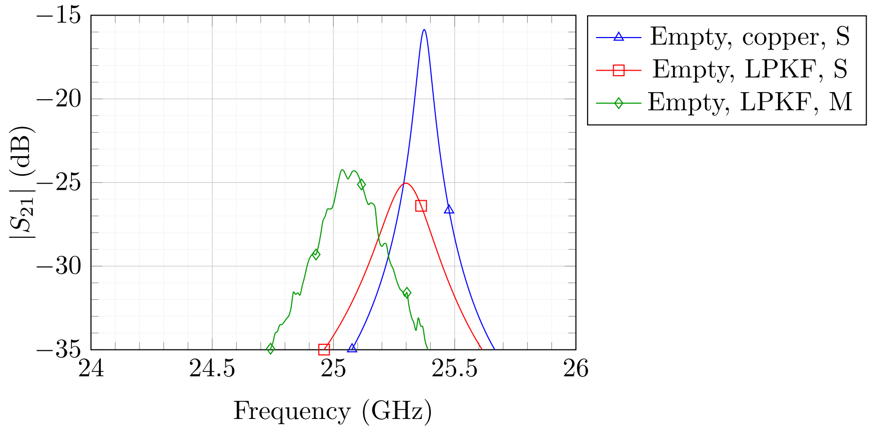

Figure 3.8.: Simulation and measurement results for empty or unfilled resonators. Note: M = measurement; S = simulation.

Before conducting the experiment with the tunable resonator, a measurement with empty or air filled cavity inside the resonator is performed first to verify the structure. The S-parameter simulation and measurement results are shown in Fig. 3.8. For the simulation, the effect of via metallization is investigated by using copper (with conductivity of 5.96×10^7 S/m) and LPKF ProConduct Paste (conductivity around 6×10^4 S/m*). According to the CST simulation, the Q_u of the empty air filled resonator could reach 478 when copper is used for metallization of the vias. By using LPKF ProConduct Paste for the vias, the unloaded Q-factors are reduced to 128.3 in the simulation due to the increasing metallic losses. The fabricated resonator gives an unloaded Q-factor of 118.1 with a small frequency shift (around 200 MHz) due to the fabrication process tolerance. The unloaded Q-factor of the realized tunable resonator cannot surpass these values since LC has a higher dielectric losses.

Measurement of the Tunable Resonator

After injecting the LC into the resonator, the measurement for magnetically tunable resonator is performed. The results are depicted in Fig. 3.9 together with the CST simulation results. The center frequency of the measured resonator varies continuously from 23.88 GHz in perpendicular state ($Q_{u,\perp} = 102$) down to 23.47 GHz in parallel state ($Q_{u,\parallel} = 105.6$), i.e. having a tuning range of 412 MHz. This tuning range is much smaller than the one by simulation with CST, which is 1260 MHz. A possible explanation is the presence of the trapped air gap inside the LC cavity. According to the CST simulation,

---

* Estimated from the resistivity information at [LPK14].

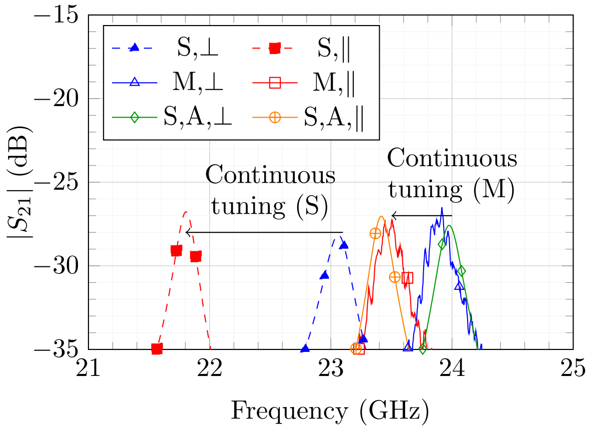

Figure 3.9.: Simulation and measurement results for LC-filled resonators. Note: M = measurement; S = simulation; ⊥ = perpendicular; || = parallel; A = simulation with 0.1 mm air gap.

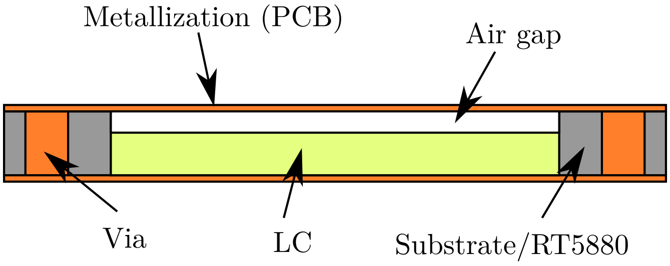

Figure 3.10.: A cross sectional view of a LC-filled SIW resonator with the presence of air gap.

an air gap of 0.1 mm thickness between LC and the top metal provides a good agreement with the measurement results. The simulated air gap model is shown in Fig. 3.10.

The summary of the work on this LC-filled SIW resonator is recapitulated in Table 1.

3.3 MAGNETICALLY TUNABLE SIW BANDPASS FILTER

Having been succesfully demonstrated in Section 3.2, the tunable SIW resonator can be employed to make a higher order bandpass filter. Employing a higher order filter increases the selectivity of the filter or makes the passband-stopband transition steeper. To create one, several resonators can be coupled with certain coupling structures and coefficients. These values, along with the number and dimensions of the resonators, will determine the characteristics of the filter, such as center frequency and bandwidth. This theoretical aspects of the filter will be introduced first in Subsection 3.3.1 and will be employed to design a bandpass filter in Subsection 3.3.2. Finally, an LC-filled SIW filter

Table 1.: Simulation (S) and measurement (M) results of SIW resonator.

Cavity filling	Vias	Q_u	S/M	Tuning range (MHz)
Air	Copper	478	S	-
Air	LPKF	128.3	S	-
Air	LPKF	118.1	M	-
LC	LPKF	124.8	S, $\parallel$	1260
		97	S, $\perp$	
LC	LPKF	105.6	M, $\parallel$	412
		102	M, $\perp$	
LC, 0.1 mm air gap	LPKF	128 118	S, $\parallel$ S, $\perp$	560

will be demonstrated in Subsection 3.3.3. Same as the resonator in Section 3.2, magnetic alignment will be utilized to tune the filter.

3.3.1 *Basic Microwave Bandpass Filter Theory*

As a microwave device, a filter can be described by its S-parameters, namely S_{11} or S_{21}. A filtering function can be created by designing the S-parameters, usually as a ratio between polynomials, for example $F(s)$, $P(s)$ and $E(s)$, defined as the followings [Cam99]:

$$S_{11}(s) = \frac{F(s)}{E(s)} \tag{3.3.1}$$

and

$$S_{21}(s) = \frac{P(s)}{\epsilon_n E(s)}. \tag{3.3.2}$$

s is a complex frequency variable ($s = \sigma + j\omega$) and ϵ_n is a normalization constant. For a realizable filter, the pole of the S-parameters should be in the left-hand side (LHS) of the s-plane.

For a passive filter, this relation holds true:

$$|S_{11}|^2 + |S_{21}|^2 \leq 1. \tag{3.3.3}$$

Return loss RL and insertion losses IL (both in dB) can be defined by the S-parameters as followings [Poz11]:

$$\mathrm{RL} = -20\log_{10}\left(|S_{11}|\right) \tag{3.3.4}$$

and

$$\mathrm{IL} = -20\log_{10}\left(|S_{21}|\right). \tag{3.3.5}$$

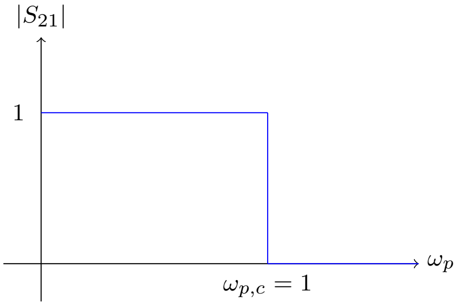

Figure 3.11.: The ideal response of a lowpass prototype, with a cutoff frequency of $\omega_{p,c} = 1$.

To set the filtering function, several inductors or capacitors can be arranged in a certain configuration with certain values. These lumped elements or circuit models can be transformed into the desired microwave structures, for example planar or waveguide structures.

Filter Synthesis Using Lowpass Prototype

A common way to design a filter is using the lowpass prototype. This prototype can be transformed later into another type of filter, such as bandpass filter by appropriate scaling. An ideal lowpass prototype response as a function of angular frequency ω_p (prototype) is shown in Fig. 3.11. Here, the cutoff frequency $\omega_{p,c}$ is equal to 1. This response can be approximated by a typical ladder circuit consists of inductors and capacitors as shown in Fig. 3.12. The i-th component has an inductance or capacitance value of g_i. The both ports of the circuit are terminated by impedances of g_0 and g_{n+1}.

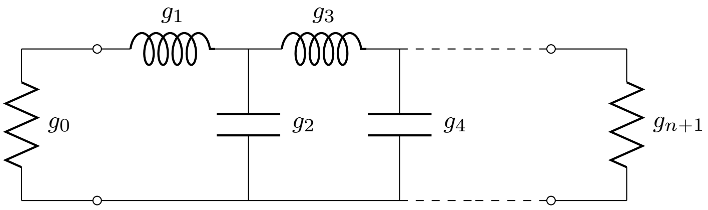

Figure 3.12.: Lowpass prototype with n lumped components. Each component has a value of g_i, where $i = 1, 2, ..., n$. The circuit is terminated by impedances of g_0 and g_{n+1}.

The value of g_i depends on the polynomial used for the S_{11} or S_{21}. One of them is Chebyshev response which provides a trade-off between the filter order, selectivity

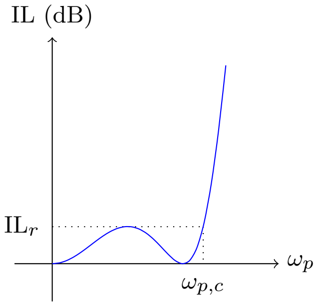

Figure 3.13.: A typical Chebyshev lowpass response.

and passband ripple. In $j\omega_p$-domain, the transfer function S_{21} of a Chebyshev lowpass prototype can be defined as [MYJ80], [Hon11]:

$$\left|S_{21}\left(j\omega_p\right)\right|^2 = \frac{1}{1+\epsilon_C^2 T_n^2\left(\omega_p\right)}, \tag{3.3.6}$$

where $T_n(\omega_p)$ is the Chebyshev function order n of the first kind:

$$T_n\left(\omega_p\right) = \begin{cases} \cos\left(n\cos^{-1}\left(\omega_p\right)\right) & \left|\omega_p\right| \leq 1 \\ \cosh\left(n\cosh^{-1}\left(\omega_p\right)\right) & \left|\omega_p\right| > 1 \end{cases} \tag{3.3.7}$$

and the ripple constant ϵ_C is related to the maximum insertion loss IL$_r$ (in dB) in the passband area:

$$\epsilon_C = \sqrt{10^{\frac{\mathrm{IL}_r}{10}} - 1}. \tag{3.3.8}$$

An example of a filter prototype with a Chebyshev response can be seen in Fig. 3.13.

The corresponding element values g_i is related to the filter order n and passband ripple IL_r [Mis01]:

$$
\begin{aligned}
g_0 &= 1 \\
g_1 &= \frac{2}{\gamma}\sin\left(\frac{\pi}{2n}\right) \\
g_i &= \frac{1}{g_{i-1}}\frac{4\sin\left(\frac{(2i-1)\pi}{2n}\right)\cdot\sin\left(\frac{(2i-3)\pi}{2n}\right)}{\gamma^2+\sin^2\left(\frac{(i-1)\pi}{n}\right)} \qquad i = 2,3,...,n \\
g_{n+1} &= \begin{cases} 1 & n \text{ odd} \\ \coth^2\left(\dfrac{\beta}{4}\right) & n \text{ even} \end{cases} \\
\beta &= \ln\left(\coth\left(\frac{IL_r}{17.37}\right)\right) \\
\gamma &= \sinh\left(\frac{\beta}{2n}\right).
\end{aligned}
\tag{3.3.9}
$$

After finding the prototype element values, the actual values of inductors and capacitors can be calculated by impedance and frequency transformation. The transformation depends on the desirable filter type: lowpass, highpass, bandpass or bandstop. For a bandpass filter, a prototype inductor with values of g can be tranmsformed into series of inductor with an inductance of L_s and a capacitor with a capacitance of C_s forming a microwave resonator. On the other hand, a prototype capacitor can be replaced by a parallel connection between inductor L_p and capacitor C_p. Fig. 3.14 shows a clear overview of the transformation. The relation between those element values can be found by impedance and frequency transformation as followings:

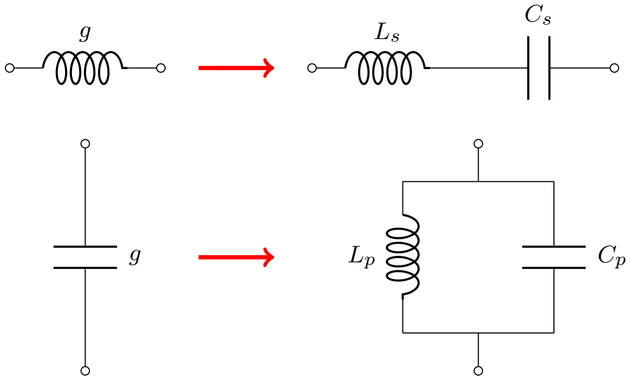

Figure 3.14.: Lowpass prototype to bandpass transformation for each prototype element.

$$\begin{aligned} L_s &= \left(\frac{\omega_{p,c}}{\mathrm{FBW}\cdot\omega_0}\right)\frac{Z_0}{g_0}\cdot g \\ C_s &= \frac{1}{\omega_0^2 L_s} \\ C_p &= \left(\frac{\omega_{p,c}}{\mathrm{FBW}\cdot\omega_0}\right)\frac{g_0}{Z_0}\cdot g \\ L_p &= \frac{1}{\omega_0^2 C_p}, \end{aligned} \tag{3.3.10}$$

where Z_0 is the reference impedance, ω_0 is the center angular frequency of the bandpass filter and FBW is the fractional bandwidth of the filter according to this definition:

$$\mathrm{FBW} = \frac{\omega_2 - \omega_1}{\omega_0} = \frac{\omega_2 - \omega_1}{\sqrt{\omega_1\omega_2}}. \tag{3.3.11}$$

Note that the ω_1 and ω_2 are the lower and upper cutoff frequency of the bandpass filter, respectively.

Coupled-Resonator Filters

The lumped element filter is impractical and has high losses in the microwave region. Therefore, planar and waveguide structures are frequently used for the microwave bandpass filter. The common topology for this purpose is by using several resonators connected to each other, for example coupling structures such as microstrip gaps, waveguide irises or posts. A coupling structure can be modelled by using an impedance inverter. As the name implies, this two port component inverts the impedance at the other port. For instance, if the impedance at port 2 is Z_2, port 1 sees the impedance as:

$$Z_1 = \frac{K^2}{Z_2}, \tag{3.3.12}$$

where K is the characteristic impedance of the inverter. The impedance inverter is symbolized in Fig. 3.15.

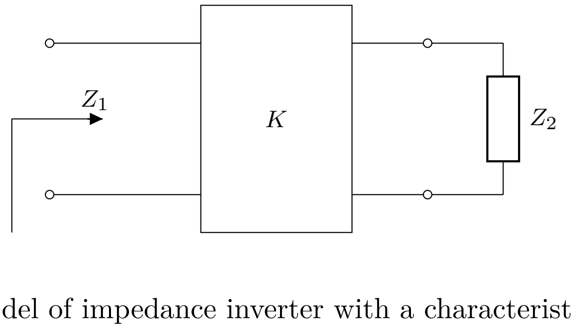

Figure 3.15.: A model of impedance inverter with a characteristic impedance of K.

The lumped element models with element values of g described by Eq. 3.3.9 can be converted to the resonator-inverter model as shown in Fig. 3.16. $X_i(\omega)$ is the reactance of each resonator and $K_{i,i+1}$ is the characteristic impedance of the inverter between resonator or resonator-input/output port. Port 1 and 2 are terminated by resistance of Z_A and Z_B. In most case, both of them are equal to the characteristic impedance of the line (Z_0) used for the feeder. In [MYJ80], it is shown that the element values of the resonator-inverter model are related to the lowpass prototype as followings:

$$\begin{aligned}
x_i &= \frac{\omega_0}{2}\frac{\mathrm{d}X_i(\omega)}{\mathrm{d}\omega}\bigg|_{\omega=\omega_0} \\
K_{01} &= \sqrt{\frac{Z_A x_1 \cdot \mathrm{FBW}}{g_0 g_1 \omega_{p,c}}} \\
K_{i,i+1} &= \frac{\mathrm{FBW}}{\omega_{p,c}}\sqrt{\frac{x_i x_{i+1}}{g_1 g_{i+1}}} \qquad i = 1, 2, ..., n-1 \\
K_{n,n+1} &= \sqrt{\frac{Z_B x_n \cdot \mathrm{FBW}}{g_n g_{n+1} \omega_{p,c}}},
\end{aligned} \tag{3.3.13}$$

where x_i is the reactance slope parameter for i-th resonator and FBW is the fractional bandwidth as defined in Eq. 3.3.11.

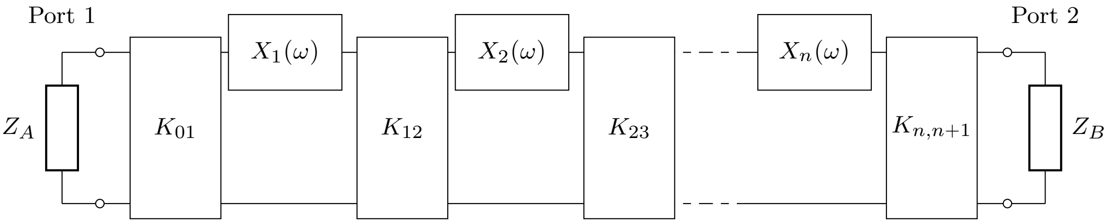

Figure 3.16.: Bandpass filter model using n resonators, which are coupled each other by impedance inverters.

Inverter characteristic K also can be expressed as the external Q-factor Q_e for the first and last resonators and coupling coefficient k [MYJ80] for the other resonators:

$$\begin{aligned}
Q_{e,A} &= \frac{x_1}{K_{01}^2/R_A} = \frac{g_0 g_1 \omega_{p,c}}{\mathrm{FBW}} \\
Q_{e,B} &= \frac{x_n}{K_{n,n+1}^2/R_B} = \frac{g_n g_{n+1} \omega_{p,c}}{\mathrm{FBW}} \\
k_{i,i+1} &= \frac{K_{i,i+1}}{\sqrt{x_i x_{i+1}}} = \frac{\mathrm{FBW}}{\omega_{p,c}\sqrt{g_i g_{i+1}}}.
\end{aligned} \tag{3.3.14}$$

To realize the impedance inverter, there are several possibilities, for example with a section of transmission line Z_0 and an impedance with a reactance of X at the center as shown in Fig. 3.17. For the impedance, an inductor ($X > 0$) or a capacitor ($X < 0$) can be used. The electrical length of the transmission line ϕ will be negative when an inductor is used and vice versa [MYJ80]. However, the negative length can be realized with the help of the neighboring resonator, which has a greater length so that the total length of the resonator is still positive and realizable. The value of the reactance X is related to the inverter value K, as described by:

$$K = Z_0 \tan\left|\frac{\phi}{2}\right| \tag{3.3.15}$$

with

$$\phi = -\tan^{-1}\frac{2X}{Z_0} \tag{3.3.16}$$

and

$$\left|\frac{X}{Z_0}\right| = \frac{K/Z_0}{1-(K/Z_0)^2}. \tag{3.3.17}$$

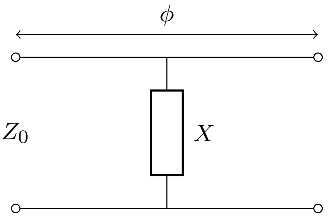

Figure 3.17.: Implementation of K-inverter using a section of transmission line with an impedance. If $X > 0$, then $\phi < 0$ and vice versa.

The shunt inductance model of the impedance inverter can be implemented using waveguide structures, for example as shown in Fig. 3.18. This iris coupling structure with an aperture width a_i can be modelled as a shunt inductor as shown in [Mar51]. The aperture width a_i is related to the reactance X as described in following equation:

$$\begin{aligned} X =& Z_0\frac{a}{\lambda_g}\left[\tan^2\left(\frac{\pi a_i}{2a}\right)\right]\left\{1+\frac{3}{4}\left[\frac{1}{\sqrt{1-\left(\frac{2a}{3\lambda}\right)^2}}-1\right]\sin^2\left(\frac{\pi a_i}{a}\right)+2\left(\frac{a}{\lambda}\right)^2\right. \\ &\left.\left[1-\frac{4}{\pi}\cdot\frac{E(\alpha)-\beta^2F(\alpha)}{\alpha^2}\cdot\frac{E(\beta)-\alpha^2F(\beta)}{\beta^2}-\frac{1}{12}\sin^2\left(\frac{\pi a_i}{a}\right)\right]\right\} \end{aligned} \tag{3.3.18}$$

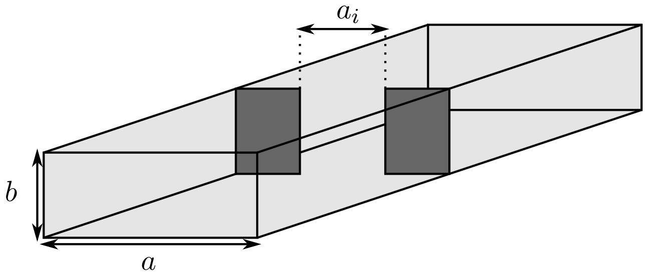

Figure 3.18.: Waveguide inductive iris with aperture dimension of a_i.

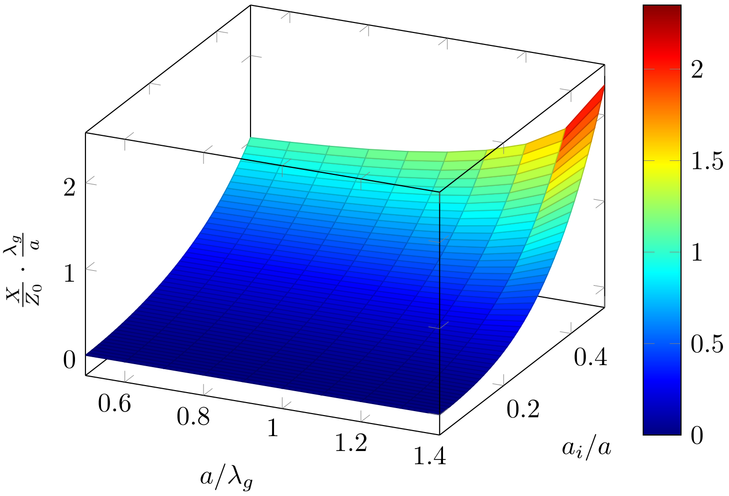

Figure 3.19.: Relation between the iris dimensions and the reactance from Marcuvitz's model [Mar51]. The aperture width a_i is plotted from 0 to $0.5a$ for the waveguide width a varying from $0.5\lambda_g$ to $1.4\lambda_g$.

where λ and λ_g are the free-space and guide wavelength, respectively. $F(\alpha)$ and $E(\alpha)$ are the first and second kind of the complete elliptic integrals. The variables α and β in Eq. 3.3.18 are defined as:

$$\begin{aligned} \alpha &= \sin\left(\frac{\pi a_i}{2a}\right) \\ \beta &= \cos\left(\frac{\pi a_i}{2a}\right) \end{aligned} \tag{3.3.19}$$

The approximation given in Eq. 3.3.18 is valid for a very thin iris and

$$0.5 < a/\lambda < 1.5. \tag{3.3.20}$$

For more flexibility, full wave simulation tools can be employed.

3.3.2 *Design Example of a 3-pole Chebyshev Filter*

The theoretical aspects described in Subsection 3.3.1 will be employed in the filter design. As an example, a 3-pole Chebyshev filter will be used. For the perpendicular state, the center frequency of the filter is 22 GHz with a return loss better than 20 dB at the passband and ripple bandwidth of 600 MHz.

First, the resonator structure should be chosen. A rectangular cavity as described in Section 3.2 is utilized. As a starting point, a resonator fully filled with Rogers RT5880 can be used since its relative permittivity value is close to the value of perpendicular state of LC. With calculations using Eq. 3.1.3 and Eq. 3.2.1, a rectangular SIW resonator with a width $a = 8.1\,\text{mm}$ and length $l_{\text{res}} = 6\,\text{mm}$ gives a resonant frequency at 22 GHz. Insertion of LC will decrease the frequency due to its higher permittivity so that the resonator size should be smaller. By using CST, insertion of an LC cavity with $a_{\text{LC}} = 1\,\text{mm}$ and $l_{\text{LC}} = 4\,\text{mm}$ works at 22 GHz when the resonator width is reduced to $a = 7.8\,\text{mm}$.

The next step is the design of the coupling structure between resonators. Inductive iris coupling is employed. Since the vias are not thin according to Eq. 3.3.20, CST simulation can be performed for the filter design. The coupling structure can be divided into two types: interresonator coupling and input/output coupling [Hon11].

When two resonators coupled to each other, two resonant frequencies appear, which are f_1 and f_2 for the lower and higher frequency, respectively (see Fig. 3.20a). The coupling coefficient k can be extracted from both resonant frequencies using the following equation [Hon11]:

$$k = \frac{f_2^2 - f_1^2}{f_2^2 + f_1^2}. \tag{3.3.21}$$

The value of the coupling coefficient k depends on iris opening a_i. Using two coupled resonators, the effect of a_i is shown in Fig. 3.20b which is simulated using CST Microwave Studio. For the designed filter, the needed k can be found from Eq. 3.3.9 and Eq. 3.3.14. The obtained lowpass element values are $g(0) = g(4) = 1$, $g(1) = g(3) = 0.8533$ and $g(2) = 1.1038$. Since the values of g are symmetric, the interresonator coupling coefficients are also symmetric or $k_{1,2} = k_{2,3} = 0.0281$. From Fig. 3.20b, the initial value of iris width between the first and second resonator is $a_{i,12} = 2.6\,\text{mm}$.

For the coupling between the first or third resonator with the feeder transmission line, a one port simulation of the short circuited resonator is conducted. The external Q-factor Q_e, which is related to the coupling, can be calculated by using the phase response of the reflection coefficient S_{11}. A typical phase response is shown in Fig. 3.21a and the relation between iris opening a_i of the structure and the external Q-factor is shown in Fig. 3.21b. The extracted external Q-factor is [Hon11]:

$$Q_e = \frac{f_0}{\Delta f_{90}}. \tag{3.3.22}$$

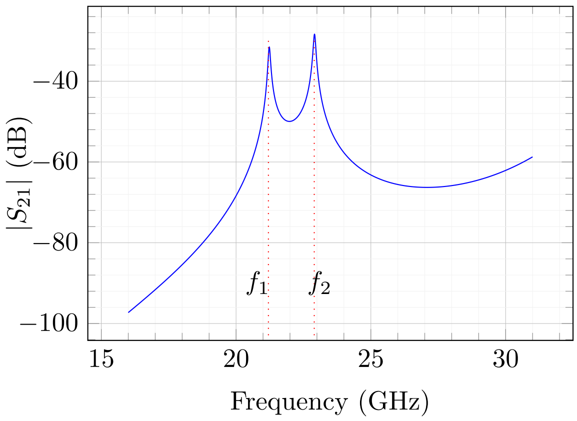

(a)

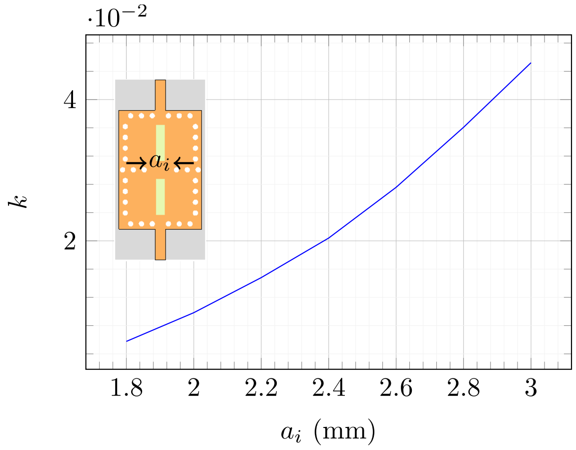

(b)

Figure 3.20.: (a) Typical response ($|S_{21}|$) of a coupled resonator. (b) Relation between the iris width a_i and coupling coefficient k.

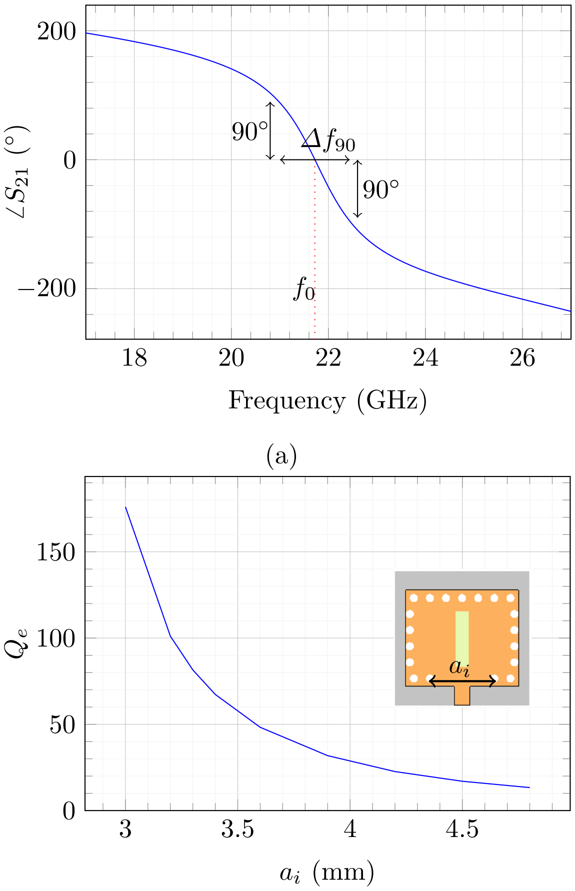

(a)

(b)

Figure 3.21.: (a) Typical response ($|S_{11}|$) of a short circuited resonator. (b) Relation between the iris width a_i and external Q-factor Q_e.

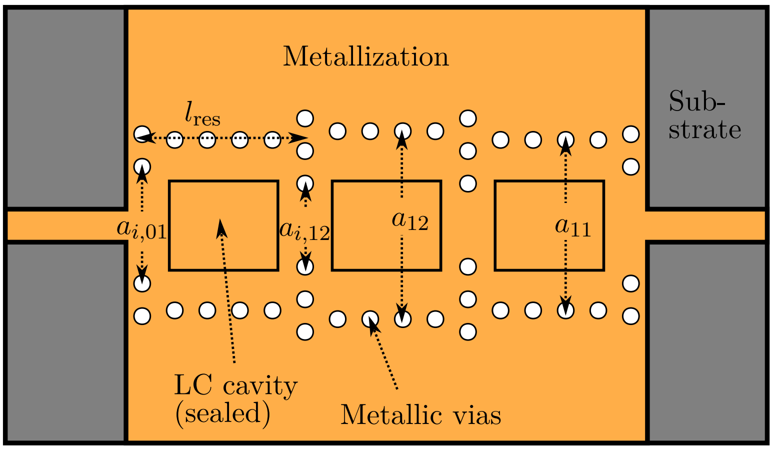

Figure 3.22.: The schematic of 3-pole Chebyshev filter.

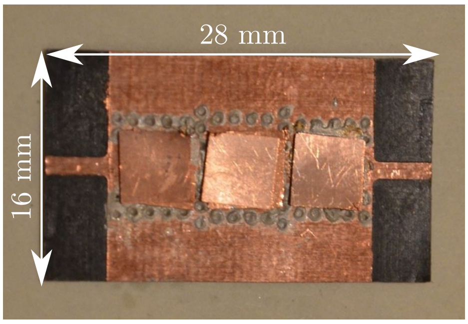

Figure 3.23.: The fabricated filter.

According to Eq. 3.3.14, the needed external Q-factor is 31.3 so that the iris width for the first or third resonator and the feeder line is 4 mm.

However, as already explained in Subsection 3.3.1, a transmission line with a negative length is needed to realize an impedance inverter for coupling. Instead of the resonator length, adjusting the resonator width would be easier to implement in this filter design. The resonator and iris width can be optimized for the whole structure so that an ideal Chebyshev response can be achieved by using CST Microwave Studio. The final structure is depicted in Fig. 3.23. The dimensions of the filter are: $a_1 = 6.58$ mm, $a_2 = 6.92$ mm, $a_{i,01} = 4.3$ mm, $a_{i,12} = 3.06$ mm, and $l_{\text{res}} = 6$ mm.

3.3.3 *Realization of a Tunable 3-pole Chebyshev Filter*

The proposed bandpass filter in Fig. 3.23 is fabricated using the same technique as the resonator in Section 3.2. The fabricated device and simulated filter's responses can be seen in Fig. 3.23 and Fig. 3.24, respectively.

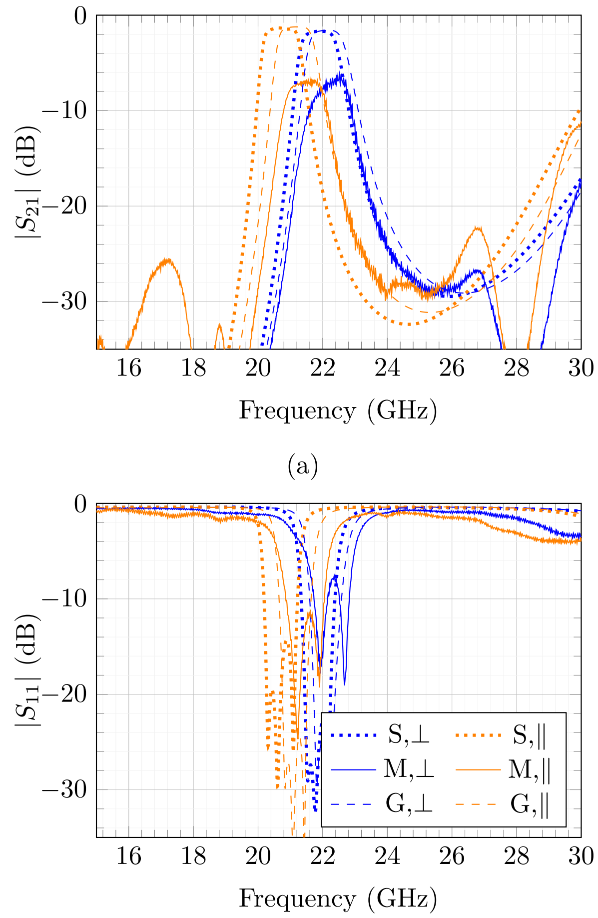

(a)

(b)

Figure 3.24.: Simulation and measurement results of 3-pole filter with Chebyshev response. Note: S = simulation; M = measurement, G = simulation with 0.02 mm air gap; ⊥ = perpendicular state; ∥ = parallel state.

To verify the simulation result, a measurement of the SIW filter is carried out with the same method as the one resonator measurement and also depicted in Fig. 3.24. The measurement results exhibit 6 dB of insertion loss, which is 3 dB higher than the one from simulation. The return loss is around 10 dB with bandwidth varying between 620–780 MHz or a fractional bandwidth of 2.81–3.54 %. The center frequency of this filter is continuously tunable between 21.45–22.06 GHz.

An effort has been made to remove the air gap by LC refilling. However, it still exists in the structure, which could be inferred by higher center frequency (1.2 % higher than simulation) and reduction of tuning range from 1100 MHz in simulation down to 610 MHz in measurements. CST simulations show that an air gap around 0.02 mm in each resonator fits the measurement results well.

This filter will be compared with other tunable filters in Chapter 4, together with the LTCC LC-filled SIW filter.

3.4 ELECTRICAL BIASING TECHNIQUE FOR LC-FILLED SIW DEVICES

As already seen in Section 3.2 and 3.3, tunable SIW devices based on LC can be tuned by using magnetic alignment. Although it is convenient for rapid or lab-scale prototyping, the magnets consume a large space, which make it unfavorable for real applications. In addition, magnetic tuning requires a mechanical re-alignment, which is contradictory to the idea of electrically tunable devices. Therefore, an electric biasing system is needed in an LC-based microwave device.

In a planar structure like MSL, two different voltages are applied on the metallization for biasing purpose. In addition, alignment layers are deposited on the top of each metallization to anchor the LC in the case of a switched-off biasing voltage. However, this biasing technique is only suitable for a structure with an LC layer with thickness less than 100 µm, since the tuning speed is much slower (around 3 minutes for 100 µm-thickness [KSF+11, HKG+14]). Moreover, SIW structures do not have two separated metallizations, making it impossible to apply the biasing voltages.

In this section, an approach has been investigated in order to include the electrical biasing system into the SIW structure, which is fabricated by using PCB technology. Several biasing lines are formed on the surface of the LC sealing material. For LC sealing as well as the biasing system holder, the glass substrate has been employed, which is well known in the planar LC devices fabrication process [Göl10, Kar14].

3.4.1 *Biasing Concepts*

A fully electrical biasing concept is utilized for the tunable SIW device. Thus, rubbed polyimide layers on top of the structure for pre-orientation of LC are not needed anymore. As already explained in Subsection 2.3, the structure itself contains at least four biasing lines or electrodes, allowing to change the direction of the electric fields inside the LC

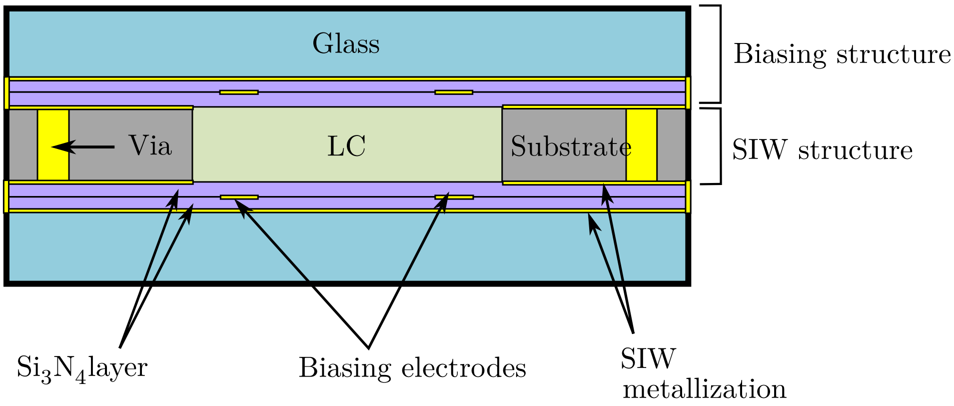

Figure 3.25.: The proposed biasing concept, where the biasing electrode network is glued to the SIW structure by using two components metallic glue.

cavity. A certain voltage is applied to each line. In general, there are two voltages: V_0 and V_b, which are fixed and tunable voltage, respectively. By tuning the voltage V_b from $-V_0$ to V_0, not only the perpendicular and parallel state of the LC orientation can be reached, but also intermediate states.

This concept of tuning is already applied in [WNG+13b], [FGPJ14] and [SGK+15]. However, the existence of resistive lines, which connect all of the top electrodes and also all of the bottom electrodes, can reduce the performance of the device. In general, resistive lines should be transparent to the high frequency field. However, when perpendicular configuration is set, a current can flow in the top and in the bottom electrodes because of the voltage difference, namely V_0 and $-V_0$. Unwanted power dissipation occurrs, and moreover, self-heating due to the dissipated power alters the property of LC inside the device.

The proposed biasing scheme does not use current flow for biasing. Four electrodes are separated from each other and also insulated by a thin layer of dielectric. For this purpose, silicon nitride (Si_3N_4) is used, which has an excellent breakdown voltage of 600 V/µm [Ric15]. Therefore, a thin insulation layer can be fabricated, which does not affect the high frequency fields. A Si_3N_4 layer with thickness of 1 µm is chosen for the biasing structure. The detailed structure is depicted in Fig. 3.25.

3.4.2 *Fabrication Process*

The biasing line fabrication process is shown in Fig. 3.26. A standard photolithography process, which its parameters are detailed in Appendix A, is used to build the biasing structure with a glass as the substrate. The metallic layer consists of a 20 nm-thick chromium and a 60 nm-thick gold layer are evaporated consecutively to the surface of the glass. This first metallization layer serves as metallic ground of the SIW structure.

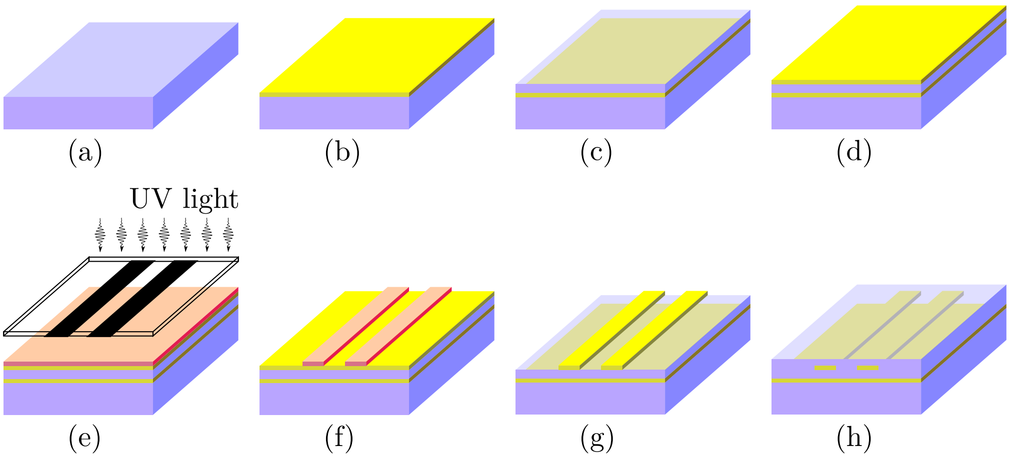

Figure 3.26.: Fabrication scheme of the biasing structure (not to scale). (a) Glass is chosen as the substrate material. (b) The first metallization layer is deposited in the glass surface by evaporating Cr and Au. (c) Si_3N_4 is deposited by PECVD. (d) The second metallization layer is formed using the same method as the first metallization layer. (e) Photoresist is coated in the second metallization layer to create the biasing line. An appropriate mask is placed in the top of it and the structure is exposed with UV light later on. (f) The exposed photoresist is developed. (g) Etching of the metallic layers. (h) Adding the second Si_3N_4 layer.

The next step is the Si_3N_4 deposition by means of plasma-enhanced chemical vapor deposition (PECVD). The second metallization layer with the same composition as the first one is applied on top of the first Si_3N_4 layer and afterwards etched to form the electrodes. Last, the second Si_3N_4 layer is placed on top of the electrode layer. The same process is repeated to the top glass. A hole with a diameter of 0.5 mm is drilled into the glass for LC injection to the SIW device. Finally, the bottom and top glasses are glued together by using two components metallic glue with the SIW device to seal the cavity. After LC injection in a vacuum chamber, the LC-filling hole is closed with glue to ensure that there are no LC leakages in the device.

A sample of a fabricated biasing structure can be seen in Fig. 3.27.

3.4.3 *Technological Verification on a Tunable Delay Line*

To investigate the performance of the fabricated biasing line, a simple SIW structure, a phase shifter, is designed, using the tunable delay line concept (see Section 2.4). In order to create this tunable delay line, a rectangular hole is milled in the center of the SIW transmission line as LC container. Later, this hole will be sealed by the proposed biasing

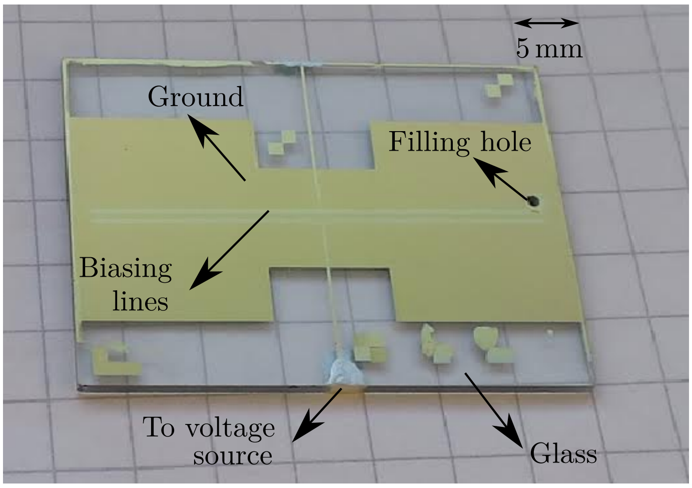

Figure 3.27.: A sample of fabricated biasing structure.

structure as depicted in Fig. 3.27. The behavior of this SIW phase shifter resembles a partially LC-filled rectangular waveguide with TE_{10} mode.

The structure of the phase shifter itself is shown in Fig. 3.28, using Rogers RO4003 as a substrate material ($\varepsilon_r = 3.38$, $\tan\delta = 0.0027$ [Rog16a]) which is manufactured by Eurocircuit[†]. A 50 Ω GCPW line is used to connect the SIW phase shifter and the probe, which is connected to the VNA. A transition between the GCPW and SIW structure has also been designed by using a tapered center line of the GCPW, providing good field and impedance matching [CW09]. For the verification purpose, the device is intended to provide a differential phase shift of 90° and the related dimensions are shown in Fig. 3.28. From simulation using CST as shown in Fig. 3.29, a maximum differential phase shift ($\Delta\phi_{\mathrm{max}}$) of 94° is obtained with a maximum insertion loss ($\mathrm{IL}_{\mathrm{max}}$) of 1.05 dB at 20 GHz. The simulation yields a figure of merit (FoM) of 89 °/dB at 20 GHz.

The measurement results are plotted in Fig. 3.30 and Fig. 3.31. The maximum return loss (6 dB) is higher than the simulation result (better than 10 dB) at the operating frequency. This is caused by a mismatch between the GCPW line and the probes, which connect the device to the VNA. As a consequence, the insertion loss is also higher, up to 2.8 dB. With a differential phase shift of 88°, the obtained FoM is 32 °/dB.

Another important thing to be discussed is the response time, which is defined as the required time to tune from 10 % of maximum phase shift to 90 %. By measuring the phase shift at 20 GHz, the change of the phase shift could be observed as depicted in Fig. 3.32. The measured response time according to the definition is 5 s with maximum voltage of $V_0 = 100\,\mathrm{V}$.

The drawback of this fabrication technique is the integration of the biasing structure to the device. A smooth surface is required to align both structure properly and also to

---

[†] `http://www.eurocircuits.com/`

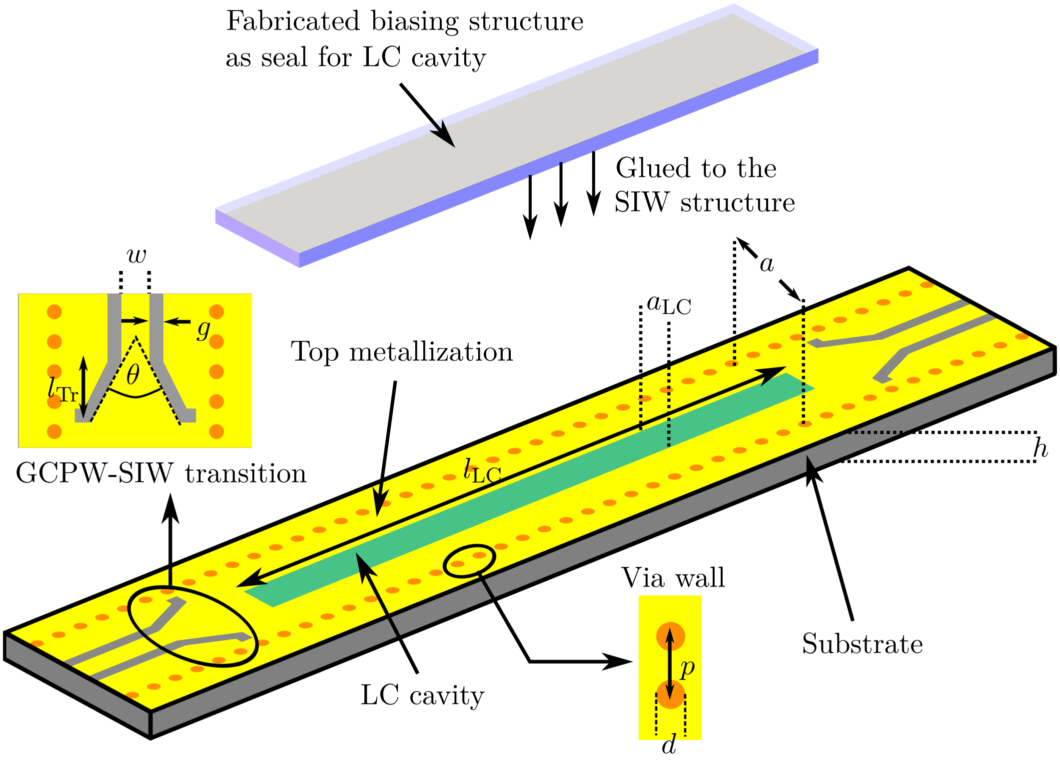

Figure 3.28.: The structure of the designed tunable SIW phase shifter. The following dimensions are chosen in the design: $a = 6.5\,\text{mm}$, $a_{\text{LC}} = 2\,\text{mm}$, $l_{\text{LC}} = 30\,\text{mm}$, $h = 0.5\,\text{mm}$, $d = 0.6\,\text{mm}$, $p = 1.2\,\text{mm}$, $l_{\text{Tr}} = 2.3\,\text{mm}$, $\theta = 53°$, $w = 1.2\,\text{mm}$ and $g = 0.6\,\text{mm}$. The cavity will be sealed by gluing the biasing structure (Fig. 3.26) on the top and bottom of the SIW.

seal the SIW structure. This would be a problem if LPKF ProConduct Paste is used as the via material like in Section 3.2.1. In [Rah15] it is shown that the FoM is decreased to 8.77 °/dB for a SIW structure with LPKF vias. A resonator is also fabricated with an unloaded Q-factor in the range of 26–30 , which is lower than the standard Q-factor for planar filter. Therefore, a technology which can integrate both biasing structure and the device is desirable, for example multilayer technologies. Low temperature co-fired ceramic (LTCC) is a possible solution which will be discussed in the next chapter.

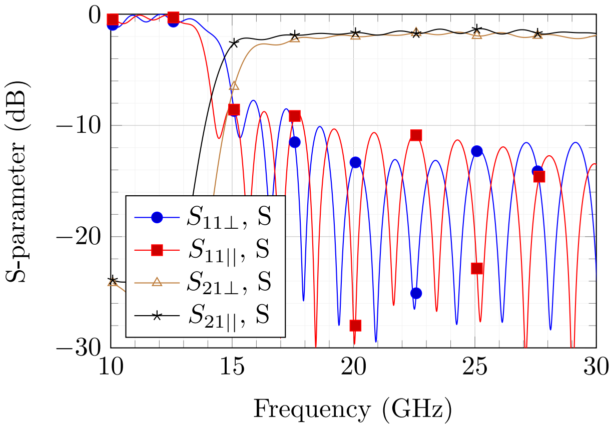

Figure 3.29.: Simulated S-parameters of the phase shifter. Note: S = simulation; ⊥ = perpendicular; ∥ = parallel.

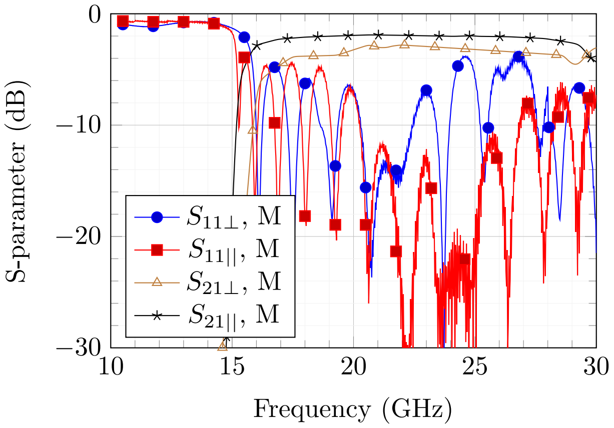

Figure 3.30.: S-parameter measurement results of the fabricated phase shifter. Note: M = measurement; ⊥ = perpendicular; ∥ = parallel.

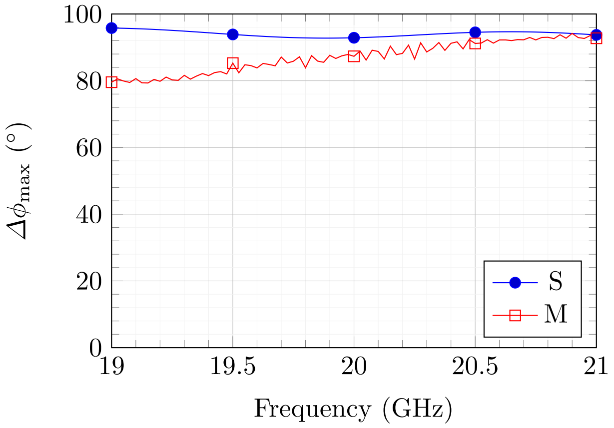

Figure 3.31.: Simulation and measurement results for the maximum differential phase shift $\Delta\phi_{\max}$. Note: S = simulation; M = measurement.

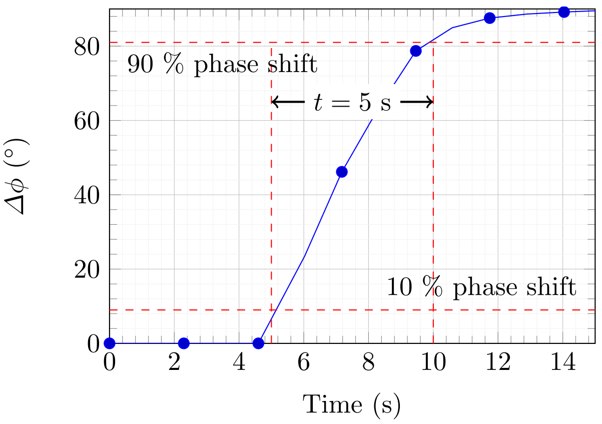

Figure 3.32.: Response time of the LC-based SIW phase shifter.

4

FULLY-INTEGRATED FILTERS AND AMPLITUDE TUNER IN LOW TEMPERATURE CO-FIRED CERAMIC (LTCC) TECHNOLOGY

To overcome the difficulties encountered in PCB technology in Chapter 3, especially in the biasing circuit fabrication, low temperature co-fired ceramic (LTCC) technology is investigated. This technology uses several layers of glass-ceramics composite as the dielectric substrate. In addition to the planar metallizations, the fabrication process of the LTCC technology also supports thin resistive layers, metallic vias and cavities [Wol09]. Therefore, the integration of the biasing circuit with the LC-based tunable device will be easier than the PCB technology. The fabrication process itself will be discussed in Section 4.1.

Next, a tunable LC-filled SIW filter is proposed in Section 4.2. Similar as in Chapter 3, resonators and 3-pole Chebyshev bandpass filters are investigated. Electrical biasing method is employed in this section.

In addition, another device, which is the LC-based amplitude tuner, is also proposed for the first time and will be discussed Section 4.3. This device alters the amplitude of a microwave signal with the help of LC-based phase shifter.

The tunable microwave devices in this chapter is a part of Liquida K project, which is a cooperation between Institute of Microwave Engineering and Photonics of TU Darmstadt, German Aerospace Center (DLR), Federal Institute for Materials Research and Testing (BAM), and IMST GmbH. In accordance with the project specification, the devices is designed for operating frequencies around 30 GHz.

4.1 LTCC PROCESSING TECHNOLOGY

As the part of Liquida K project, the proposed devices are processed by BAM using LTCC technology. The general overview of the fabrication process can be seen in Fig. 4.1. The LTCC substrates are prepared and later punched to form the cavities and LC-filling hole, as well as the via holes. The LC-filling hole has a diameter of 0.5 mm, which is used for all of the devices in this chapter. For the via holes, metallic paste is filled into the holes so that the metallic vias are formed. The next step is the fabrication of the planar metallizations, which is done by screen printing technique. After that, the printed LTCC

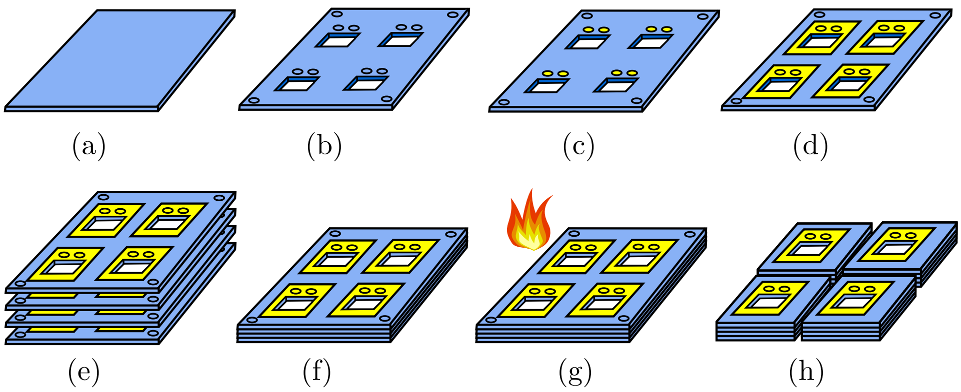

Figure 4.1.: The fabrication step with LTCC technology: (a) susbstrate or green tape preparation, (b) cavity and via forming, (c) via filling with gold paste, (d) fabrication of metallic layer by screen printing, (e) stacking, (f) lamination, (g) firing and (h) singulation. Source: BAM.

layers are stacked and laminated. For the firing process, the devices are sintered with a peak temperature of 865 °C for 20 min. This temperature is relatively low compared to the melting point of good conducting material such as gold and copper, creating a possibility to realize microwave devices. The sintering process cause shrinkages of 8.9 % and 10.6 % for the lateral and thickness direction, respectively. These shrinkages are already compensated before fabricating the device. Finally, the LTCC laminate is cut out so that every single device is obtained.

Note also that the LC cavity is automatically closed during the LTCC fabrication process. After the fabrication, the LC is injected through the filling hole in a vacuum chamber. By using two components glue, the filling hole is sealed to prevent the LC leakage.

As for the materials, DuPont GreenTape 9K7 is used as the LTCC substrate, which has relative permittivity of 7.1 and loss tangent of 0.0015 [DuP09b]. The loss tangent is relatively low for microwave applications, for example compared to Rogers RO4003 in Chapter 3. Each green tape layer has a thickness of 107 µm after the sintering process. All of the metallizations inside the LTCC are made from gold pastes, which are LL505 for the planar metallization and LL500 for the via filling. Each of them has a conductivity of 1.33×10^7 S/m*. This is lower than the conductivity of the pure gold (4.42×10^7 S/m). Nevertheless, this conductivity is still higher than LPKF ProConduct paste used in the PCB fabrication process so that a lower metallic loss is expected. All of the biasing lines are made of a resistive paste 2061 with a resistivity of 200 kΩ/□. This paste is almost transparent to the high frequency field but it is resistive for the DC or low frequency biasing signal. The biasing method is similar to the proposed method in Chapter 3, which utilizes no current, unlike in [SGK+15]. The thickness of both planar metallizations and

---

* The conductivity is calculated from the resistivity value in [DuP12] and [DuP09a].

resistive lines are 10 µm. For the LC, GT3-23001 from Merck is used with following properties: $\varepsilon_{r,\perp} = 2.47$, $\varepsilon_{r,\parallel} = 3.16$, $\tan\delta_{r,\perp} = 0.0151$ and $\tan\delta_{r,\parallel} = 0.0033$. All of these materials are qualified for space applications [GMG+09, FGPJ14], which give an advantage compared to the other tuning technologies.

4.2 ELECTRONICALLY TUNABLE SIW FILTER

In this section, an electrically tunable SIW resonator and 3-pole filter will be constructed by using this LTCC technology. Before discussing about the SIW structures, the feeding network, which connects the structures with the VNA for measurement, will be presented first.

4.2.1 *Transition from SIW to Grounded Coplanar Waveguide*

The grounded coplanar waveguide (GCPW) topology is used to connect the SIW structure and the high frequency signal source or VNA with the help of a device called wafer prober. The positive electrode for the high frequency signal is placed in the center, separated from the ground pads by certain gaps (on the left and right side). The width of the signal electrode and gaps are 0.4 mm and 0.2 mm, repectively. These dimensions are chosen to provide a line impedance of 50 Ω.

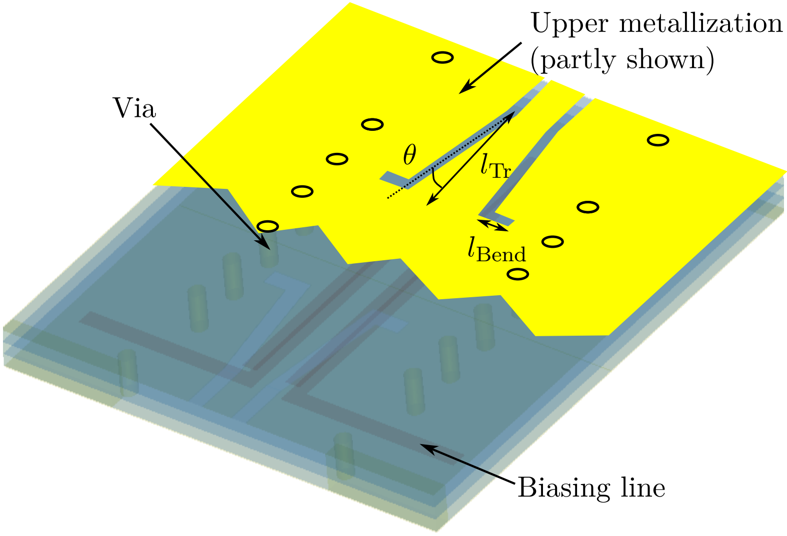

Figure 4.2.: Simulation model of back-to-back transition between GCPW and SIW. Some vias in the GCPW part is deleted to connect the biasing line with the external voltage sources. The following dimensions are used: $l_{\mathrm{Tr}} = 1.55$ mm, $\theta = 8.55°$, and $l_{\mathrm{Bend}} = 0.4$ mm.

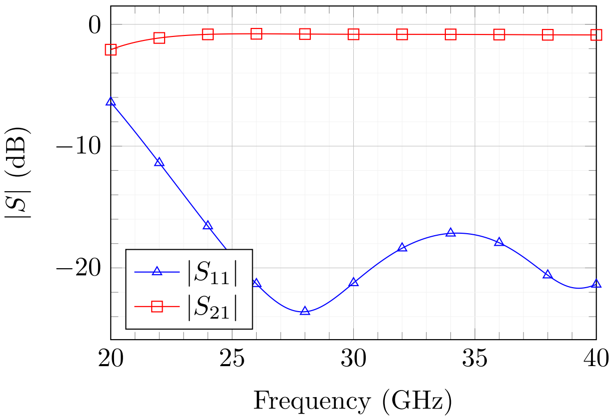

Figure 4.3.: Simulation results of back-to-back transition between GCPW and SIW.

To connect this GCPW line to SIW structure, a transition between those two structures is needed. Same as in Section 3.4, a tapered line and 90° bend are used as shown in Fig. 4.2, which is a modification from [CW09]. The dimensions are: $l_{\mathrm{Tr}} = 1.55\,\mathrm{mm}$, $\theta = 8.55°$, and $l_{\mathrm{Bend}} = 0.4\,\mathrm{mm}$. As already shown in Section 3.4, biasing lines are compulsory for electric biasing. Since the connections with external voltage sources are required, some vias in the GCPW part are deleted. To examine the response of the transition, a CST simulation is conducted by using two transitions connected together (back-to-back configuration). The S-parameters are depicted in Fig. 4.3. It is shown that $|S_{11}|$ is below $-20\,\mathrm{dB}$ at 30 GHz, while $|S_{21}|$ around $-1\,\mathrm{dB}$. This insertion loss will be taken into account for the analysis of the resonator and filter in Subsection 4.2.2 and 4.2.3, respectively.

4.2.2 *Concept of Electrically Tunable SIW Resonator*

Concept, Design and Performance Analysis

As a building block for bandpass filters, the properties of a single LC resonator is investigated. The structure is shown in Fig. 4.4. According to Eq. 3.2.1 and 3.1.3, the following dimensions are suitable for a resonance frequency around 30 GHz: $a_{\mathrm{res}} = 3\,\mathrm{mm}$, $l_{\mathrm{res}} = 2.95\,\mathrm{mm}$, $d_{\mathrm{via}} = 0.2\,\mathrm{mm}$ and $p_{\mathrm{via}} = 0.6\,\mathrm{mm}$. The distance between the via structures and the LC cavity is 0.4 mm, which is chosen due to the fabrication limitations at BAM. A hole is also punched at the top of the cavity, having a diameter of 0.5 mm. For the biasing lines, resistive paste is used (see Fig. 4.4). The total number of LTCC layers used for the structure is four. The LC cavity itself is placed in layer 3.

To check the maximum achievable unloaded Q-factor, a CST simulation can be performed using an unfilled cavity, which is the same as in Chapter 3. However the center frequency of the resonator increases to above 40 GHz due to the decreasing permittivity

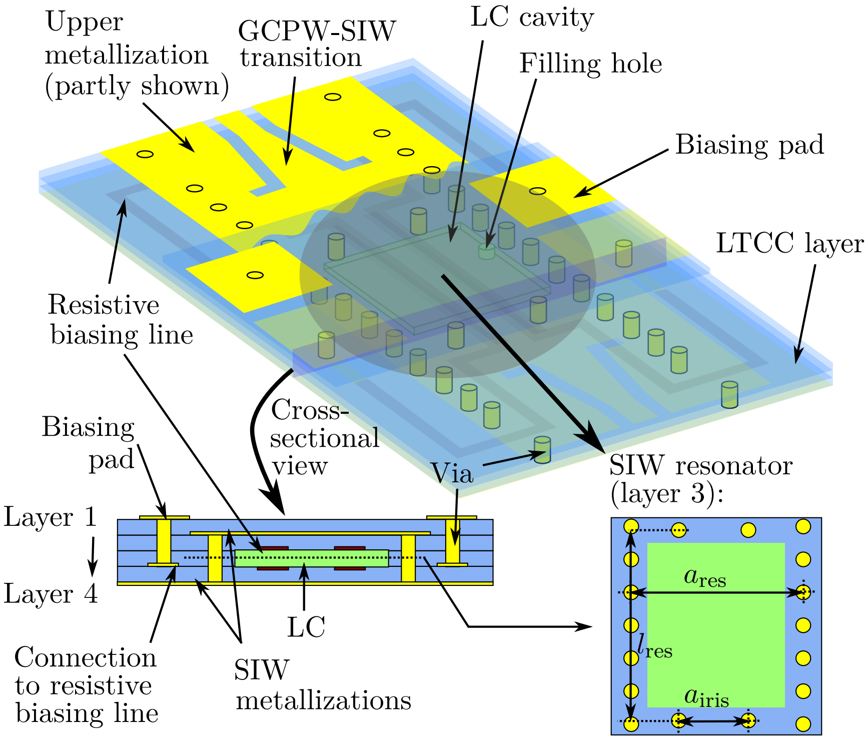

Figure 4.4.: LTCC-LC-based tunable resonator with four LTCC layers. The LC cavity is placed in layer 3.

inside the cavity as indicated from the simulation results in Fig. 4.5a. Since the difference in the operating frequency is quite big (more than 33 %), a simulation with lossless materials has been performed. The simulation results are depicted in Fig. 4.5b. The respective unloaded Q-factors are summarized in Table 2.

The effect of each material and also the filling hole are examined in the simulation. First, the lossless materials are used for simulation (case A) to check the losses caused by radiation. This is possible because the SIW design rules in Eq. 3.1.1–3.1.2 are not fulfilled. However, this effect is small as can be inferred from the negligible insertion loss (only 0.04 dB).

The metallic losses are examined in cases B and C. The losses caused by the metallization is larger than for radiation. Pure gold and gold paste are used for this two cases and all of the dielectric materials are assumed to be lossless. The Q-factor for the structure with gold paste is lower compared to the pure gold structure due to its lower conductivity. Nevertheless, the Q-factor is still better than the structure with LPKF ProConduct paste in Chapter 3.

By using lossless metallizations, the contribution of dielectric losses are simulated in case D and E. While the LTCC does not show much effect, the LC has the largest contribution to the Q-factor reduction. The perpendicular case is used in this simulation,

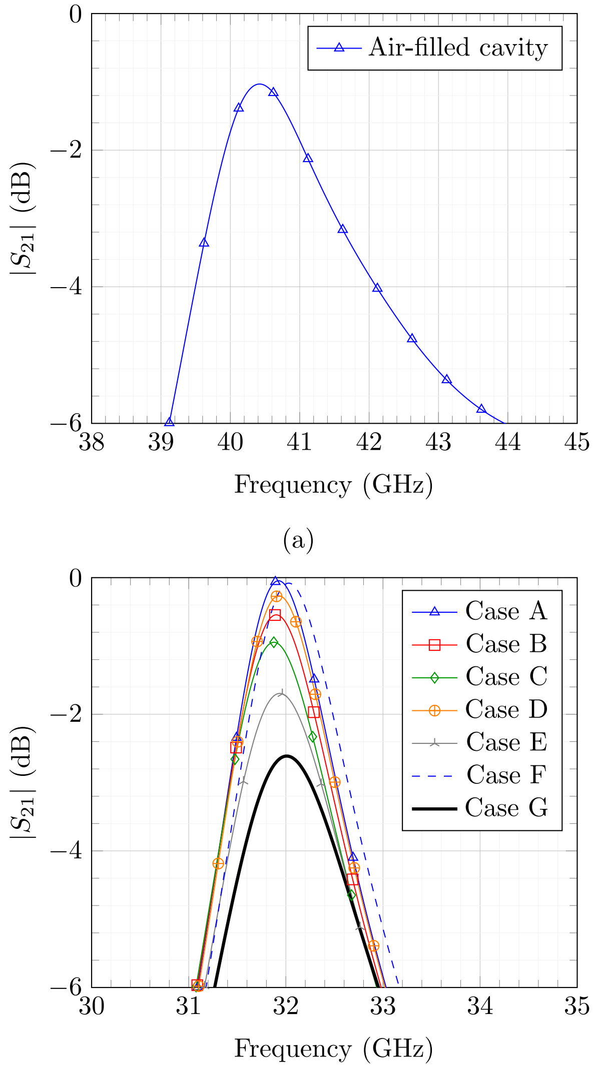

(a)

(b)

Figure 4.5.: Simulation results of the resonator structure: (a) unfilled LC-cavity and (b) LC-filled cavity, where various loss mechanisms are taken into account according to Table 2.

Table 2.: Effect of the material losses of the resonator on the unloaded Q-factor.

Case	Insertion Loss (dB)	Unloaded Q-factor
A: Ideal case	0.04	5600
B: Lossy metallization (gold)	0.54	445
C: Lossy metallization (gold paste)	0.95	246
D: Lossy LTCC	0.26	926
E: Lossy LC (perpendicular case)	1.7	130
F: Ideal with filling hole	0.08	2952
G: Whole structure	3	69

which has a higher loss tangent. For the filling hole, the effect is not that much with less than 0.1 dB insertion loss in case F. The hole gives a small center frequency shift at around 100 MHz.

Finally, the whole structure along with each loss mechanism is simulated (case G) and the final unloaded Q-factor is 69. All of the Q-factors are calculated using Eq. 3.2.12 in Chapter 3.

By using the properties of the LC GT3-23001, two extreme resonant frequencies are obtained around 30 GHz as shown in Fig. 4.6. The obtained unloaded Q-factors are 69 and 118 for the perpendicular and parallel case, respectively. The resonance frequencies are varying from 30.3–32.0 GHz resulting in a tunability of 5.31 %.

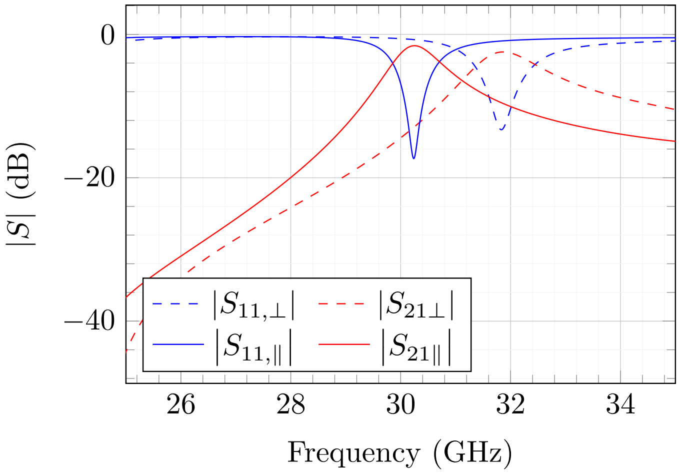

Figure 4.6.: Simulation results of a single LC-LTCC resonator using CST.

However, the full tuning range cannot be achieved later in the measurements, due to imperfect alignment of the LC directors. As shown in Fig. 4.7, the directors are not perfectly perpendicular or parallel to the RF fields, but follow the direction of the biasing fields. Therefore, the extreme effective permittivities of the LC inside the cavity are no

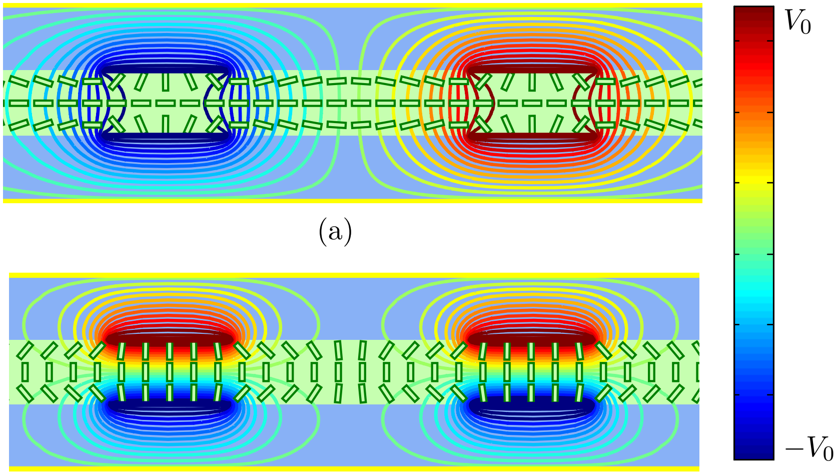

(a)

(b)

Figure 4.7.: The director distribution in the middle of the LC-cavity for (a) perpendicular and (b) parallel state.

longer $\varepsilon_{r,\perp}$ and $\varepsilon_{r,\|}$ anymore, but in-between those values. This effective permittivity can be predicted by using the simulation tools from [GGMJ08]. By using a transmission line with the same cross section as the resonator, a comparison can be made between the LC-filled cavity and the homogenous-material-filled cavity to predict the effective permittivity $\varepsilon_{r,\mathrm{eff}}$ of the LC inside. The graph in Fig 4.8 shows the relation between the relative permittivity of the homogenous material as the cavity filling and the propagation constant β of the structure. From the simulation tool, the obtained propagation constant for LC in perpendicular and parallel state are 847 rad/m and 945 rad/m, respectively, so that the predicted effective permittivity of the LC are the followings: $\varepsilon_{r,\mathrm{eff},\perp} = 2.64$ and $\varepsilon_{r,\mathrm{eff},\|} = 3.14$.

Using CST, this structure is re-simulated and the center frequency varies from 31.4 GHz at perpendicular state to 30.3 GHz at parallel state (tunability of 1100 MHz or 4 %) as can be seen in Fig. 4.9. Since the resonant frequency is inversely proportional to the square root of the material permittivity, the frequency shift in perpendicular state is more perceptible. The obtained unloaded Q-factors are 69 for the perpendicular state and 118 for the parallel state. Note that the parallel state always has the better Q-factor due to its lower loss tangent.

Measurement Results and Discussion

After the fabrication process, measurements had been performed. The fabricated resonator is shown in Fig. 4.10. Voltages of V_0, $-V_0$, V_b and $-V_b$ were applied to each biasing pad. Two ground-signal-ground (GSG) probes with a pitch of 1250 µm connect the GCPW part of the structure with the VNA. The measurement setup can be seen in

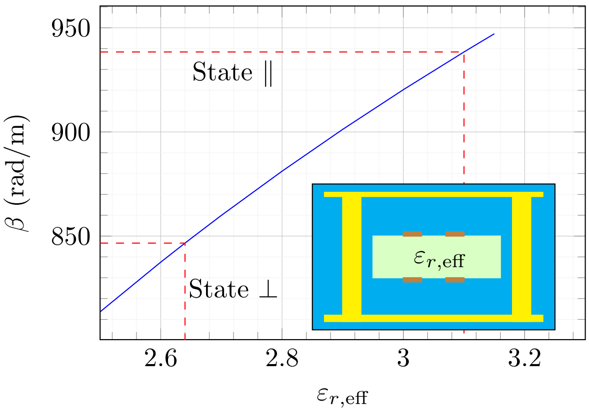

Figure 4.8.: The effective permittivity of LC for the proposed resonator structure.

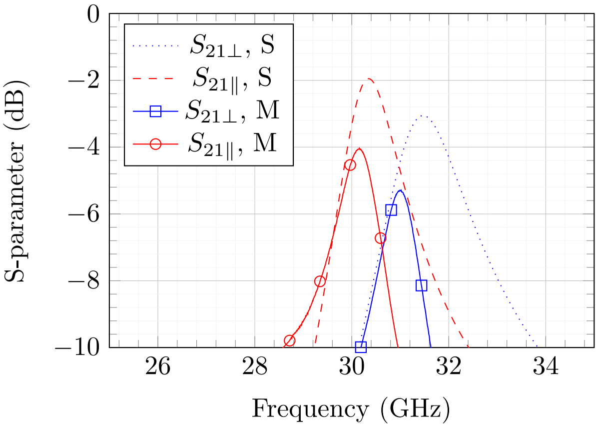

Figure 4.9.: Re-simulation (S) and measurement (M) results for an LC-filled SIW resonator, taken into account of the LC director imperfection.

Fig. 4.11. The S-parameter measurement results are depicted in Fig. 4.9. The tuning range is reduced into 30.16–31 GHz (840 MHz or 3 %) possibly due to the fabrication tolerance. The Q-factors are 68–100 , which are close to the range of the expected Q-factor obtained from the simulation. To achieve the extreme states, the maximum voltage needed is 80 V both for V_0 and V_b.

In addition to the S-parameters, the response time of this resonator is also measured. For this purpose, continuous wave measurements at a single frequency are performed, which provide a better recording speed compared to the measurement for whole frequency range [Göl10]. Since the center frequency cannot be measured by this method, the phase of the filter ($\angle S_{21}$) can be exploited since it is related to the center frequency f_0 of the filter. Fig. 4.12 shows the phase measurement of the filter with several values of V_b: −80 V,−50 V,0 V and 80 V. At 30.5 GHz, which is the center of the tuning range of the

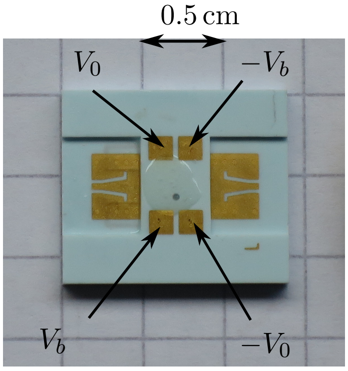

Figure 4.10.: Fabricated tunable SIW resonator along with the biasing configuration.

Table 3.: Comparison of the response time of various LC-based devices.

Topology	h_{LC}†	Range V_b	t_{rise}	t_{fall}
MSL phase shifter [KSF+11]	100 µm	0–15 V	4.6 s	175.8 s
Varactor-loaded line [HKG+14]	10 µm	0–40 V	<1 s	3 s
Waveguide phase shifter and filter [WNG+13a, FGPJ14]	<3 mm	±200 V	Few min.	Few min.
SIW resonator, this work	107 µm	±80 V	2 s	1.5 s

filter, the phase decreases as the center frequency decreases. The possible phase values are between −54° and 12°, which are the phases for the extreme states.

Since the phase represents the center frequency, the definition of the response time from the tunable delay line concept can be borrowed, which is the required time to tune from 10 % to 90 % of the maximum differential phase shift for rise time (t_{rise}) and vice versa for the fall time (t_{fall}). The plot of time versus the differential phase shift ($|\angle S_{21} - \angle S_{21}(f_0)|$) presented in Fig. 4.13. The obtained response time is 2 s and 1.5 s for rise and fall time, respectively.

This measured time is comparable to the most of the planar LC-based devices, as shown in Table 3. For the fall time, the proposed SIW device has even a better switching speed. This is different than the most of the planar LC structures, for example in [KSF+11, HKG+14], where the fall time is usually longer due to the usage of the weak anchoring force from the alignment layer. Both of the extreme states in this work are controlled by strong biasing voltage or electric field, so that the rise and fall time are almost the same. Despite their better Q-factor (or FoM for a phase shifter), the LC-based waveguide devices have slower response (in order of minutes) compared to the proposed SIW structure due to their thick LC layer.

---

† Thickness of LC layer

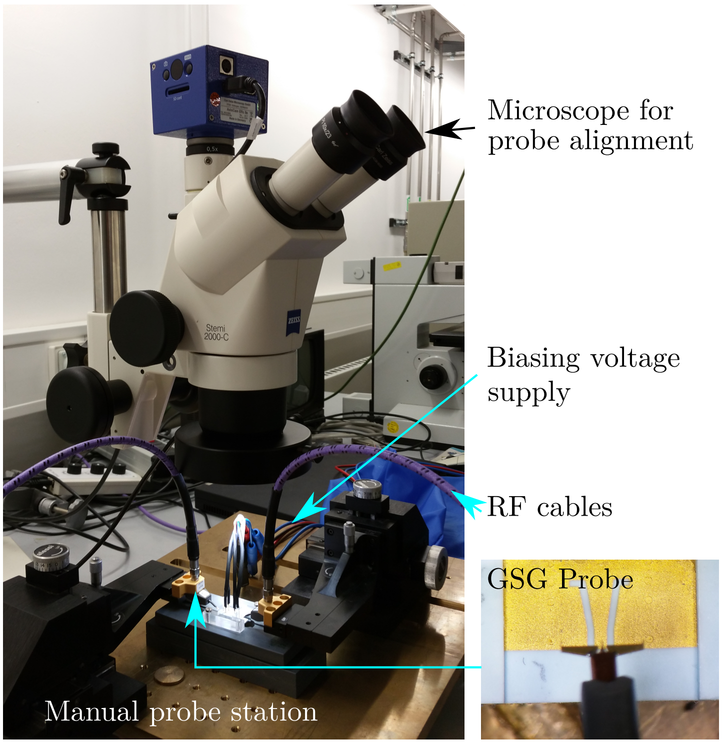

Figure 4.11.: The measurement setup used for the resonator and filter. A manual probe station is employed along with two GSG probes.

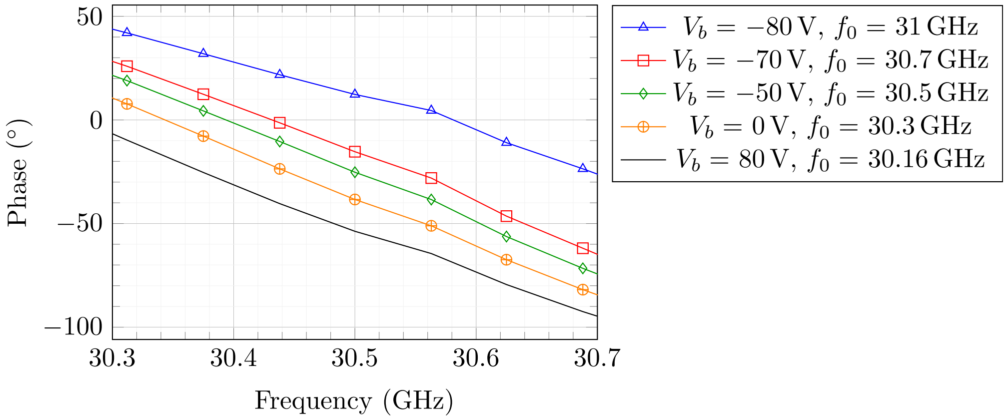

Figure 4.12.: The measured phase of SIW resonator at around 30.5 GHz.

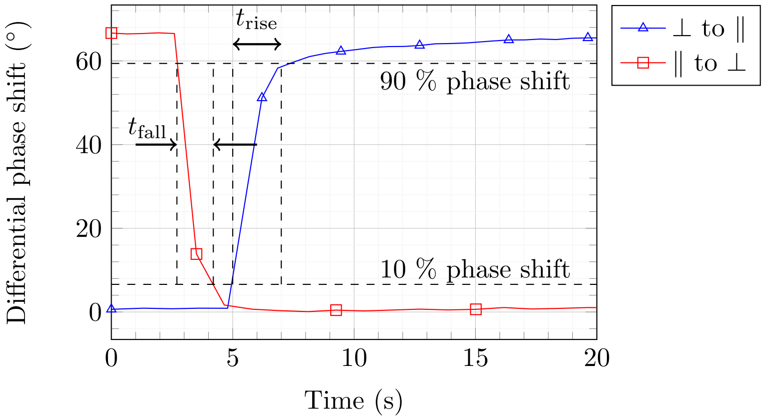

Figure 4.13.: Response time measurement of the SIW resonator at 30.5 GHz. Since the center frequency measurement is impossible in continuous wave mode, the differential phase shift is employed to determine the rise and fall time.

4.2.3 *Electrically Tunable 3-pole SIW Bandpass Filter*

The LC-filled SIW resonators can be cascaded to form a bandpass filter. Designed for a center frequency around 30 GHz, the structure depicted in Fig. 4.14 is simulated using CST. This filter is a 3-pole Chebyshev filter designed for a 3 GHz ripple bandwidth with the same design method described in Chapter 3. The following dimensions are yielded after the design: $l_{\text{res},1} = 2.89\,\text{mm}$, $l_{\text{res},1} = 2.95\,\text{mm}$, $a_{i,01} = 1.89\,\text{mm}$, $a_{i,12} = 1.6\,\text{mm}$ and $a = 3\,\text{mm}$. Using the obtained value of LC's effective permittivity in Subsection 4.2.2, the simulation yields a center frequency tuning range of 29.4–30.2 GHz as can be seen in Fig. 4.15.

The fabricated filter, which is also shown in Fig. 4.14, is measured with the same procedure as the single resonator. The measurement gives almost similar results, 29.4–30.1 GHz or 700 MHz (Fig. 4.15). The difference can be seen on the return loss which is reduced to 6 dB due to imperfect transition at the GSG probes. The filter has a minimum insertion loss from 2 dB at the parallel state up to 4 dB at the perpendicular state with a ripple up to 3 dB. The fractional ripple bandwidth for both state has a small difference: 11.6 % at perpendicular and 11.2 % at parallel state.

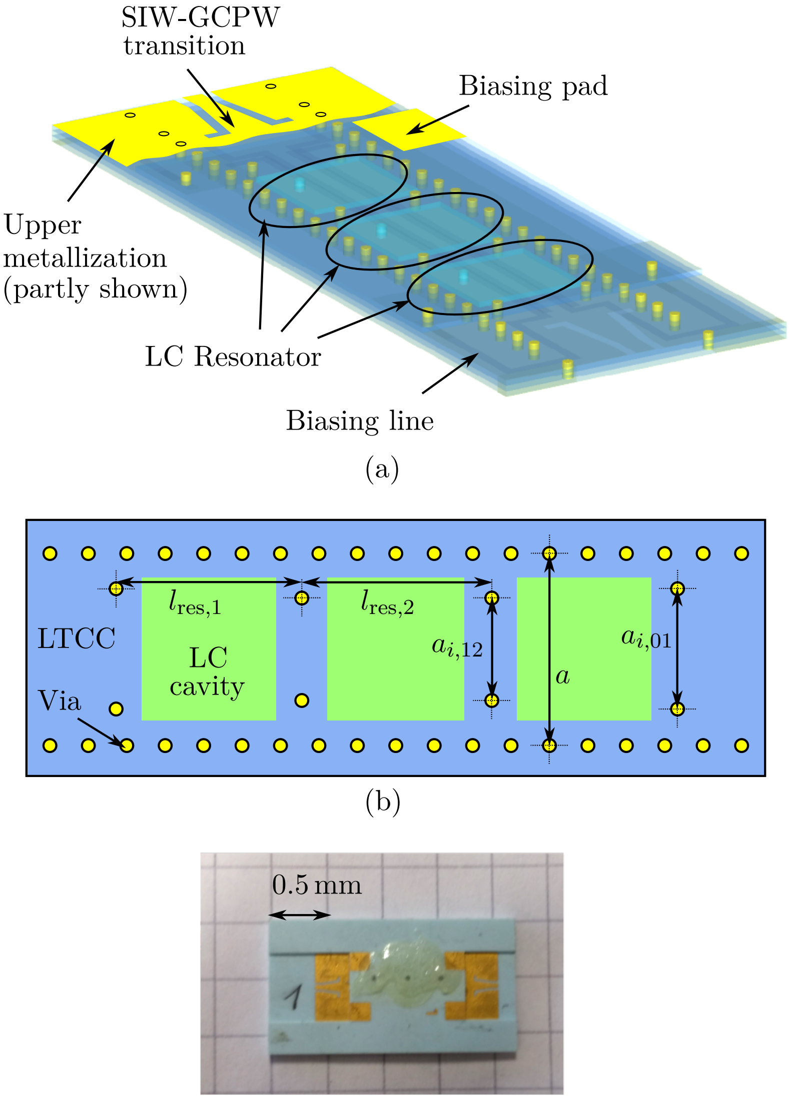

(a)

(b)

(c)

Figure 4.14.: 3-pole tunable filter using LTCC: (a) CST simulation model, (b) detailed view of the resonators and (c) fabricated device. The following dimensions are used: $l_{\mathrm{res},1} = 2.89\,\mathrm{mm}$, $l_{\mathrm{res},1} = 2.95\,\mathrm{mm}$, $a_{i,01} = 1.89\,\mathrm{mm}$, $a_{i,12} = 1.6\,\mathrm{mm}$ and $a = 3\,\mathrm{mm}$. Note that the structure is symmetric.

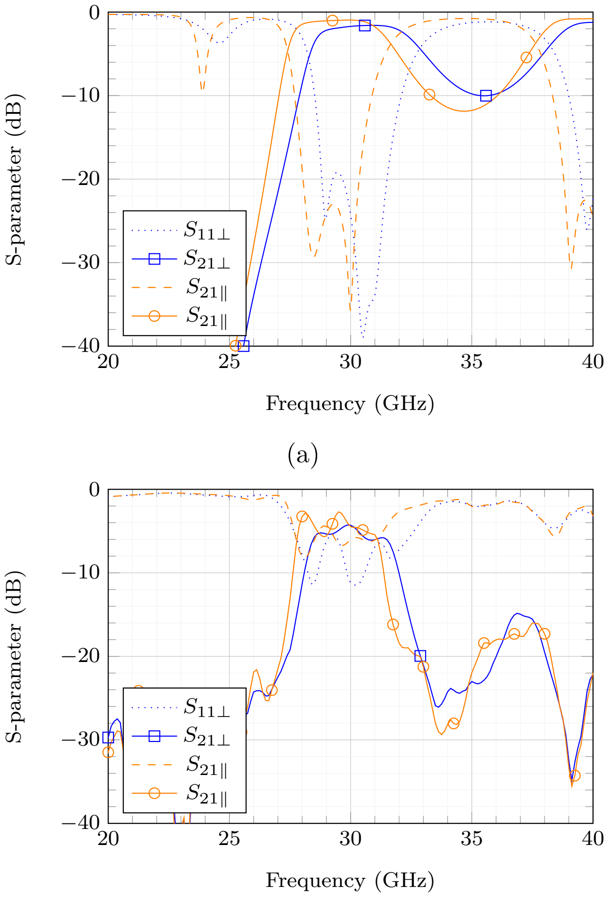

(a)

(b)

Figure 4.15.: (a) Simulation and (b) measurement results of the 3-pole filter.

Table 4.: Comparison of tunable resonators and filters with various tuning technology.

Topology	Tuning Element	n[‡]	f_0 (GHz)	IL (dB)	FBW (%)	Q_u
SIW [ZSM^{+}11]	BST	2	2.95–3.57	3.3	5.4	up to 66
SIW [SAE11]	MEMS	2	1.2–1.6	2.2–4.1	3.2–4.3	93–132
SIW [SMTB11]	Varactor	1	2.6–3.1	25–45*	0.7–2.5	40–150
SIW [AGW13]	Ferrite/Varactor	2	10.8–11.9	1–2	4–4.1	up to 130
PLL[§] [GGK^{+}10]	LC	3	18.5–20.5	8–10	4–9	25–31[¶]
Microstrip [YFB^{+}12]	LC	1	2.7–2.9	0.97–1	22–25	37–43
PCL[‖] [YMS12]	LC	3	31–34	4.4–5.6	5.46–7.25	22–28 [¶]
Waveguide [FGPJ14]	LC	3	19.7–20.1	5–7	1.1–1.4	170–484
This work, SIW,PCB	LC, Magnetic	3	21.5–22.06	6**	2.81–3.54	102–105.6
This work, SIW,LTCC	LC, Electric	3	29.4–30.1	2–4	11.2–11.6	68–100

4.2.4 *Comparison with Tunable SIW Filters from Literatures*

Several tunable SIW filter with various tuning technologies have been reported and summarized in Table 4. It can be seen that the unloaded Q-factor of the magnetically tunable LC-filled SIW filter with PCB (Chapter 3) is comparable to the other works, especially with MEMS and ferrites. However, the operating frequency of this filter is 2 to 3 times higher which makes this LC filter more promising. Compared to the other LC filter, the combination of LC and SIW technology gives an improvement of the unloaded Q-factor. While other planar topologies yield an unloaded Q-factor typically below 40, a Q-factor above 100 is possible to achieve with SIW structure.

The electrically tunable LC-filled SIW filter is also presented in Table 4. The operating frequency is even higher (around 30 GHz) than the magnetically tuned filter. An unloaded Q-factor in the range of 68–100 could still be achieved and it is still higher than for MSL-based structures in this frequency range, for example in [YMS12]. The insertion loss is also 1–2 dB lower. Although waveguide filters [FGPJ14] are expected to have a better Q-factor, its size is a drawback when a compact and low-profile device is needed.

In terms of tunability, tuning ranges of 610 MHz (3 %) and 700 MHz (2.5 %) are achieved for the magnetically and electrically tuned filter, respectively. For the LTCC filter, the results is narrower than [YMS12] due to the higher LTCC substrate permittivity. If the LC layer height (h_{LC}) could be increased, the tuning range can be improved. For example, the usage of $h_{\mathrm{LC}} = 2\,\mathrm{mm}$ and $h_{\mathrm{LC}} = 3\,\mathrm{mm}$ in an LC-based resonator can increase the tuning range into 4.5 % and 5 %, respectively, according to CST simulation results in Fig. 4.16.

[‡] Filter order or pole number

[§] Periodically Loaded Line

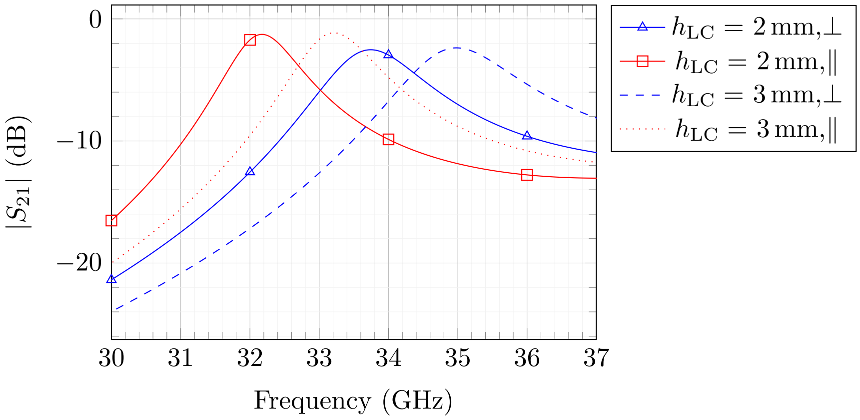

Figure 4.16.: Simulation results of an LC-based resonator (see Fig. 4.4) with a thicker LC layer, for example $h_{\mathrm{LC}} = 2\,\mathrm{mm}$ and $h_{\mathrm{LC}} = 3\,\mathrm{mm}$.

4.3 LIQUID CRYSTAL BASED AMPLITUDE TUNER

In this section, the LC-based amplitude tuner is proposed for the first time, operating at 30 GHz. A simple design is utilized for a demonstration purpose by using an interference concept with the help of a tunable LC phase shifter. Theoretically, an unattenuated signal or a the fully attenuated signal in the output can be achieved with the help of this concept, which is explained in Subsection 4.3.1. Moreover, each signal attenuation in-between can be adjusted continuously. From the general concept, the needed components are analyzed and designed as shown in Subsection 4.3.2. Before fabricating the device, the properties of the combined components are presented in Subsection 4.3.3. The fabrication and measurements are discussed in Subsection 4.3.4 for both attenuation and phase. Finally, the obtained results are compared with other devices with similar functionality in Subsection 4.3.5.

4.3.1 *Operational Principle*

To change the amplitude of a signal, the concept of interference in the signal theory can be employed. Let y_1 and y_2 be both time varying sinusoidal signals with the same frequency (f), amplitude of A_1 and A_2, as well as phase of ϕ_1 and ϕ_2:

$$\begin{aligned} y_1 &= A_1 \cos\left(2\pi f t + \phi_1\right) \\ y_2 &= A_2 \cos\left(2\pi f t + \phi_2\right). \end{aligned} \tag{4.3.1}$$

¶ Approximated by using insertion loss method [MYJ80]
‖ Parallel-coupled line
** embedded

When both of the propagating signals are incident at a certain place, interference occurs. The sum of the both signals is still a sinusoidal signal with the same frequency but different amplitude (A_{total}) and phase (ϕ_{total}):

$$y_{\text{total}} = y_1 + y_2 = A_{\text{total}} \cos\left(2\pi f t + \phi_{\text{total}}\right). \tag{4.3.2}$$

With the help of the phasor concept and trigonometric identities, the total amplitude and phase can be expressed as:

$$\begin{aligned} A_{\text{total}} &= \sqrt{{A_1}^2 + {A_2}^2 + 2A_1A_2\cos\left(\phi_{\text{diff}}\right)} \\ \phi_{\text{total}} &= \tan^{-1}\left(\frac{A_1\sin\left(\phi_1\right) + A_2\sin\left(\phi_2\right)}{A_1\cos\left(\phi_1\right) + A_2\cos\left(\phi_2\right)}\right), \end{aligned} \tag{4.3.3}$$

where $\phi_{\text{diff}} = \phi_2 - \phi_1$ is the phase difference between y_2 and y_1. By varying ϕ_{diff}, the amplitude of the total signal can be controlled. For example, A_{total} will be maximized ($A_{\text{total}} = A_1 + A_2$) when $\phi_{\text{diff}} = 0°$. On the other hand, $A_{\text{total}} = 0$ can be achieved when destructive interference occurs ($A_1 = A_2$ and $\phi_{\text{diff}} = 180°$). Therefore, continuous tuning of ϕ_{diff} between 0° and 180° yields a continuous amplitude variation between $A_1 + A_2$ and 0.

Consequently, an amplitude tuner with an input signal of $y(t) = A\cos\left(2\pi f t + \phi\right)$ can be realized by splitting the input signal into two branches: a tunable phase shifter and a fixed transmission line. The tunable phase shifter controls the phase difference ϕ_{diff} between both branches. The signals from both branches are combined again, yielding an output signal described by Eq. 4.3.2–4.3.3. An equal power divider or combiner can be employed for this purpose. In addition, DC-blocking structures are also needed to prevent the flow of the biasing current from the tunable phase shifter to the VNA. The main block diagram is shown in Fig. 4.17.

4.3.2 *Concepts and Subcomponents of the Integrated Amplitude Tuner*

The overall structure of the proposed amplitude tuner are depicted in Fig. 4.18. The main subcomponents, which are the phase shifters, power divider/combiner and DC-blocking structure, are realized in 9-layer LTCC technology. In addition to those subcomponents, the feeding circuit is also designed. The design of each subcomponent will be discussed in the following parts.

Tunable LC Phase Shifter and Fixed Line

With the tunable delay line principle (see Section 2.4), the tunable LC phase shifter can be constructed. From Eq. 2.4.2, it is clear that differential phase constant $\Delta\beta$ should be as large as possible to reduce the size of the phase shifter, i.e. the length l for a certain value of differential phase shift $\Delta\phi$. Since the relative permittivity $\varepsilon_{r,\perp}$

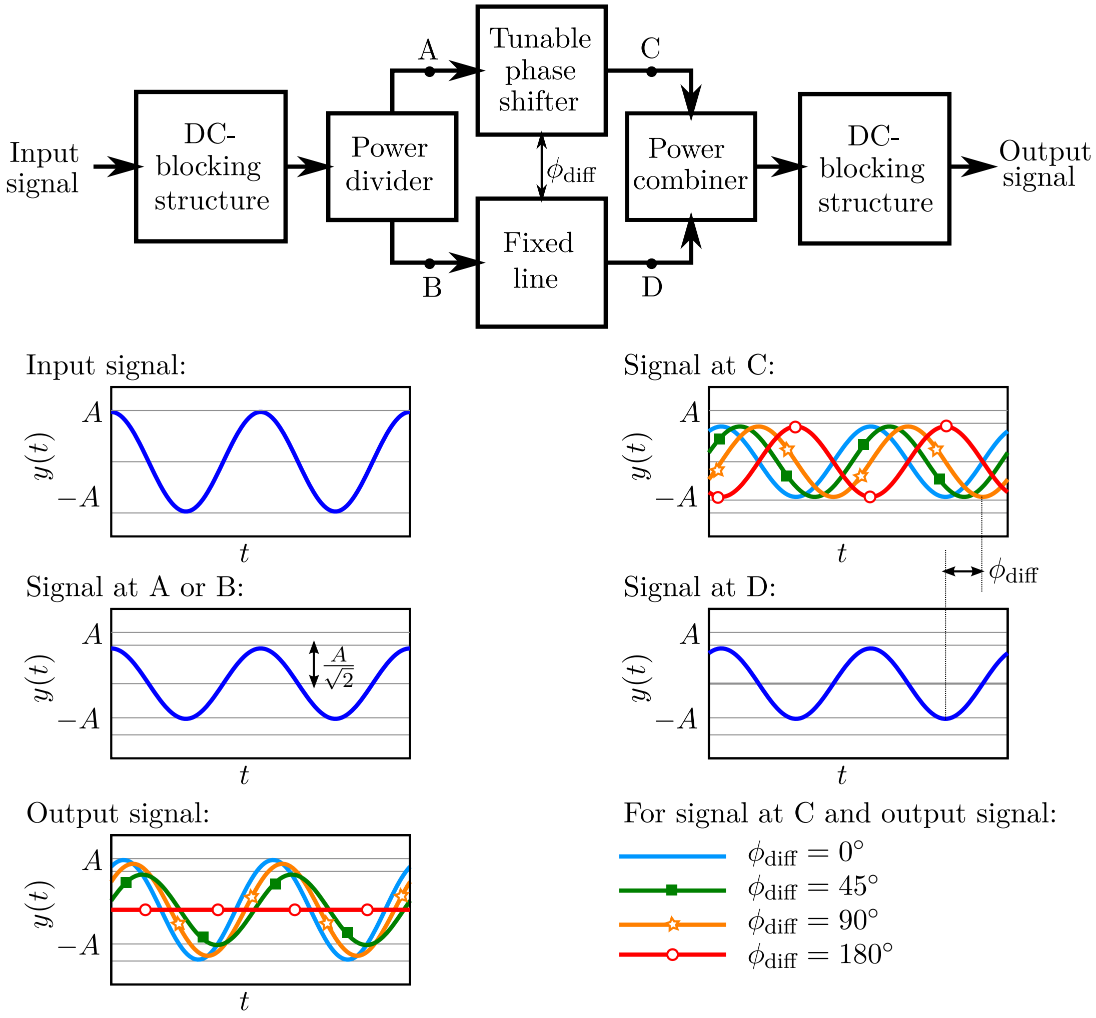

Figure 4.17.: The block diagram of the proposed amplitude tuner. Three main subcomponents are presented: tunable phase shifter/fixed line, power divider/combiner and DC-blocking structure. The phase difference ϕ_{diff} between the tunable phase shifter and the fixed line can be tuned continuously between 0° and 180° in order to achieve an output signal with an amplitude range from 0 to A. See the signal at each point for the details.

and $\varepsilon_{r,\parallel}$ of the LC are already known, the topology of the transmission line should be chosen so, that most of the electric field stays inside the LC in order to make the tuning more efficient. Compared to the well-known microstrip line (MSL) topology [WLJ02], a stripline topology provides a better tuning efficiency [JSH^{+}15]. This phase shifter has a deembedded FoM of 20 °/dB at 30 GHz, with a response time up to 37 s. The analysis of this stripline structure is carried out in Appendix B.

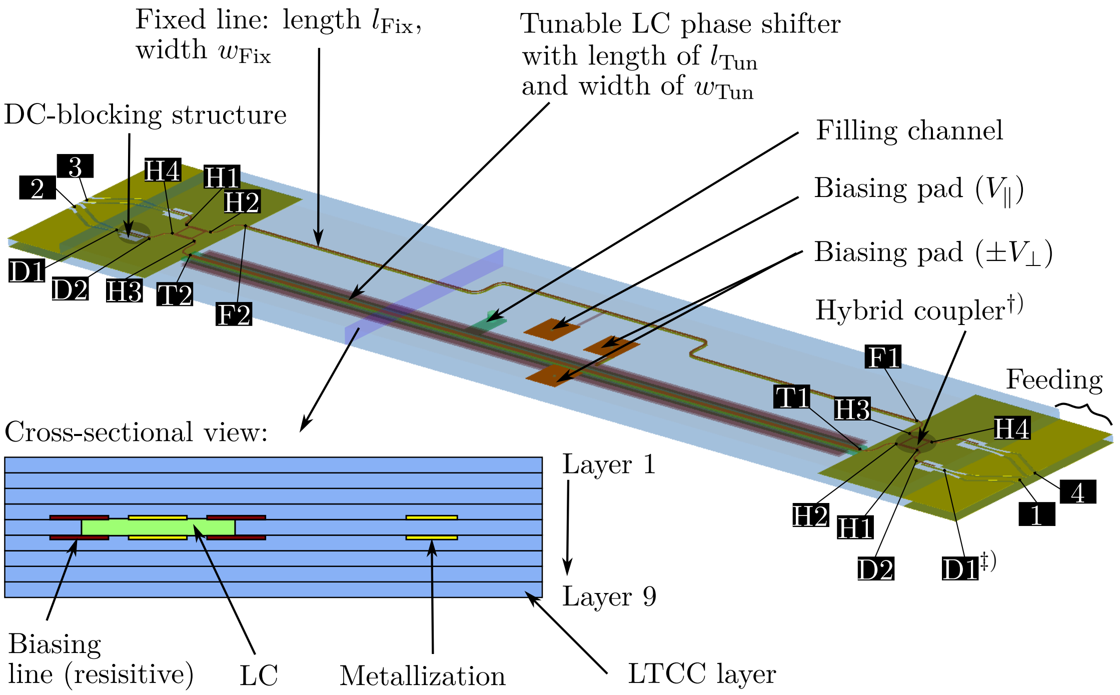

Figure 4.18.: The overall structure of the amplitude tuner: tunable LC phase shifter, fixed line, power divider/combiner (hybrid coupler) and DC-blocking structure. Nine layers of LTCC are used with a single layer thickness of $h_{\text{LTCC}} = 107\,\mu\text{m}$. The following dimensions are used for the phase shifter: $l_{\text{Tun}} = 38.3\,\text{mm}$, $l_{\text{Fix}} = 48\,\text{mm}$, $w_{\text{Tun}} = 260\,\mu\text{m}$ and $w_{\text{Fix}} = 150\,\mu\text{m}$. See Fig. and Fig. 4.24 for the details of the hybrid coupler and DC-blocking structure, respectively. Note: $^{\dagger)}$the hybrid couplers are used for power divider and combiner, $^{\ddagger)}$ **D1** means port D1.

Both extreme states of the stripline topology are simulated using a simulation tool developed at the Institute of Microwave Engineering and Photonics, TU Darmstadt [GGMJ08] and shown in Fig. 4.19. For perpendicular state, two pairs of biasing lines made of resistive paste 2061 with a resistivity of $200\,\text{k}\Omega/\square$ are employed with voltages of $\pm V_{\perp}$ on the left and right side. A voltage of $V_{\parallel}$ is applied in the top electrode of the stripline phase shifter for the parallel orientation, while the bottom electrode and the resistive lines are set to a voltage of 0 V.

The striplines are designed for an impedance of $50\,\Omega$ with line widths of $260\,\mu\text{m}$ for the tunable branch and $150\,\mu\text{m}$ for the fixed branch. With the determined dimension, the obtained phase constants for perpendicular and parallel case of the tunable phase shifter are 1157 rad/m and 1239 rad/m or equivalent to effective relative permittivity in the range of 3.39–3.88 . This range is around 7 % better than the tunable phase shifter using MSL technology. For amplitude tuner application with 180° phase shift, the length

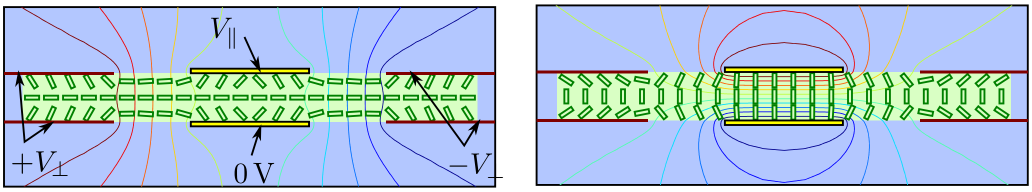

(a) (b)

Note:
▭ Metallization
▬ Resisitive line
▯ LC director
🟦 LTCC substrate

Figure 4.19.: (a) Perpendicular and (b) parallel state of the LC inside the stripline phase shifter. The orientation of the LC can be changed, for example by setting the biasing voltage as followings: (a) $V_\parallel = 0\,\text{V}$ and $V_\perp = 100\,\text{V}$ for perpendicular case, (b) $V_\parallel = 80\,\text{V}$ and $V_\perp = 0\,\text{V}$ for parallel case.

of the tunable stripline should be at least 38.3 mm according to Eq. 2.4.2. For the fixed branch, the length of the phase shifter is designed so that the phase is equal to the phase in the tunable branch when the LC is oriented perpendicularly. A length of 48 mm is suitable for this design.

As shown in Fig. 4.18, the stripline structures are designed at the layer 4 and 5. The LC filling channel is also designed, which has dimensions of 1.7 mm×1 mm×0.107 mm. This channel is connected to the 0.5 mm filling hole. The biasing pads are also included in the design, which connect the biasing lines with the voltage source. Note that since the direct connection to the tunable phase shifter is impossible, the connection is made through the fixed lines for the $V_\parallel$ biasing pad. The fixed and tunable branches are connected at the power divider/combiner subcomponent so that both branches have the same potential. The CST simulation results of both phase shifters are shown in Fig. 4.20. A differential phase shift of 180° is achieved with insertion loss less than 5.6 dB.

Power Divider and Combiner

A power divider is needed to separate a signal into the tunable and non-tunable branch, and vice versa for the power combiner. A popular topology for this purpose is the Wilkinson power divider [Poz11], which also could be used as power combiner. The structure is depicted in Fig. 4.21a.

The signal from port P1 is split into two quarter wavelength ($\lambda/4$) branches. According to [Poz11], if the line impedance at each port is Z_0, both branches should have an impedance of $\sqrt{2}Z_0$. To provide a perfect matching at the operating frequency, a resistor with a value of $2Z_0$ should be attached between port 2 and 3. Using a microstrip line topology, the following dimensions are obtained: line width $w_\text{line} = 100\,\mu\text{m}$ and branch width $w_\text{branch} = 20\,\mu\text{m}$ for Z_0 of $50\,\Omega$. However, this design is not suitable since it is difficult to fabricate (dimensions should be equal or larger than 100 µm).

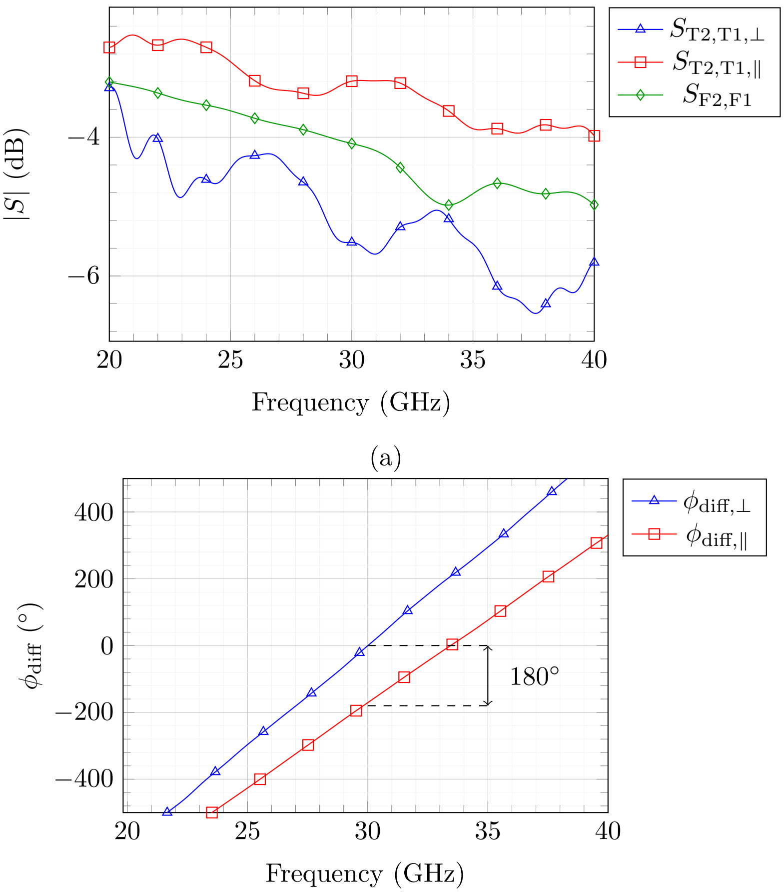

(a)

(b)

Figure 4.20.: Simulation results of the tunable phase shifter and fixed line: (a) transmission coefficient $|S|$ and (b) phase difference (ϕ_{diff}) between tunable and fixed branch. See Fig. 4.18 for the port definition.

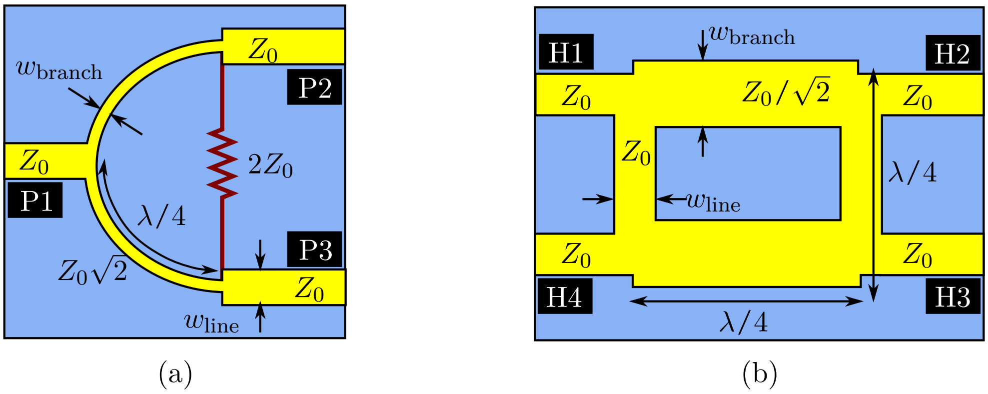

(a) (b)

Figure 4.21.: Two possibilities for the power divider part: (a) Wilkinson power divider and (b) hybrid coupler. Since the Wilkinson power divider is not suitable for fabrication, the hybrid coupler is chosen with following dimensions: $w_{\text{line}} = 100\,\mu\text{m}$ and $w_{\text{branch}} = 200\,\mu\text{m}$.

Another alternative to realize a power divider or combiner is the hybrid coupler [Poz11], which is shown in Fig. 4.21b. Since the hybrid coupler has 4 inputs and only 3 of them are needed, one input should be terminated by a matched load. The VNA can be employed to provide the match termination. At the operating frequency, the line impedances of the hybrid coupler should be $Z_0/\sqrt{2}$ and Z_0 (see Fig. 4.21b) [Poz11], resulting in following dimensions: $w_{\text{line}} = 100\,\mu\text{m}$ and $w_{\text{branch}} = 200\,\mu\text{m}$.

The simulation results are shown in Fig. 4.22. Assuming the signal comes from port H1, it will be divided equally into port H2 and H3. This is indicated by the equal insertion loss of 3.6 dB around 30 GHz. For a lossless coupler, the ideal loss is 3 dB, which indicates the half power of the input signal. Therefore, there is an additional loss of 0.6 dB at the circuit. The magnitude of $S_{\text{H1,H1}}$ and $S_{\text{H4,H1}}$ are below -20 dB around 30 GHz, indicating a low input reflection and a good isolation.

The usage of the hybrid coupler as a power divider gives an additional phase difference of 90° between the path H1-H2 and H1-H3 due to unequal path length. By using port 1 as the input and port 3 as the output of the whole amplitude tuner (see Fig. 4.18), the additional phase difference from the power divider and combiner cancel out each other, since a $-90°$ phase shift difference is introduced at the power combiner.

DC-blocking Structure

A DC-blocking structure is included in the design and placed between the hybrid coupler and the CPW contact pad. Since the probe is only suitable for a CPW structure, it is used as the topology for the feeding lines. Therefore, this DC blocking structure should also serve as a transition between the CPW and microstrip line. A solution can be found in [ZM04], which uses a gap enabling electromagnetic coupling between both

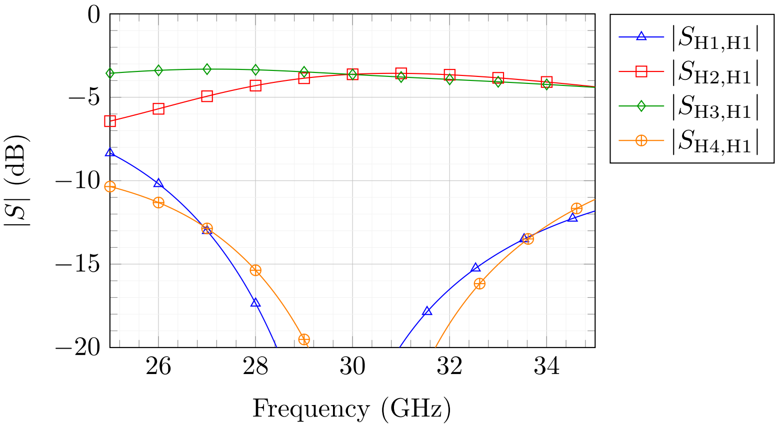

Figure 4.22.: Simulation results of the hybrid coupler. See Fig. 4.18 or Fig. 4.21b for the port definition.

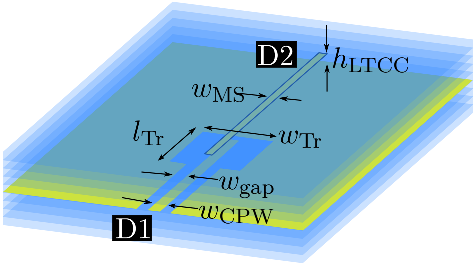

Figure 4.23.: The DC-blocking structure. The following dimensions are used: $w_{\mathrm{CPW}} = 150\,\mu\mathrm{m}$, $w_{\mathrm{gap}} = 150\,\mu\mathrm{m}$, $l_{\mathrm{Tr}} = 1.21\,\mathrm{mm}$, $w_{\mathrm{Tr}} = 0.96\,\mathrm{mm}$ and $w_{\mathrm{MS}} = 100\,\mu\mathrm{m}$.

transmission line topology. In this case, the gap is made by a 107 µm LTCC layer, which is able to block the biasing current. The detailed structure can be found in Fig. 4.18 and the simulation results are shown in Fig. 4.24. At 30 GHz, the reflection is lower than −20 dB with 1 dB insertion loss, being acceptable for the amplitude tuner.

Feeding Circuit

Since the VNA will provide the matched termination, two additional ports are needed so that the amplitude tuner will have 4 ports (2 input ports and 2 output ports). One possibility to feed the input and output signals is using 2 ports GSGSG probes (G=Ground, S=Signal) from Cascade (see Fig. 4.25), which have a pitch of 500 µm. Two GCPW lines with a width and a gap of 400 µm and 200 µm, respectively, are used as contact pads for the probes. Between the GCPW and the DC blocking structure, a quarter-wavelength tapered transition is used for a lower reflection. Both the feeding structure and simula-

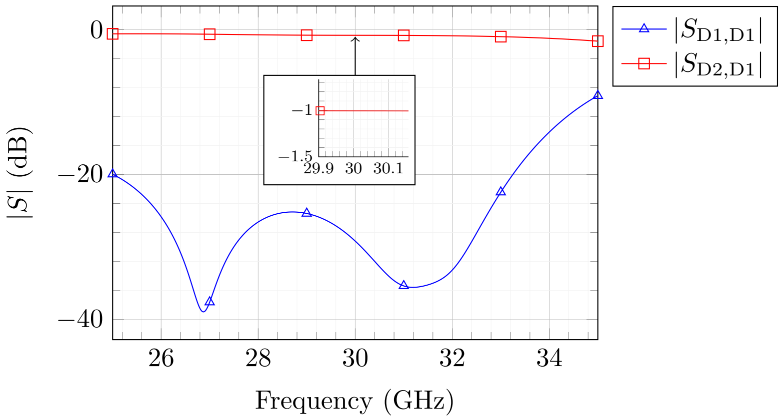

Figure 4.24.: Simulation results of the DC-blocking structure. See Fig. 4.23 or Fig. 4.18 for the port definition.

tion results are presented in Fig. 4.26. The simulation gives a return loss of 20 dB with 0.9 dB of insertion loss.

4.3.3 *Amplitude Tuner Response*

The theoretical response of the amplitude tuner will be discussed first and then compared with the simulation results from CST Microwave Studio. In order to calculate the theoretical S-parameters of the amplitude tuner, the S-parameters of each components is needed to be known. Due to the cascade configuration of the components, a T-parameter concept for a 4-port device is developed first in Appendix C, which can be easily obtained from the S-parameters. Hence, the T-parameter of the amplitude tuner (T_{AS}), which is a cascade arrangement of power divider with T-parameter of T_{PD}, phase shifters with T-parameter of T_{PS} and power combiner with T-parameter of T_{PC} is:

$$\left[T_{\mathrm{AS}}\right] = \left[T_{\mathrm{PD}}\right]\left[T_{\mathrm{PS}}\right]\left[T_{\mathrm{PC}}\right]. \tag{4.3.4}$$

Note that the port definition of the amplitude tuner and its subcomponents are described in Fig. 4.18.

Figure 4.25.: GSGSG Probe connected to two GCPW transmission lines.

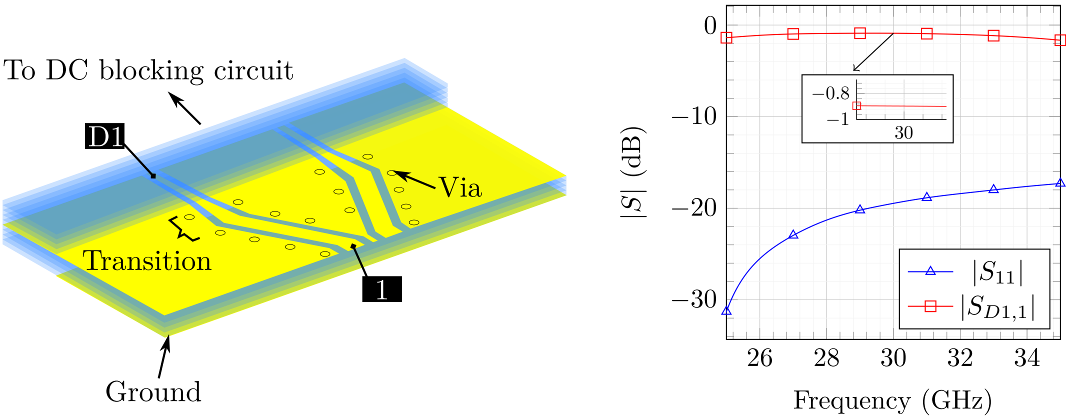

(a)

(b)

Figure 4.26.: (a) Simulation model of the feeding line. (b) The corresponding simulation results from a single GCPW line (port 1) to a single CPW line embedded inside the LTCC (port 2).

As already mentioned in Subsection 4.3.2, hybrid coupler structures are used as the power divider and combiner. The S-parameter matrix of an ideal hybrid coupler is [Poz11]:

$$\begin{aligned} \begin{bmatrix} b_{\mathrm{H1}} \\ b_{\mathrm{H2}} \\ b_{\mathrm{H3}} \\ b_{\mathrm{H4}} \end{bmatrix} &= \begin{bmatrix} S_{\mathrm{HC}} \end{bmatrix} \begin{bmatrix} a_{\mathrm{H1}} \\ a_{\mathrm{H2}} \\ a_{\mathrm{H3}} \\ a_{\mathrm{H4}} \end{bmatrix} \\ \begin{bmatrix} S_{\mathrm{HC}} \end{bmatrix} &= \frac{-1}{\sqrt{2}} \begin{bmatrix} 0 & j & 1 & 0 \\ j & 0 & 0 & 1 \\ 1 & 0 & 0 & j \\ 0 & 1 & j & 0 \end{bmatrix}. \end{aligned} \tag{4.3.5}$$

From Eq. 4.3.5, the arrangement of variable incident waves a and reflected waves b can be adjusted to the Eq. C.0.30 in order to find the T-parameter. The result is:

$$\begin{bmatrix} T_{\mathrm{HC}} \end{bmatrix} = \begin{bmatrix} T_{\mathrm{PD}} \end{bmatrix} = \begin{bmatrix} T_{\mathrm{PC}} \end{bmatrix} = \frac{1}{\sqrt{2}} \begin{bmatrix} j & 0 & 1 & 0 \\ 0 & -j & 0 & -1 \\ 1 & 0 & j & 0 \\ 0 & -1 & 0 & -j \end{bmatrix}. \tag{4.3.6}$$

Now, the T-parameter for the phase shifters should be determined. The relations between the reflected and incident waves are given by:

$$\begin{aligned} \begin{bmatrix} b_{\mathrm{T1}} \\ b_{\mathrm{T2}} \\ b_{\mathrm{F2}} \\ b_{\mathrm{F1}} \end{bmatrix} &= \begin{bmatrix} S_{\mathrm{PS}} \end{bmatrix} \begin{bmatrix} a_{\mathrm{T1}} \\ a_{\mathrm{T2}} \\ a_{\mathrm{F2}} \\ a_{\mathrm{F1}} \end{bmatrix}, \\ \begin{bmatrix} S_{\mathrm{PS}} \end{bmatrix} &= \begin{bmatrix} 0 & e^{-\gamma_1 l_1} & 0 & 0 \\ e^{-\gamma_1 l_1} & 0 & 0 & 0 \\ 0 & 0 & 0 & e^{-\gamma_2 l_2} \\ 0 & 0 & e^{-\gamma_2 l_2} & 0 \end{bmatrix}, \end{aligned} \tag{4.3.7}$$

where $\gamma_i = \alpha_i + j\beta_i$ is the propagation constant inside the tunable phase shifter ($i = 1$) and fixed line ($i = 2$). l_i denotes the physical length of the corresponding transmission line.

Thus, the T-parameter is:

$$\begin{bmatrix} T_{\mathrm{PS}} \end{bmatrix} = \begin{bmatrix} e^{\gamma_1 l_1} & 0 & 0 & 0 \\ 0 & e^{-\gamma_1 l_1} & 0 & 0 \\ 0 & 0 & e^{\gamma_2 l_2} & 0 \\ 0 & 0 & 0 & e^{-\gamma_2 l_2} \end{bmatrix}. \tag{4.3.8}$$

Inserting Eq. 4.3.6 and Eq. 4.3.8 to Eq. 4.3.4, the obtained T-parameter for the amplitude tuner is:

$$[T_{\mathrm{AT}}] = \frac{1}{2}\begin{bmatrix} -e^{\gamma_1 l_1}+e^{\gamma_2 l_2} & 0 & j\left(e^{\gamma_1 l_1}+e^{\gamma_2 l_2}\right) & 0 \\ 0 & -e^{-\gamma_1 l_1}+e^{-\gamma_2 l_2} & 0 & j\left(e^{-\gamma_1 l_1}+e^{-\gamma_2 l_2}\right) \\ j\left(e^{\gamma_1 l_1}+e^{\gamma_2 l_2}\right) & 0 & e^{\gamma_1 l_1}-e^{\gamma_2 l_2} & 0 \\ 0 & j\left(e^{-\gamma_1 l_1}+e^{-\gamma_2 l_2}\right) & 0 & e^{-\gamma_1 l_1}-e^{-\gamma_2 l_2} \end{bmatrix}. \tag{4.3.9}$$

From its T-parameters, the S-parameters for the amplitude tuner could be obtained by rearranging Eq. C.0.30 in the form of Eq. C.0.28. The most interesting part to be observed is the transmission coefficients, which is $S_{31,\mathrm{AT}}$ according to Subsection 4.3.2:

$$S_{31,\mathrm{AT}} = \frac{1}{2}\sqrt{e^{-2\alpha_1 l_1}+e^{-2\alpha_2 l_2}+2e^{-(\alpha_1 l_1+\alpha_2 l_2)}\cos\left(\beta_1 l_1-\beta_2 l_2\right)}. \tag{4.3.10}$$

This transmission coefficient is related to the attenuation of the amplitude tuner.

For a better understanding of the response, the ideal case, which assumes that all of the phase shifters are lossless, is discussed first. Substituting $\alpha = 0$ for a lossless case, the Eq. 4.3.10 can be reduced into:

$$S_{31,\mathrm{AT}} = \sqrt{0.5\left(1+\cos\left(\beta_1 l_1-\beta_2 l_2\right)\right)}. \tag{4.3.11}$$

With the phase constant $\beta_i = 2\pi f\sqrt{\varepsilon_{r,i}}/c$, f is the frequency, c is the speed of electromagnetic waves in vacuum and $\varepsilon_{r,i}$ is the effective relative permittivity of each phase shifter, Eq. 4.3.11 can be modified as:

$$S_{31,\mathrm{AT}}(f) = \sqrt{0.5\left(1+\cos\left(2\pi\left(\frac{l_1\sqrt{\varepsilon_{r,1}}-l_2\sqrt{\varepsilon_{r,2}}}{c}\right)f\right)\right)}. \tag{4.3.12}$$

By substituting the values of the physical lengths and relative permittivities (see Subsection 4.3.2), the plot of the transmission coefficient $S_{31,\mathrm{AT}}$ as a function of frequency can be generated, which is shown in Fig. 4.27. Periodic properties appear in Fig. 4.27 which represents the periodic nature of the tunable delay line utilized in the phase shifter component. The transmission zeros appear at several frequencies, where the signal from both phase shifter cancel each other. Meanwhile, the signals add each other at the other frequencies, resulting in multiple maxima or peaks in the frequency response of the amplitude tuner. Increasing the LC permittivity inside the phase shifter by tuning yields a displacement of the transmission zeros and peaks location, which are moving towards the higher frequency due to the lower phase difference between both phase shifters.

The displacement of the frequency response is utilized to shift the amplitude or attenuate the signal by a certain value controlled by the LC tuning. This feature will be clear

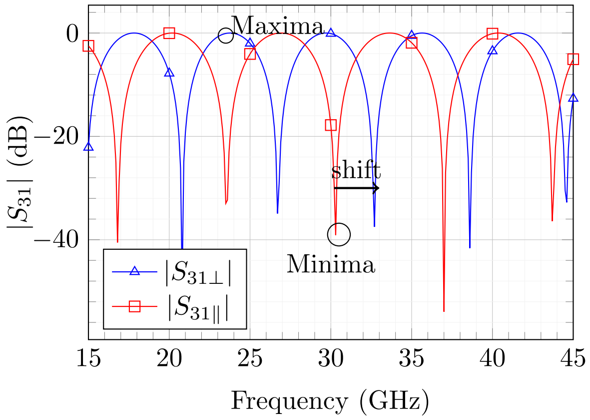

Figure 4.27.: Calculated response of an amplitude tuner.

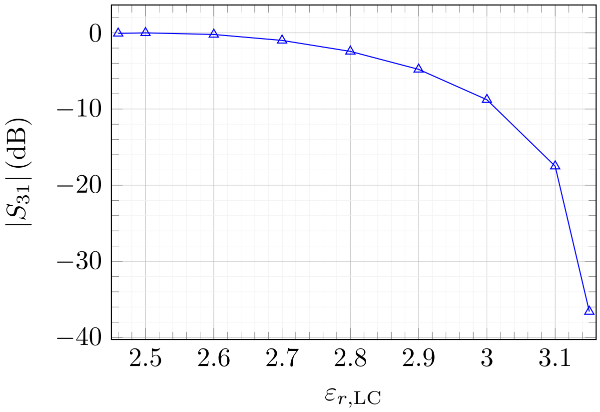

Figure 4.28.: The relation between the relative permittivity of LC $\varepsilon_{r,\mathrm{LC}}$ and $|S_{31}|$ at 30 GHz.

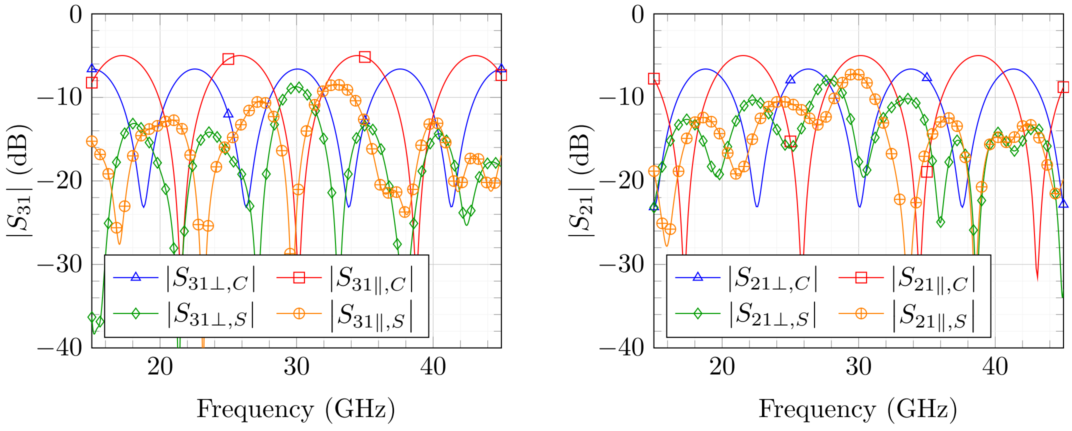

(a) $|S_{31}|$ (b) $|S_{21}|$

Figure 4.29.: Theoretical response of an amplitude tuner. Note: ⊥ = perpendicular, ∥ = parallel, C = calculation using Eq. 4.3.10 or Eq. 4.3.13, S = simulation using CST Microwave Studio.

if the relation between the magnitude of the $S_{31,\mathrm{AT}}$ and the relative permittivity of LC $\varepsilon_{r,\mathrm{LC}}$ is plotted at the frequency of 30 GHz, as shown in Fig. 4.28. It is visible that this device can continuously alter the amplitude of the input signal with attenuation from 0 dB to more than 40 dB, theoretically. The drawback of this device is the frequency dependency of the magnitude of the $S_{31,\mathrm{AT}}$. However, the amplitude tuner is still suitable for narrowband applications.

To find the real limitation of the amplitude tuner, the losses should be calculated. By substituting the value of α and β for both LC and LTCC material to Eq. 4.3.10, the curve of S_{31} can be plotted in Fig. 4.29a. The results show an insertion loss of 6.6 dB at the peak. The loss and frequency dependency from the other subcomponents have not been taken into account in Eq. 4.3.10. To inspect the overall component, simulations using CST Microwave Studio are conducted using the structure depicted in Fig. 4.18 and the results are also depicted in Fig. 4.29a. At around 30 GHz, the simulation results show a good agreement with the calculated results. The possible attenuation achieved by this device is 9.5 dB to more than 20 dB, where its minimum attenuation is around 3 dB higher than the calculation result.

The high insertion loss is caused by the lossy materials, such as LC and the gold paste, which is utilized to construct the amplitude tuner. The contribution of each material can be analyzed with additional CST simulations. Fig. 4.30 shows that the usage of perfect electric conductor (PEC) with lossy LC can improve the minimum insertion loss into 2 dB. On the other hand, a higher insertion loss is unavoidable (minimum attenuation of 8 dB) when the gold paste is used with lossless LC (LLC). Therefore, the metallization is the main cause of the high insertion loss.

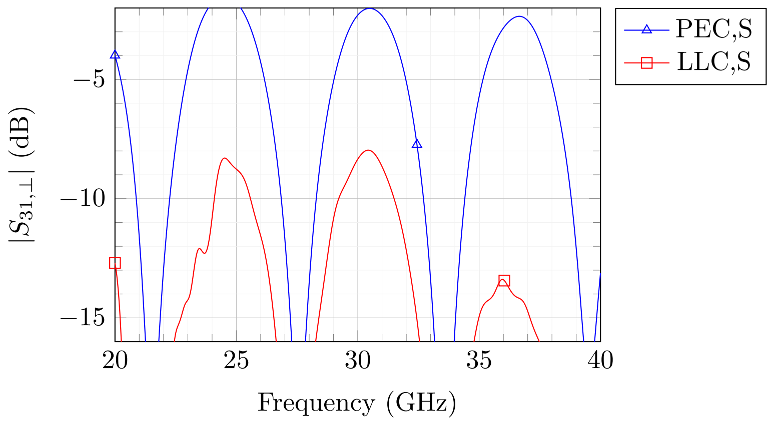

Figure 4.30.: Additional simulations using perfect electric conductor (PEC) and lossless LC (LLC). The insertion loss is mainly caused by the metallization, which adds an unwanted insertion loss of 8 dB.

With the same way as the S_{31}, the S_{21} can be calculated from the T-parameter, so that the following expression is obtained:

$$S_{21,\mathrm{AT}} = \frac{1}{2}\sqrt{e^{-2\alpha_1 l_1} + e^{-2\alpha_2 l_2} - 2e^{-(\alpha_1 l_1 + \alpha_2 l_2)} \cos\left(\beta_1 l_1 - \beta_2 l_2\right)}. \tag{4.3.13}$$

The plot of this equation is depicted in Fig. 4.29b. The CST simulation is also performed as a comparison and gives an attenuation range of around 8 dB to more than 20 dB. Note that the S_{21} is the reverse of the S_{31} due to the energy conservation.

With the CST simulation, the reflection at each port can be investigated, as well as the isolation between adjacent ports, which is shown in Fig. 4.31. For both extreme states, the return loss at the operating frequency is around 15 dB. The isolations are also 15 dB indicating a small leakage from an input port to its neighboring port.

4.3.4 *Hardware Implementation and Measurement Results*

The designed amplitude tuner is fabricated by BAM. The fabricated device is depicted in Fig. 4.32. Three biasing pads can be seen in Fig. 4.32 which will be connected with the voltage source during the measurement for biasing.

Fig. 4.33 shows the measurement setup used for the amplitude tuner. The device is placed in a fixture and connected to the VNA through the GSGSG probe. All of the biasing pads in Fig. 4.32 are connected to the voltage sources.

Before measuring the LC-filled device, an investigation of the empty structure is conducted first to check the conformity of the fabricated structure. The measurement is compared with a simulation, as shown in Fig. 4.34.

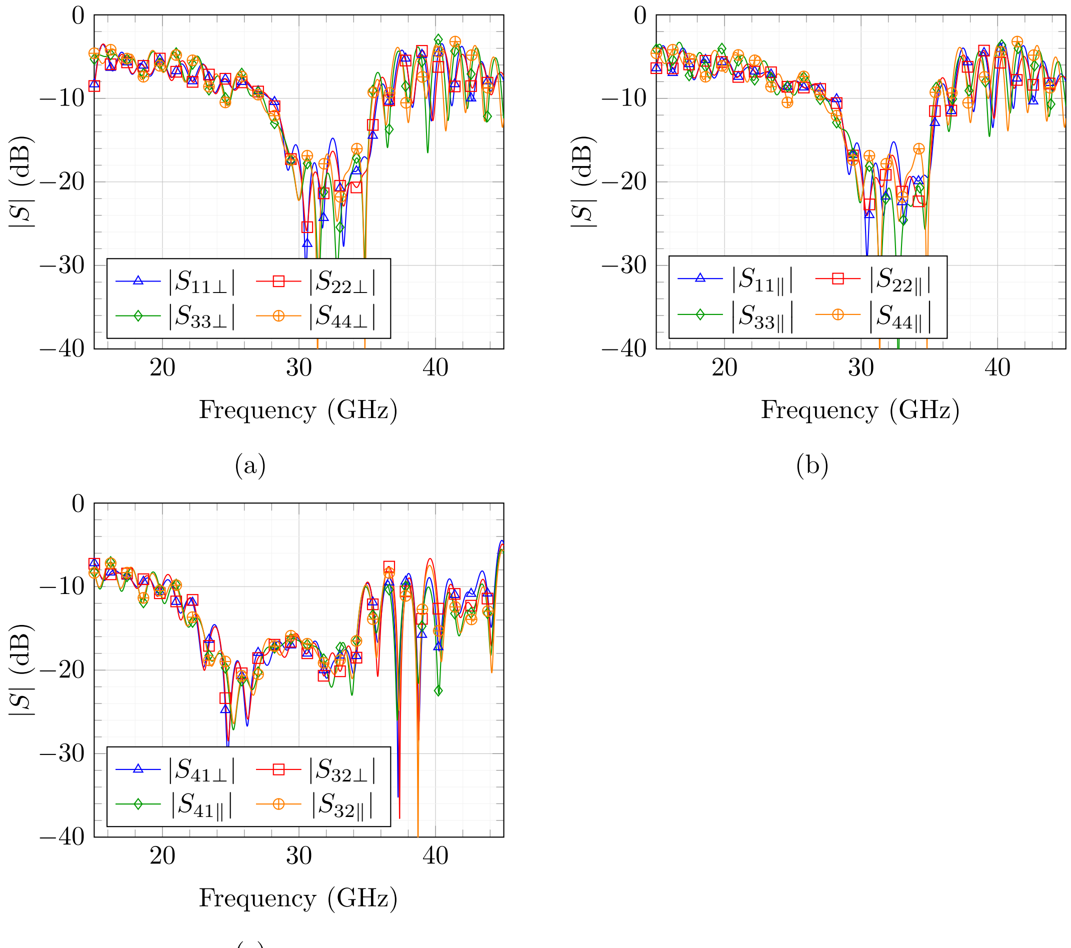

(a)

(b)

(c)

Figure 4.31.: Reflection for (a) perpendicular and (b) parallel case, and also isolation (c) of the amplitude tuner, simulated with CST Microwave Studio.

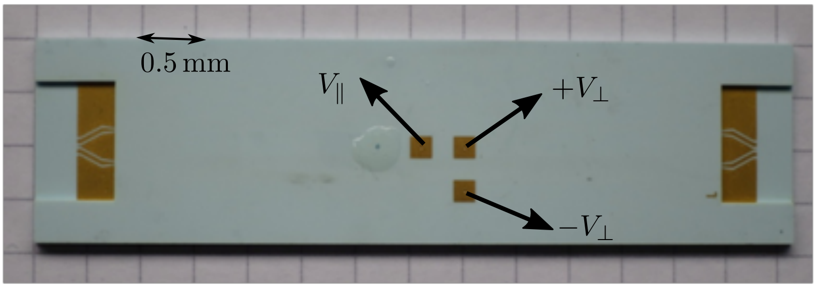

Figure 4.32.: Fabricated amplitude tuner with biasing pads for perpendicular ($V_\perp$) and parallel ($V_\parallel$) biasing.

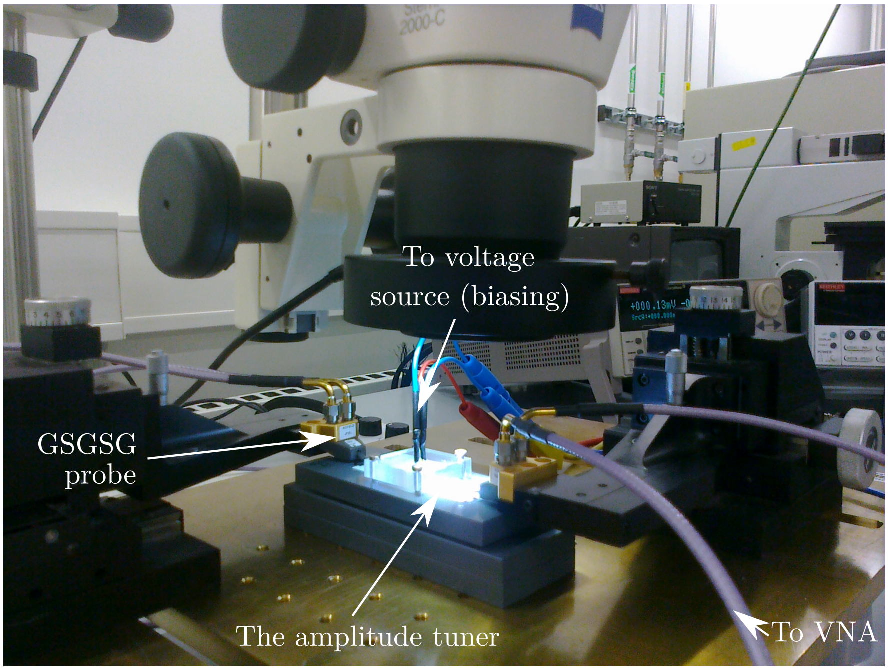

Figure 4.33.: Measurement setup for the amplitude tuner. The blue biasing cables are for $V_\perp$ and the red one is for $V_\parallel$.

The simulation and measurement results depicted in Fig. 4.34 show similarity for the reflection measurement (S_{11}). The S_{21} also shows a similarity up to 30 GHz. For S_{31} and S_{41}, the results are quite different for the frequency range around 25–35 GHz. This is possibly due to the imperfect GSGSG probe contact, which cause the signal flows to port 4 instead of port 3. Therefore, the peak of S_{31} around 30 GHz (Fig. 4.34c) is lower compared to the simulation.

After performing the empty measurement, the amplitude tuner is filled with LC in the vacuum chamber so that the LC-filled device can be measured. The measurement result is presented in Fig. 4.35. Good results are obtained in the measurement results of S_{31} (Fig. 4.35c). When biasing voltages of ±100 V are applied on the left and right side of the tunable phase shifter, the attenuation from S_{31} is minimum, 11 dB at 30 GHz. These perpendicular voltages are tuned to 0 V while the parallel voltage is applied on the top metallization of phase shifter, creating an external electric field parallel to the RF field. The LC director will align in the parallel direction and the maximum obtained attenuation is 30 dB for a parallel voltage of 80 V. Therefore, the amplitude tuner gives a continuous amplitude tuning range of 19 dB. Please note that the DC ground should be connected to the RF ground to obtain the correct measurement results.

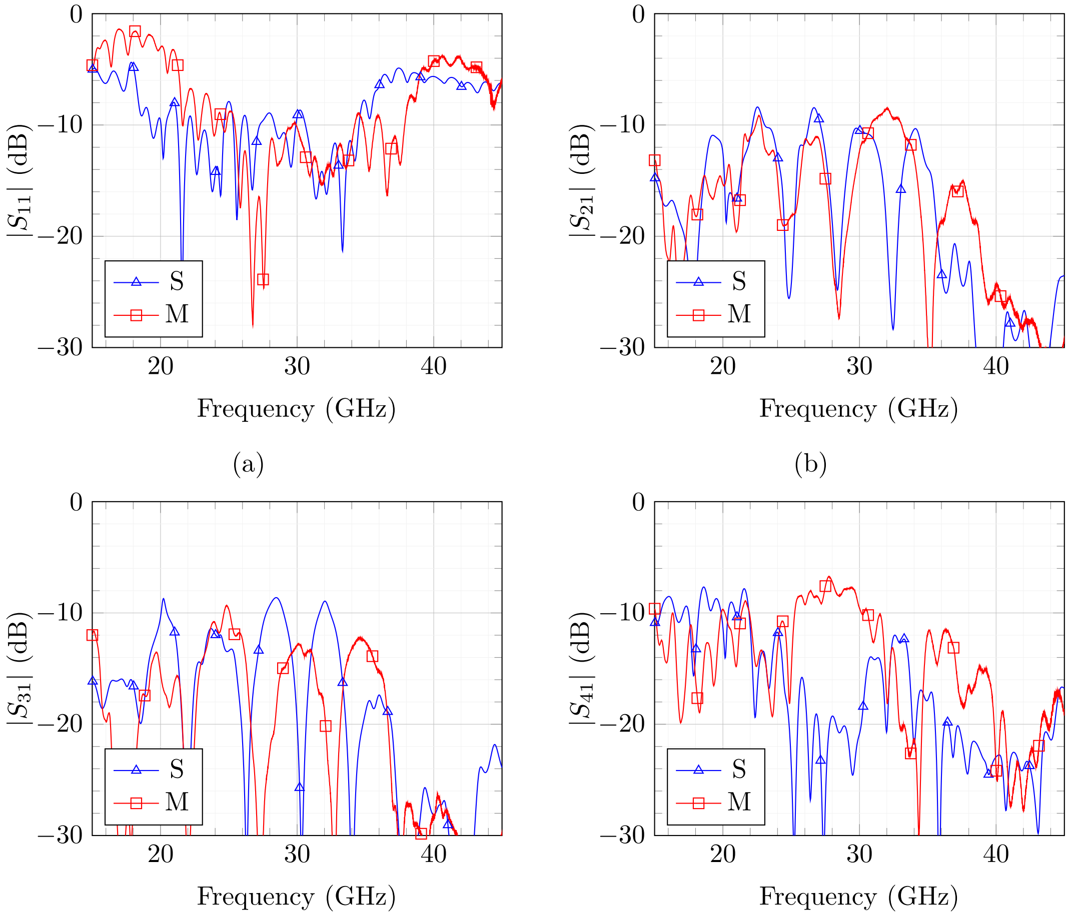

(a) (b)

(c) (d)

Figure 4.34.: S-parameter measurement results for the fabricated amplitude tuner without LC (empty): (a) S_{11}, (b) S_{21}, (c) S_{31} and (d) S_{41}. Note: S = Simulation, M = Measurement.

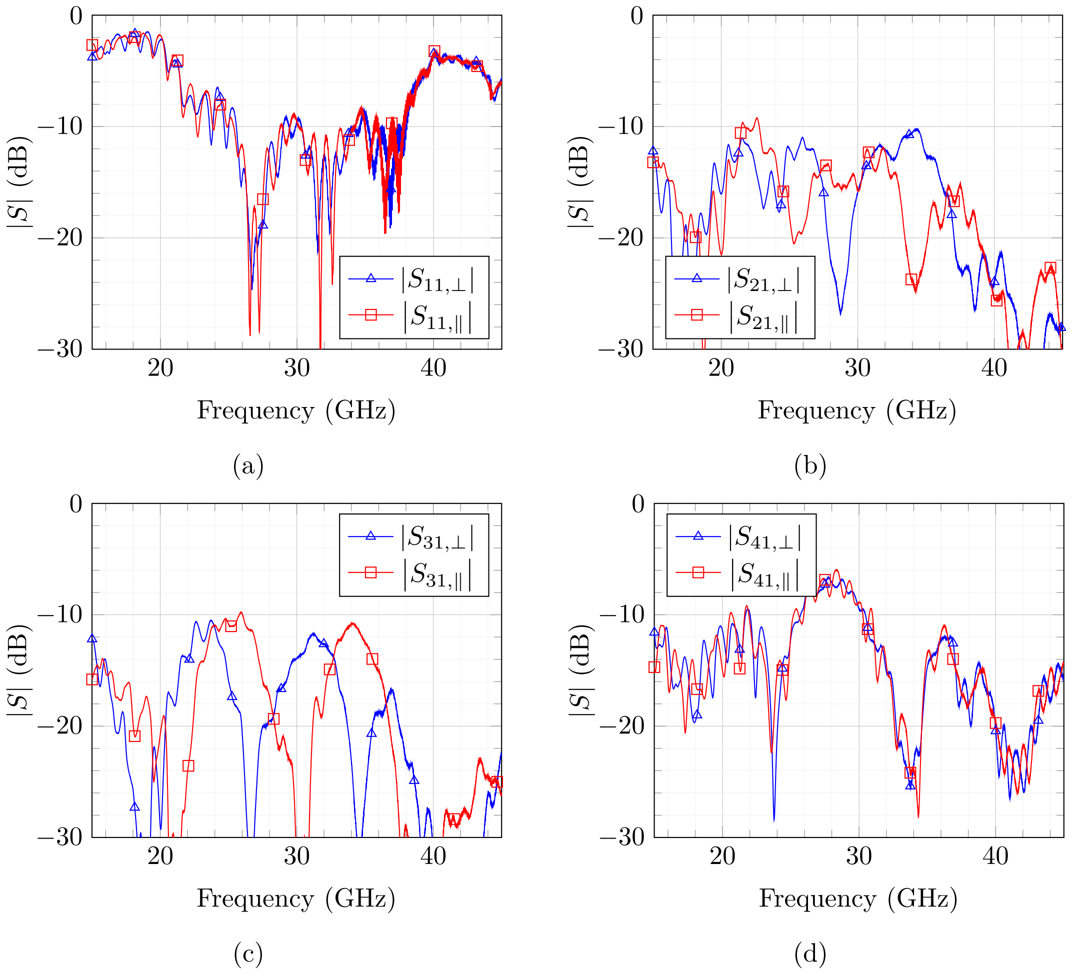

(a) (b)

(c) (d)

Figure 4.35.: S-parameter measurement results for the LC-filled amplitude tuner: (a) S_{11}, (b) S_{21}, (c) S_{31} and (d) S_{41}. Note: $\perp$ = perpendicular state, $\parallel$ = parallel state.

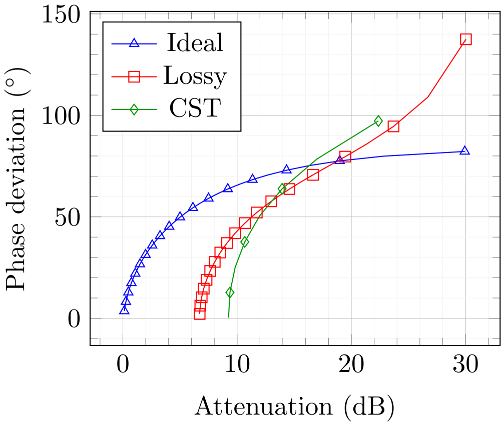

Figure 4.36.: Relation between attenuation S_{31} and phase deviation of the phase shifter inside the amplitude tuner.

Phase of the Amplitude Tuner

An ideal amplitude tuner or variable attenuator, for an application such as antenna array in radar system [Par72] or gain control [Stu06], should have a minimum phase variation. For our amplitude tuner, this means the variation of the phase term $\angle S_{31}$ should be as small as possible. The values of $\angle S_{31}$ can be obtained using the circuit analysis explained in Subsection 4.3.3.

The phase can be formulated from its S-parameter derived from the T-parameter in Eq. 4.3.9:

$$\angle S_{31} = \tan^{-1}\left(\frac{e^{-\alpha_1 l_1}\cos\left(\beta_1 l_1\right) + e^{-\alpha_2 l_2}\cos\left(\beta_2 l_2\right)}{e^{-\alpha_1 l_1}\sin\left(\beta_1 l_1\right) + e^{-\alpha_2 l_2}\sin\left(\beta_2 l_2\right)}\right). \tag{4.3.14}$$

For lossless phase shifters, Eq. 4.3.14 can be reduced by the help from trigonometric identities into:

$$\angle S_{31} = \frac{\pi}{2} - \frac{\beta_1 l_1 + \beta_2 l_2}{2} + n_{31}\pi. \tag{4.3.15}$$

where n_{31} is an integer, which is appeared due to the inverse tangent function.

The phase shift variation caused by the amplitude tuner (relative to the perpendicular state), is plotted in Fig. 4.36 for both ideal and lossy case. The CST simulation results are also plotted as well. The CST result is different from the calculated result but more accurate, since all of the transitions are taken into account, as well as the real properties of the hybrid coupler. Nevertheless, the tendency of the curves are the same.

From Fig. 4.36, it is revealed that the phase shift is different for each state of attenuation, which is related to the tunable permittivity of LC. To overcome this unwanted phase shift, an additional phase shifter can be placed after the output of the amplitude tuner. In antenna arrays for example, this phase shifter could be merged into the tunable phase shifter which controls the beam direction. The required additional differential

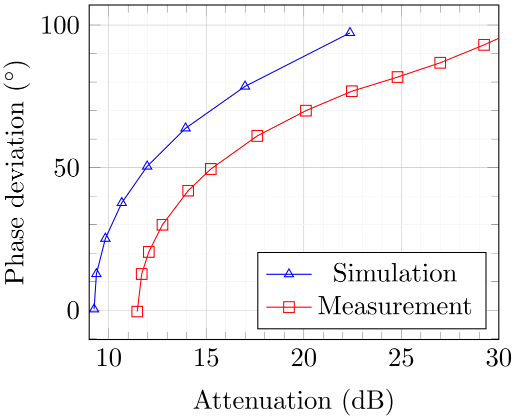

Figure 4.37.: Relation between the attenuation and phase shift of the amplitude tuner.

phase shift of this phase shifter due to the amplitude tuner is related to the maximum phase deviation caused by the amplitude tuner. According to Eq. 4.3.15, the maximum phase deviation for the lossless case is:

$$\Delta\left(\angle S_{31}\right) = \left|\angle S_{31,\parallel} - \angle S_{31,\perp}\right| = \frac{\beta_{1,\parallel} l_1 - \beta_{1,\perp} l_1}{2} = 90^\circ \tag{4.3.16}$$

The value 90° comes from the designed differential phase shift of the LC phase shifter (which is 180°, see Subsection 4.3.2). When the loss is taken into account, the maximum phase shift difference deviates up to 180° from the lossless case, as shown in Fig. 4.36. However, we can limit the attenuation value to get the lower phase difference.

The measurement results are plotted in Fig. 4.37, which shows a maximum phase deviation of 94° from the perpendicular state. This result shows an agreement with the CST simulation result, which give a maximum deviation of 96°.

4.3.5 *Comparison of Amplitude Tuner*

In this section, the proposed amplitude tuner is compared with other similar devices, which feature amplitude tuning properties. The comparison is summarized in Table 5.

As can be seen from Table 5, various technologies are utilized to realize amplitude tuners. Most of them are using semiconductor solutions to tune the amplitude, which work at frequencies lower than 12 GHz. The insertion loss in this work is 11 dB. This insertion loss is mostly caused by the metallization (see Subection 4.3.3). However, the operating frequency of this amplitude tuner is 30 GHz which is above the other variable attenuators. In addition, the proposed component is completely space qualified, giving a major advantage compared to the existing technologies.

Some improvements can be made in the future, for example miniaturization of the device. The device along with the tuning system is still smaller than the mechanically

Table 5.: Comparison of various amplitude tuners or variable attenuators.

Tuning Element	Operating frequency (GHz)	Return loss (dB)	Attenuation range (dB)
PIN Diode [Wal94]	2.5-5.3	12	2.5-15
Varactor [TW02]	3-4	N.A.	2.2-17
HFET [SZ05]	3-3.4	N.A.	6-30
CMOS [KH10]	8-12	10	8-35
Varactor [BG12]	2.3-2.7	10	1.6-36
Mechanical/piezoactuator [LLP+16]	3.0-3.6	4	5-40
LC, this work	~30	6	11-30

tuned amplitude tuner, for example in [LLP+16]. Moreover, the use of meandered phase shifter or periodic structure such as in [HKG+14] can potentially reduce the phase shifter length.

5

CONCLUSION AND OUTLOOK

Two reconfigurable microwave devices based on LC, which are the bandpass filter and amplitude tuner, have been developed in this work. The devices are fabricated by using printed circuit board (PCB) and low temperature co-fired ceramic (LTCC) technology.

For the bandpass filter, the substrate integrated waveguide (SIW) structure is utilized because it has low losses and potential for low cost fabrication. There are two main parts of the filter development: the filter structure itself and the biasing structure. The PCB technology is utilized for the basic investigations due to its fabrication simplicity. These investigations are performed with the help of magnetic tuning, which is possible for LC-based devices and quite practical for lab-scale demonstrator. To begin the verification of the proposed filter, a single resonator, which is a simple one-pole filter, has been designed, fabricated and measured. The simplest form of resonator, TE_{101} rectangular cavity, has been employed. A rectangular hole is formed in the center of the resonator and later filled with LC. To seal the LC material, two copper plate are glued on the top and bottom of the LC cavity. The structure itself is made of PCB Rogers RT5880 with LPKF ProConduct Paste as the via filling material. After the completion of the fabrication process, the structure is measured with the help of two magnets, producing magnetic field to align the LC directors into perpendicular or parallel state. According to the measurement results, a tunable resonator with unloaded Q-factor of 102–105.6 and tuning range of 412 MHz is achieved for an operating frequency at around 22 GHz.

After a successfull one-pole filter demonstration, the resonators are cascaded to obtain a higher order filter. A higher order filter has the advantage of better rejection in the stopband region of the filter. In this work, a 3-pole filter has been achieved by cascading three LC-based resonators, which are previously investigated. Each resonator is connected by coupling structures, for example by inductive irises. By calculating the respective coupling coefficient, the dimensions of the filter are obtained. The filter itself is designed for an operating frequency at around 22 GHz and bandwidth of 600 MHz. With the same fabrication and measurement process as the single resonator, a filter with a center frequency of 21.45–22.06 GHz is yielded with the insertion loss of 6 dB. The fractional bandwidth variation is 2.81–3.54 %.

Since magnetic alignment device requires a lot of space, electric biasing system is designed for LC-filled SIW bandpass filter. For the PCB technology, the glass structures, in which the metallizations for the structure itself and the biasing lines are formed, can be used. As a separator between both metallizations, a thin layer of silicon nitride (Si_3N_4) is used, which has an excellent breakdown voltage of 600 V/µm. A simple demonstrator, which utilizes a tunable delay line structure, is fabricated and give following results: FoM of 32 °/dB and tuning time of 5 s. However, the integration between the device itself and the biasing structure can be difficult due to the surface roughness of the device. Therefore, another technology, which is LTCC, might answers the problem since the biasing structure and the device are fabricated in the same process.

The LTCC-based LC-filled SIW filter has been demonstrated in Chapter 4 as a part of the Liquida K Project, which is a cooperation between the Institute of Microwave Engineering and Photonics of TU Darmstadt with the German Aerospace Center (DLR), the Federal Institute for Materials Research and Testing (BAM) and IMST GmbH. Since the goal of this project is to make microwave devices for 30 GHz, a filter operating at that frequency is designed with a bandwidth of 3 GHz. As a substrate, Green Tape DuPont 9K7 is used with gold paste as metallization. The biasing line is made of resistive Paste 2061 with resistivity of 200 kΩ/□. GT3-23001 from Merck AG is used for the LC. The LTCC fabrication process is done by BAM. Same as before, a single resonator is fabricated to test the Q-factor of the structure. A resonator with unloaded Q-factor in the range of 68–100 is obtained with a tuning range of 840 MHz (30.16–31 GHz). With fully electrical biasing method, excellent response times are also obtained, which are faster than 2 s. Later, a 3-pole filter has also been fabricated and following results are achieved: operating frequency of 29.4–30.1 GHz, fractional bandwidth of 11.2–11.6 % and insertion loss 2–4 dB. Compared with the other SIW filters in literatures, its unloaded Q-factor is comparable, despite the proposed filter itself works in a higher frequency band. The obtained Q-factor is also higher than the existing LC-based planar filter.

In this work, fundamental structures have been commenced, leaving some room for improvements on the LC-filled SIW filter, for example by using cross-coupling structures. This coupling structure enables us to obtain some transmission zeros resulting in a sharper passband-stopband transition [Hon11]. The advantage of such a filter compared to the high order filter lies in the lower insertion loss. Moreover, miniaturization of the filter, for instance by using dual mode resonator, is another interesting point aspect for future investigations.

The second tunable device, which is the amplitude tuner, has also been demonstrated in Chapter 4. This device has been fabricated with the same technology as the electrically tunable LC-filled SIW filter. The amplitude tuner is based on the interference concept: an input signal is separated into two branches and combined again together at the output port. Before combined together, the signals propagate in two different phase shifter: fixed and tunable. LC is used to construct the tunable phase shifter. When both phase shifters give the same phase shift, the output signal will have a maximum amplitude, since both branch signals add each other. On the other hand, the output amplitude will be minimized when both phase shifters have a 180° difference. Therefore, several subcomponents have been designed, such as the phase shifters, power divider and combiner, as well as the DC-blocking structure to prevent the flowing biasing current. The following structures are used for the phase shifters, power divider/combiner and DC-blocking structure, respectively: striplines, hybrid coupler and electromagnetic coupling structure. Then, a 30 GHz amplitude tuner has been fabricated and measured, showing an attenuation range of 11–30 dB. However, a phase variation up to 94° ocurred, yet, this problem is solved when this amplitude tuner is cascaded with a phase shifter as in the antenna beamforming circuit [Bal12] or clutter canceller system [CKL+12]. Although the initial 11 dB insertion loss is quite high, the amplitude tuner operates at higher frequency than many other similar components known from literatures. For instance, the device in [KH10] gives an insertion loss of 8 dB at 8 GHz. In addition, the proposed LTCC-based amplitude tuner, as well as the filter, is suitable for space applications, which is an improvement compared to other technologies. Since the amplitude tuner is quite large (length around 7 cm), further miniaturization is desired, for example by using meandered phase shifter or periodically loaded structure.

Due to their ability to operate at higher frequency, the LC-based devices are promising to be developed beyond the operating frequency in this work, for example, in future 60 GHz systems [KYO+13]. These tunable devices will add functionality and flexibility of these systems.

BIBLIOGRAPHY

[AGW13] S. Adhikari, A. Ghiotto, and K. Wu. Simultaneous electric and magnetic two-dimensionally tuned parameter-agile SIW devices. *IEEE Transactions on Microwave Theory and Techniques*, 61(1):423–435, Jan 2013.

[ASE10] M. Armendariz, V. Sekar, and K. Entesari. Tunable SIW bandpass filters with PIN diodes. In *The 40th European Microwave Conference*, pages 830–833, Sept 2010.

[Bal12] C.A. Balanis. *Antenna Theory: Analysis and Design.* Wiley, 2012.

[BG12] S. Bulja and A. Grebennikov. Variable reflection-type attenuators based on varactor diodes. *IEEE Transactions on Microwave Theory and Techniques*, 60(12):3719–3727, Dec 2012.

[BML$^+$06] J.F. Bernigaud, N. Martin, P. Laurent, C. Quendo, G. Tanne, B. Della, F. Huret, and Ph. Gelin. Liquid crystal tunable filter based on DBR topology. In *Microwave Conference, 2006. 36th European*, pages 368–371, Sept 2006.

[BMSY$^+$10] S. Bulja, D. Mirshekar-Syahkal, M. Yazdanpanahi, R. James, S. E. Day, and F. A. Fernández. Liquid crystal based phase shifters in 60 GHz band. In *Proc. IEEE . European Wireless Technology Conference (EuWIT), 2010.*, pages 37–40, Paris, France, September 2010.

[Cam99] R. J. Cameron. General coupling matrix synthesis methods for chebyshev filtering functions. *IEEE Transactions on Microwave Theory and Techniques*, 47(4):433–442, Apr 1999.

[CC15] K. K. M. Cheng and M. C. J. Chik. A varactor-based variable attenuator design with enhanced linearity performance. *IEEE Transactions on Microwave Theory and Techniques*, 63(10):3191–3198, Oct 2015.

[CD85] J. Clarke and M. R. B. Dunsmore. High-power tunable YIG filters. *IEE Proceedings H - Microwaves, Antennas and Propagation*, 132(4):251–254, July 1985.

[CKL$^+$12] H. R. Chuang, H. C. Kuo, F. L. Lin, T. H. Huang, C. S. Kuo, and Y. W. Ou. 60-GHz millimeter-wave life detection system (MLDS) for noncontact human vital-signal monitoring. *IEEE Sensors Journal*, 12(3):602–609, March 2012.

[CW09] Xiao-Ping Chen and Ke Wu. Low-loss ultra-wideband transition between conductor-backed coplanar waveguide and substrate integrated waveguide. In *Microwave Symposium Digest, 2009. MTT '09. IEEE MTT-S International*, pages 349–352, June 2009.

[CW14] Xiao-Ping Chen and Ke Wu. Substrate integrated waveguide filter: Basic design rules and fundamental structure features. *Microwave Magazine, IEEE*, 15(5):108–116, July 2014.

[dJ79] W. H. de Jeu. *Physical Properties of Liquid Crystalline Materials*. Gordon and Breach, New York, USA, 1979.

[Dre10] C. Drentea. *Modern Communications Receiver Design and Technology*. Artech House intelligence and information operations series. Artech House, 2010.

[DuP09a] DuPont. *DuPont LL500 Co-fired gold via fill*, 10 2009.

[DuP09b] DuPont. *DuPont^{TM} GreenTape^{TM} low temperature co-fired ceramic system*, 11 2009.

[DuP12] DuPont. *DuPont LL505 Co-fired, wire bondable gold conductor*, 12 2012.

[Ell93] Robert S. Elliott. *Electromagnetics History, Theory, and Application*. IEEE Press, Piscataway, NJ, USA, 1993.

[FGK$^+$12] Carsten Fritzsch, Flavio Giacomozzi, Onur Hamza Karabey, Saygin Bildik, Sabrina Colpo, and Rolf Jakoby. Advanced characterization of a W-band phase shifter based on liquid crystals and MEMS technology. *International Journal of Microwave and Wireless Technologies*, 4(3):379–386, 2012.

[FGPJ14] T. Franke, A. Gaebler, A. E. Prasetiadi, and R. Jakoby. Tunable Ka-band waveguide resonators and a small band band-pass filter based on liquid crystals. In *Microwave Conference (EuMC), 2014 44th European*, pages 339–342, Oct 2014.

[FKR$^+$13] Anne-Laure Franc, Onur Hamza Karabey, Gustavo Rehder, Emmanuel Pistono, Rolf Jakoby, and Philippe Ferrari. Compact and broadband millimeter-wave electrically tunable phase shifter combining slow-wave effect with liquid crystal technology. 61:3905–3915, November 2013.

[GGG$^+$09] F. Goelden, A. Gaebler, M. Goebel, A. Manabe, S. Mueller, and R. Jakoby. Tunable liquid crystal phase shifter for microwave frequencies. *Electronics Letters*, 45(13):686–687, June 2009.

[GGK$^+$10] F. Goelden, A. Gaebler, O. Karabey, M. Goebel, A. Manabe, and R. Jakoby. Tunable band-pass filter based on liquid crystal. In *Microwave Conference, 2010 German*, pages 98–101, March 2010.

[GGM$^+$09] A. Gaebler, F. Goelden, A. Manabe, M. Goebel, S. Mueller, and R. Jakoby. Investigation of high performance transmission line phase shifters based on liquid crystal. In *Proc. IEEE . 39th European Microwave Conference*, pages 594–597, Rome, Italy, September 2009.

[GGMJ08] A. Gaebler, F. Goelden, S. Mueller, and R. Jakoby. Modeling of electrically tunable transmission line phase shifter based on liquid crystal. In *Antennas and Propagation Society International Symposium, 2008. AP-S 2008. IEEE*, pages 1–4, July 2008.

[GMG$^+$09] A. Gaebler, A. Moessinger, F. Goelden, A. Manabe, M. Goebel, R. Follmann, D. Koether, C. Modes, A. Kipka, M. Deckelmann, T. Rabe, B. Schulz, P. Kuchenbecker, A. Lapanik, S. Mueller, W. Haase, and R. Jakoby. Liquid crystal-reconfigurable antenna concepts for space applications at microwave and millimeter waves. *International Journal of Antennas and Propagation*, 2009:1–7, Jan 2009.

[Göl10] Felix Gölden. *Liquid Crystal Based Microwave Components with Fast Response Times: Material, Technology, Power Handling Capability.* PhD thesis, Technische Universität Darmstadt, Darmstadt, March 2010.

[HKG$^+$14] Wenjuan Hu, O.H. Karabey, A. Gabler, A. E. Prasetiadi, M. Jost, and R. Jakoby. Liquid crystal varactor loaded variable phase shifter for integrated, compact, and fast beamsteering antenna systems. In *European Microwave Integrated Circuit Conference (EuMIC), 2014 9th*, pages 660–663, Oct 2014.

[Hon11] J.S. Hong. *Microstrip Filters for RF / Microwave Applications.* Wiley Series in Microwave and Optical Engineering. Wiley, 2011.

[JSH$^+$15] M. Jost, S. Strunck, A. Heunisch, A. Wiens, A.E. Prasetiadi, C. Weickhmann, B. Schulz, M. Quibeldey, O.H. Karabey, T. Rabe, R. Follmann, D. Koether, and R. Jakoby. Continuously tuneable liquid crystal based stripline phase shifter realised in LTCC technology. In *Microwave Conference (EuMC), 2015 European*, pages 1260–1263, Sept 2015.

[Kar14] Onur Hamza Karabey. *Electronic Beam Steering and Polarization Agile Planar Antennas in Liquid Crystal Technology.* Springer International Publishing, Switzerland, 2014.

[KFN02] T. Kuki, H. Fujikake, and T. Nomoto. Microwave variable delay line using dual-frequency switching-mode liquid crystal. *IEEE Transactions on Microwave Theory and Techniques*, 50(11):2604–2609, Nov 2002.

[KGSJ12] O. H. Karabey, A. Gaebler, S. Strunck, and R. Jakoby. A 2-d electronically steered phased-array antenna with 2 x 2 elements in LC display technology. *IEEE Transactions on Microwave Theory and Techniques*, 60(5):1297–1306, May 2012.

[KH10] B. H. Ku and S. Hong. 6-bit CMOS digital attenuators with low phase variations for X-band phased-array systems. *IEEE Transactions on Microwave Theory and Techniques*, 58(7):1651–1663, July 2010.

[KSF$^+$11] O. H. Karabey, B. G. Saavedra, C. Fritzsch, S. Strunck, A. Gaebler, and R. Jakoby. Methods for improving the tuning efficiency of liquid crystal based tunable phase shifters. In *European Microwave Integrated Circuits Conference (EuMIC)*, pages 494–497, Oct 2011.

[KYO$^+$13] H. C. Kuo, H. L. Yue, Y. W. Ou, C. C. Lin, and H. R. Chuang. A 60-GHz-CMOS sub-harmonic RF receiver with integrated on-chip artificial-magnetic-conductor yagi antenna and balun bandpass filter for very-short-range gigabit communications. *IEEE Transactions on Microwave Theory and Techniques*, 61(4):1681–1691, April 2013.

[Lee04] T.H. Lee. *Planar Microwave Engineering: A Practical Guide to Theory, Measurement, and Circuits.* Number v. 1. Cambridge University Press, 2004.

[LLP$^+$16] T. H. Lee, K. Lee, G. C. Park, Y. S. Kim, and J. Lee. Bandstop filter (BSF) topology with variable attenuation. *IEEE Transactions on Microwave Theory and Techniques*, 64(2):467–474, Feb 2016.

[LPK14] LPKF. *Chemiefreie Durchkontaktierung fuer das PCB-Prototyping LPKF ProConduct*, 11 2014.

[Mar51] N. Marcuvitz. *Waveguide handbook.* Radiation Laboratory series. McGraw-Hill, 1951.

[MFBJ10] A. Moessinger, C. Fritzsch, S. Bildik, and R. Jakoby. Compact tunable Ka-band phase shifter based on liquid crystals. In *Microwave Symposium Digest (MTT), 2010 IEEE MTT-S International*, pages 1020–1023, May 2010.

[Mis01] D.K. Misra. *Radio-Frequency and Microwave Communication Circuits: Analysis and Design.* Wiley, 2001.

[MNS⁺16] H. Maune, M. Nikfalazar, C. Schuster, T. Franke, W. Hu, M. Nickel, D. Kienemund, A. Prasetiadi, C. Weickhmann, M. Jost, A. Wiens, and R. Jakoby. Tunable microwave component technologies for satcom-platforms. In *2016 German Microwave Conference (GeMiC)*, pages 23–26, March 2016.

[MSW⁺04] S. Mueller, P. Scheele, C. Weil, M. Wittek, C. Hock, and R. Jakoby. Tunable passive phase shifter for microwave applications using highly anisotropic liquid crystals. In *IEEE MTT-S International Microwave Symposium Digest (IEEE Cat. No.04CH37535)*, volume 2, pages 1153–1156 Vol.2, June 2004.

[MYJ80] George Matthaei, Leo Young, and E.M.T. Jones. *Microwave filters, impedance-matching networks and coupling structures.* Artech House, Norwood, MA, USA, 1980.

[OM72] T. Okoshi and T. Miyoshi. The planar circuit - an approach to microwave integrated circuitry. *IEEE Transactions on Microwave Theory and Techniques*, 20(4):245–252, Apr 1972.

[Par72] W. J. Parris. P-i-n variable attenuator with low phase shift (short papers). *IEEE Transactions on Microwave Theory and Techniques*, 20(9):618–620, Sep 1972.

[Poz11] David M. Pozar. *Microwave engineering.* John Wiley & Sons, Inc., United States of America, fourth edition, 2011.

[Rah15] Sabrina Rahmawati. Investigation of electrical biasing schemes for substrate integrated waveguide (SIW) tunable devices based on liquid crystal (LC) technology. Master's thesis, Technische Universitaet Darmstadt, Darmstadt, 2015.

[RER⁺09] G. M. Rebeiz, K. Entesari, I. C. Reines, S. j. Park, M. A. El-tanani, A. Grichener, and A. R. Brown. Tuning in to RF MEMS. *IEEE Microwave Magazine*, 10(6):55–72, Oct 2009.

[Ric15] Martin Rickes. Design und fertigung eines LC-hohlleiter phasenschiebers fuer 250 GHz. Master's thesis, Technische Universitaet Darmstadt, Darmstadt, 2015.

[Rog16a] Rogers Corporation. *RO4000 Series High Frequency Circuit Materials*, 10 2016.

[Rog16b] Rogers Corporation. *RT/duroid 5870/5880 High Frequency Laminates*, 03 2016.

[SA51] W. Sichak and H. Augenblick. Tunable waveguide filters. *Proceedings of the IRE*, 39(9):1055–1059, Sept 1951.

[SAE11] V. Sekar, M. Armendariz, and K. Entesari. A 1.2-1.6-GHz substrate-integrated-waveguide RF MEMS tunable filter. *Microwave Theory and Techniques, IEEE Transactions on*, 59(4):866–876, April 2011.

[SGK$^+$15] Sebastian Strunck, Alexander Gaebler, Onur H. Karabey, Andreas Heunisch, Baerbel Schulz, Torsten Rabe, Ruediger Follmann, Juergen Kassner, Dietmar Koether, Atsutaka Manabe, and Rolf Jakoby. Reliability study of a tunable Ka-band SIW-phase shifter based on liquid crystal in LTCC-technology. *International Journal of Microwave and Wireless Technologies*, 7:521–527, 10 2015.

[SKGJ12] S. Strunck, O. H. Karabey, A. Gaebler, and R. Jakoby. Reconfigurable waveguide polariser based on liquid crystal for continuous tuning of linear polarisation. *Electronics Letters*, 48(8):441–443, April 2012.

[SL02] O. V. Stoukatch and L. P. Ligthart. Attenuator with small phase shift for ultra-wideband pulse subsurface geo-radar. In *Microwave Conference, 2002. 32nd European*, pages 1–3, Sept 2002.

[SMTB11] S. Sirci, J.D. Martinez, M. Taroncher, and V.E. Boria. Varactor-loaded continuously tunable SIW resonator for reconfigurable filter design. In *Microwave Conference (EuMC), 2011 41st European*, pages 436–439, Oct 2011.

[SS74] Michael J. Stephen and Joseph P. Straley. Physics of liquid crystals. *Rev. Mod. Phys.*, 46:617–704, Oct 1974.

[Stu06] O. V. Stukach. Variable attenuator with low phase shift. In *European Conference on Wireless Technology*, pages 241–244, Sept 2006.

[Sva92] J. Svacina. Analysis of multilayer microstrip lines by a conformal mapping method. *IEEE Transactions on Microwave Theory and Techniques*, 40(4):769–772, Apr 1992.

[Sva06] Jiri Svacina. New method for analysis of microstrip with finite-width ground plane. *Microwave and Optical Technology Letters*, 48(2):396–399, 2006.

[SZ05] C. E. Saavedra and You Zheng. Ring-hybrid microwave voltage-variable attenuator using HFET transistors. *IEEE Transactions on Microwave Theory and Techniques*, 53(7):2430–2434, July 2005.

[TL06] Chih-Ming Tsai and Hong-Ming Lee. The effects of component q distribution on microwave filters. *IEEE Transactions on Microwave Theory and Techniques*, 54(4):1545–1553, June 2006.

[TOD14] N. Takbiri, A. Oncu, and R. Dasbasi. 360^0 variable microwave phase shifter design for clutter cancellation circuitry of life detecting radar. In *Microwaves, Radar, and Wireless Communication (MIKON), 2014 20th International Conference on*, pages 1–4, June 2014.

[TW02] C. R. Trent and T. M. Weller. S-band reflection type variable attenuator. *IEEE Microwave and Wireless Components Letters*, 12(7):243–245, July 2002.

[Wal94] S. Walker. A low phase shift attenuator. *IEEE Transactions on Microwave Theory and Techniques*, 42(2):182–185, Feb 1994.

[Wen69] C. P. Wen. Coplanar waveguide: A surface strip transmission line suitable for nonreciprocal gyromagnetic device applications. *IEEE Transactions on Microwave Theory and Techniques*, 17(12):1087–1090, Dec 1969.

[WFJD07] E. Willman, F. A. Fernandez, R. James, and S. E. Day. Modeling of weak anisotropic anchoring of nematic liquid crystals in the landau-de gennes theory. *IEEE Transactions on Electron Devices*, 54(10):2630–2637, Oct 2007.

[WJCL13] C. Weickhmann, R. Jakoby, E. Constable, and R. A. Lewis. Time-domain spectroscopy of novel nematic liquid crystals in the terahertz range. In *2013 38th International Conference on Infrared, Millimeter, and Terahertz Waves (IRMMW-THz)*, pages 1–2, Sept 2013.

[WLJ02] C. Weil, G. Luessem, and R. Jakoby. Tunable inverted-microstrip phase shifter device using nematic liquid crystals. In *Microwave Symposium Digest, 2002 IEEE MTT-S International*, volume 1, pages 367–371 vol.1, June 2002.

[WNG$^+$13a] C. Weickhmann, N. Nathrath, R. Gehring, A. Gaebler, M. Jost, and R. Jakoby. A light-weight tunable liquid crystal phase shifter for an efficient phased array antenna. In *2013 European Microwave Conference*, pages 428–431, Oct 2013.

[WNG$^+$13b] C. Weickhmann, N. Nathrath, R. Gehring, A. Gaebler, M. Jost, and R. Jakoby. Recent measurements of compact electronically tunable liquid crystal phase shifter in rectangular waveguide topology. *Electronics Letters*, 49(21):1345–1347, October 2013.

[Wol09] I. Wolff. From antennas to microwave systems - LTCC as an integration technology for space applications. In *3rd European Conference on Antennas and Propagation*, pages 3–8, March 2009.

[XW05] Feng Xu and Ke Wu. Guided-wave and leakage characteristics of substrate integrated waveguide. *IEEE Transactions on Microwave Theory and Techniques*, 53(1):66–73, Jan 2005.

[YFB$^+$12] P. Yaghmaee, C. Fumeaux, B. Bates, A. Manabe, O.H. Karabey, and R. Jakoby. Frequency tunable S-band resonator using nematic liquid crystal. *Electronics Letters*, 48(13):798–800, June 2012.

[YMS12] M. Yazdanpanahi and D. Mirshekar-Syahkal. Millimeter-wave liquid-crystal-based tunable bandpass filter. In *Radio and Wireless Symposium (RWS), 2012 IEEE*, pages 139–142, Jan 2012.

[YW06] Deng-Ke Yang and Shin-Tson Wu. *Fundamentals of Liquid Crystal Devices.* John Wiley & Sons, Ltd., Chichester, UK, 2006.

[ZM04] Lei Zhu and W. Menzel. Broad-band microstrip-to-CPW transition via frequency-dependent electromagnetic coupling. *IEEE Transactions on Microwave Theory and Techniques*, 52(5):1517–1522, May 2004.

[ZSM$^+$11] Y. Zheng, M. Sazegar, H. Maune, X. Zhou, J. R. Binder, and R. Jakoby. Compact substrate integrated waveguide tunable filter based on ferroelectric ceramics. *IEEE Microwave and Wireless Components Letters*, 21(9):477–479, Sept 2011.

[ZYP$^+$07] C. Zhang, S. Yang, H. K. Pan, A. E. Fathy, S. El-Ghazaly, and V. Nair. Reconfigurable antenna for simultaneous multi-service wireless applications. In *2007 IEEE Radio and Wireless Symposium*, pages 543–546, Jan 2007.

A

PHOTOLITHOGRAPHY FABRICATION PROCESS PARAMETERS

The following parameters are used to develop the biasing structure in Chapter 3.

Metallic Layer

Chromium (Cr) : 20 nm
Gold (Au) : 60 nm

Spin Coating

Photoresist : AZ 4533
Speed : 4000 rpm
Duration : 40 s

Pre-exposure Bake

Temperature : 90 °C
Duration : 3 min.

UV light Exposure

Duration : 35 s

Photoresist Development

Developer : AZ400K 1:4
Duration : 35 s

Etching

Duration : 9 s (Au) and 11 s (Cr)

B

ANALYSIS OF AN LC-FILLED STRIPLINE

The term stripline used in this work refers to a pair of parallel strips with the same width separated by dielectric material. In this case, the LC fills the gap between those strips and the structure is embedded inside the LTCC structure, as shown in Fig. B.1.

The important property will be examined is the dependency between the relative permittivity of LC $\varepsilon_{r,\mathrm{LC}}$, which is tunable, to the effective relative permittivity of the structure ε_r. One of the analytical method can be utilized is the moving perfect electric wall (MPEW) [Sva06]. The idea is to introduce a perfect electric wall inside the stripline structure which divides the stripline structure into two microstrip lines (MSL) as shown in Fig. B.1. For a symmetric stripline like in our case, the model can be simplified so that the electric wall is placed in the center of the structure ($h_1 = h_2 = h/2$ for $w_1 = w_2 = w$). Therefore, the MPEW analysis equations in [Sva06] can be reduced into:

$$\varepsilon_{r,\mathrm{S}} = \varepsilon_{r,\mathrm{MSL2}}, \tag{B.0.17}$$

where $\varepsilon_{r,\mathrm{S}}$ and $\varepsilon_{r,\mathrm{MSL2}}$ denote the effective permittivity of the stripline structure and the effective permittivity of its equivalent MSL structure (with the height of LC layer of $h/2$), respectively.

The result presented in Eq. B.0.17 is interesting since the effective relative permittivity of the stripline structure is equal to the MSL model, which its height is half of the stripline. Physically speaking, the less equivalent height of LC (h_{LC}) compared to an

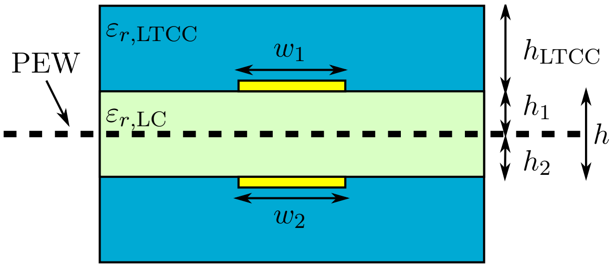

Figure B.1.: The moving perfect electric wall method for stripline analysis. A perfect electric wall (PEW) is inserted in the middle of the structure creating two MSL with height of h_1 and h_2.

MSL with a height of h cause the electric field concentrates more on the LC part, which makes the tuning more efficient. Moreover, the real height is still h which give this stripline structure an advantage in term of metallic losses compared to an MSL structure with a height of $h/2$.

The next step to be done is to find the effect of the LC and LTCC permittivity to the overall effective permittivity. Using the conformal mapping method (CMM) [Sva92], which is already applied for the LC-based MSL structure [KSF$^+$11], the effective permittivity can be calculated as the followings for $w/h_{\mathrm{LC}} \geq 1$:

$$\varepsilon_{r,\mathrm{S}} = \varepsilon_{r,\mathrm{MSL2}} = \varepsilon_{r,\mathrm{LC}} \cdot q_1 + \varepsilon_{r,\mathrm{LTCC}} \cdot \frac{(1-q_1)^2}{\varepsilon_{r,\mathrm{LTCC}}\,(1-q_1-q_2)+q_2}, \tag{B.0.18}$$

where:

$$q_1 = 1 - \frac{1}{2} \cdot \frac{\ln\left(\dfrac{\pi w_{\mathrm{eff}}}{h_{\mathrm{LC}}} - 1\right)}{\dfrac{w_{\mathrm{eff}}}{h_{\mathrm{LC}}}} \tag{B.0.19}$$

$$q_2 = 1 - q_1 - \frac{1}{2} \cdot \frac{h_{\mathrm{LC}} - v_\epsilon}{w_{\mathrm{eff}}} \cdot \ln\left(\pi \frac{w_{\mathrm{eff}}}{h_{\mathrm{LC}}} \frac{\cos\left(\dfrac{v_\epsilon}{2} \cdot \dfrac{\pi}{h_{\mathrm{LC}}}\right)}{\pi\left(\dfrac{h_{\mathrm{LC}} + h_{\mathrm{LTCC}}}{h_{\mathrm{LC}}} - \dfrac{1}{2}\right) + \dfrac{v_\epsilon}{2} \cdot \dfrac{\pi}{h_{\mathrm{LC}}}} + \sin\left(\frac{v_\epsilon}{2} \cdot \frac{\pi}{h_{\mathrm{LC}}}\right)\right) \tag{B.0.20}$$

$$w_{\mathrm{eff}} = w + \frac{2h_{\mathrm{LC}}}{\pi} \ln\left(17.08\left(\frac{w}{2h_{\mathrm{LC}}} + 0.92\right)\right) \tag{B.0.21}$$

$$v_\epsilon = 2\frac{h_{\mathrm{LC}}}{\pi} \tan^{-1}\left(\frac{\pi}{\dfrac{\pi}{2}\dfrac{w_{\mathrm{eff}}}{h_{\mathrm{LC}}} - 2}\left(\frac{h_{\mathrm{LC}} + h_{\mathrm{LTCC}}}{h_{\mathrm{LC}}} - 1\right)\right). \tag{B.0.22}$$

Remember that $h_{\mathrm{LC}} = h/2$ in this case (see Fig. B.1).

For a clear overview, the effective relative permittivity of the stripline is plotted versus the relative permittivity of LC, as exhibited in Fig. B.2. The obtained dimensions from Subsection 4.3.2 are used. As a comparison, simulations using CST Microwave Studio are also performed and give difference less than 3.9 % which is quite accurate.

For tunability comparison, an MSL structure with $h_{\mathrm{LC}} = h$ is also simulated and depicted in Fig. B.3. From this result, the tunability of the stripline structure is 9.7 % better than the MSL structure according to the tuning efficiency definition [KSF$^+$11]:

$$\eta_\tau = \frac{\Delta\varepsilon_{r,\mathrm{eff}}}{\Delta\varepsilon_{r,\mathrm{LC}}}, \tag{B.0.23}$$

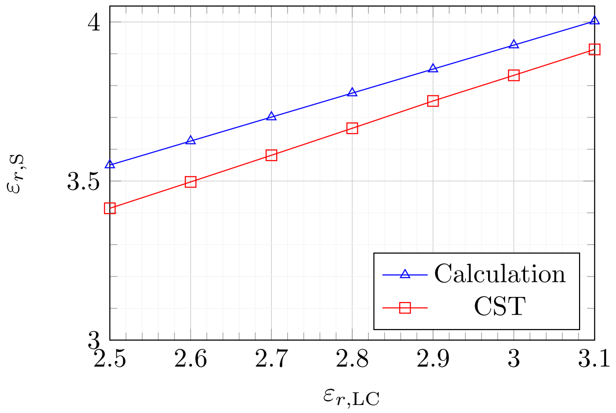

Figure B.2.: The relation between the permittivity of LC ($\varepsilon_{r,\mathrm{LC}}$) and effective permittivty of the stripline structure ($\varepsilon_{r,\mathrm{S}}$).

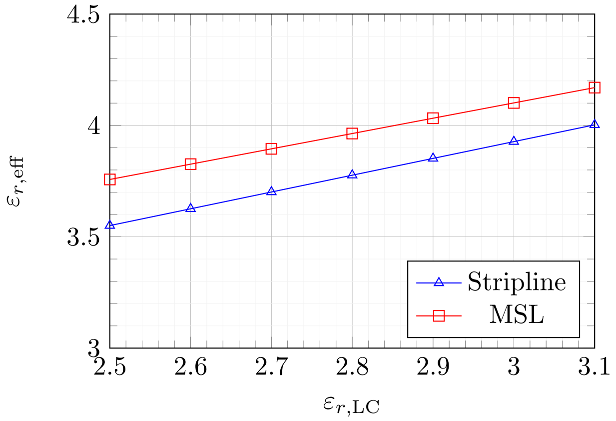

Figure B.3.: Comparation of the effective permittitivty ($\varepsilon_{r,\mathrm{eff}}$) of stripline and MSL structure.

where η_τ is the tuning efficiency, $\Delta\varepsilon_{r,\mathrm{eff}}$ is the difference of the effective relative permittivity of the structure and $\Delta\varepsilon_{r,\mathrm{LC}}$ is the difference of the relative permittivity of the LC. The higher values of the $\varepsilon_{r,\mathrm{MSL}}$ indicate the larger influence of the LTCC material which has larger permittivity than LC. Since it is a non-tunable material, the tuning efficiency is reduced. This result is also confirmed by our in-house simulation tool [GGMJ08] which indicates the tuning efficiency is 8.2 % better with stripline topology.

C

MODIFIED T-PARAMETER FOR CASCADED 4-PORT COMPONENTS

When a microwave component is cascaded with another component, it is convenient to use the transfer scattering parameter or T-parameter. It could be modified from the definition of S-parameter for a device with N ports:

$$\begin{aligned} \begin{bmatrix} b \end{bmatrix} &= \begin{bmatrix} S \end{bmatrix} \begin{bmatrix} a \end{bmatrix} \\ \begin{bmatrix} b_1 \\ b_2 \\ \vdots \\ b_N \end{bmatrix} &= \begin{bmatrix} S_{11} & S_{12} & \dots & S_{1N} \\ S_{21} & S_{22} & \dots & S_{2N} \\ \vdots & \vdots & \ddots & \vdots \\ S_{N1} & S_{N2} & \dots & S_{NN} \end{bmatrix} \begin{bmatrix} a_1 \\ a_2 \\ \vdots \\ a_N \end{bmatrix}, \end{aligned} \tag{C.0.24}$$

where $[a]$ and $[b]$ are the incident and reflected waves matrices, which its contents represent the wave at the first until the N-th port. $[S]$ is the S-parameter matrix which size is $N \times N$. T-parameter could be defined by changing the position of the elements in $[a]$ and $[b]$. For example, the corresponding T-parameter for a two-ports network (see Fig. C.1a) is [Mis01]:

$$\begin{bmatrix} a_1 \\ b_1 \end{bmatrix} = \begin{bmatrix} T_{11} & T_{12} \\ T_{21} & T_{22} \end{bmatrix} \begin{bmatrix} b_2 \\ a_2 \end{bmatrix}. \tag{C.0.25}$$

In Eq. C.0.25, the element of $[a]$ and $[b]$ which belong to the first port are arranged together in the left side of the equation. The elements of the second port are grouped on the right side of the equation. Note that the reflected wave of the second port b_2 is placed as the first element of matrix unlike the matrix for the first port. This is useful for a cascade configuration. Suppose we have two microwave devices A and B (see Fig. C.1b) with S-parameters of $[S_A]$ and $[S_B]$. The T-parameters for both device are $[S_A]$ and $[S_B]$ so that:

$$\begin{bmatrix} a_{1A} \\ b_{1A} \end{bmatrix} = \begin{bmatrix} T_A \end{bmatrix} \begin{bmatrix} b_{2A} \\ a_{2A} \end{bmatrix} \tag{C.0.26}$$

$$\begin{bmatrix} a_{1B} \\ b_{1B} \end{bmatrix} = \begin{bmatrix} T_B \end{bmatrix} \begin{bmatrix} b_{2B} \\ a_{2B} \end{bmatrix}. \tag{C.0.27}$$

Since the reflected wave b_{2A} serves as the incident wave for device B a_{1B} (or $b_{2A} = a_{1B}$) and vice versa ($a_{2A} = b_{1B}$), the cascaded T-parameter ($[T_{\text{cas}}]$) can be calculated by using Eq. C.0.26 and Eq. C.0.27:

$$\begin{aligned} \begin{bmatrix} a_{1A} \\ b_{1A} \end{bmatrix} &= \begin{bmatrix} T_A \end{bmatrix} \begin{bmatrix} b_{2A} \\ a_{2A} \end{bmatrix} \\ \begin{bmatrix} a_{1A} \\ b_{1A} \end{bmatrix} &= \begin{bmatrix} T_A \end{bmatrix} \begin{bmatrix} a_{1B} \\ b_{1B} \end{bmatrix} \\ \begin{bmatrix} a_{1A} \\ b_{1A} \end{bmatrix} &= \begin{bmatrix} T_A \end{bmatrix} \begin{bmatrix} T_B \end{bmatrix} \begin{bmatrix} b_{2B} \\ a_{2B} \end{bmatrix}. \end{aligned} \tag{C.0.28}$$

Hence:

$$\begin{bmatrix} T_{\text{cas}} \end{bmatrix} = \begin{bmatrix} T_A \end{bmatrix} \begin{bmatrix} T_B \end{bmatrix}. \tag{C.0.29}$$

Using this idea, the T-parameter for 4-ports device, as shown in Fig. C.1c, could be defined as:

$$\begin{bmatrix} a_1 \\ b_1 \\ a_4 \\ b_4 \end{bmatrix} = \begin{bmatrix} T_{11} & T_{12} & T_{13} & T_{14} \\ T_{21} & T_{22} & T_{23} & T_{24} \\ T_{31} & T_{32} & T_{33} & T_{34} \\ T_{41} & T_{42} & T_{43} & T_{44} \end{bmatrix} \begin{bmatrix} b_2 \\ a_2 \\ b_3 \\ a_3 \end{bmatrix}. \tag{C.0.30}$$

Similar to Eq. C.0.29, the T-parameter of cascaded devices can be calculated by multiplying the T-parameter of each device.

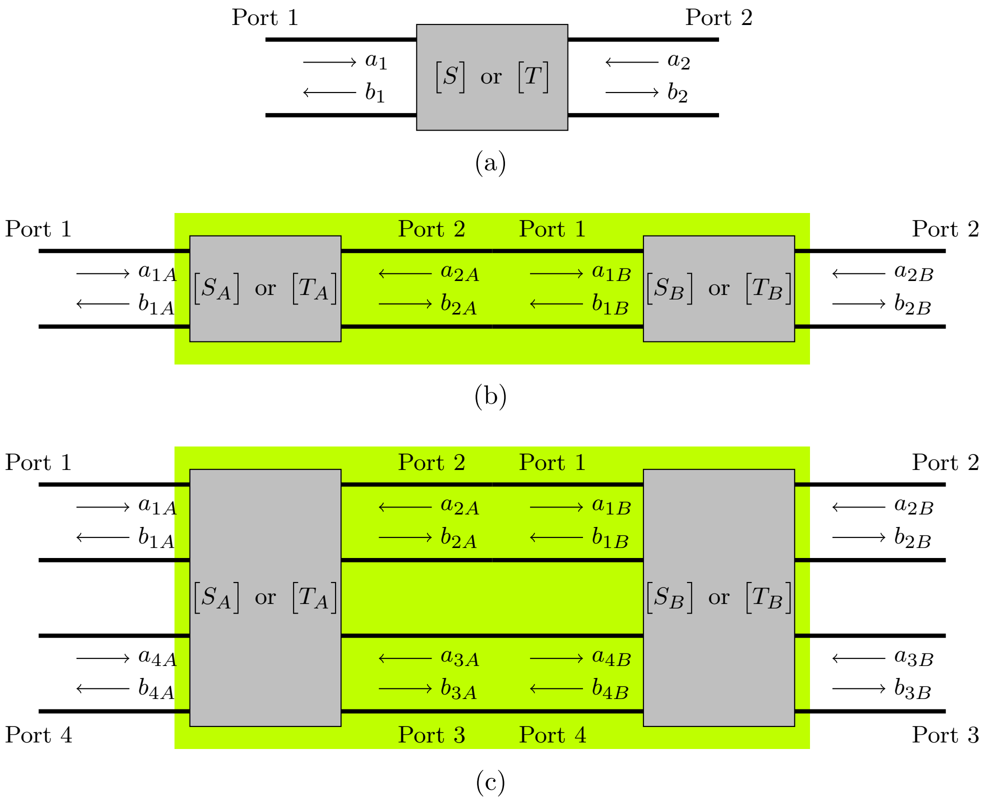

Figure C.1.: (a) Incident wave a_n and reflected wave b_n at the n-th port. (b) Two cascaded microwave devices with S-parameter of $[S_A]$ and $[S_B]$. (c) Cascaded four-ports networks.

LIST OF ABBREVIATIONS

BAM	*Bundesanstalt für Materialforschung und -prüfung* (Federal Institute for Materials Research and Testing)
BST	Barium strontium titanate
CPW	Coplanar waveguide
CST	Computer Simulation Technology
DC	Direct current
DLR	*Deutschen Zentrums für Luft- und Raumfahrt* (German Aerospace Center)
FBW	Fractional bandwidth
FET	Field-effect transistors
FoM	Figure of merit
GCPW	Grounded coplanar waveguide
GSG	Ground-signal-ground
IL	Insertion loss
LC	Liquid crystal
LCD	Liquid crystal display
LLC	Lossless liquid crystal
LTCC	Low temperature co-fired ceramic
MEMS	Microelectromechanical systems
MSL	Microstrip line
PCB	Printed circuit board
PEC	Perfect electric conductor
PECVD	Plasma-enhanced chemical vapor deposition
Q-factor	Quality factor
RF	Radio frequency
SIW	Substrate integrated waveguide
TE	Transverse electric
TEM	Transverse electromagnetic
TM	Transverse magnetic
UV	Ultraviolet
VNA	Vector network analyzer
YIG	Yttrium-iron-garnet

LIST OF SYMBOLS

a	Physical width of a substrate integrated waveguide structure
a_{eff}	Effective width of a substrate integrated waveguide structure
a_i	Width of an iris structure
a_{LC}	Width of the liquid crystal cavity inside a resonator
B_w	Bandwidth
β	Phase constant of a transmission line
χ_e	Electric susceptibility
χ_m	Magnetic susceptibility
d_{via}	Diameter of metallic via for a substrate integrated waveguide structure
$\Delta\phi$	Differential phase shift of a tunable delay line
$\vec{E}$	Electric field
ε_0	Vacuum permittivity
ε_r	Relative permittivity of a material
$\varepsilon_{r,\text{eff}}$	Effective relative permittivity
$\varepsilon_{r,\parallel}$	Relative permittivity of liquid crystal in parallel state
$\varepsilon_{r,\perp}$	Relative permittivity of liquid crystal in perpendicular state
f_0	Resonant frequency of a resonator
FBW	Fractional bandwidth
FoM	Figure of Merit for a tunable delay line
g_i	i-th element value of a lowpass prototype
$\vec{H}$	Magnetic field
h_{LC}	Height of a liquid crystal layer
IL	Insertion loss
K	Characteristic impedance of an inverter
k	Coupling coefficient between two resonators
l_{res}	Length of a resonator
μ_0	Vacuum permeability
μ_r	Relative permeability of a material
$\vec{n}$	Director of liquid crystal
$\vec{P}$	Electric polarization
p_{via}	Pitch between adjacent vias for a substrate integrated waveguide structure
ϕ_{diff}	The phase difference between branches in an amplitude tuner

Q	Quality factor of a resonator
Q_e	External quality factor of a resonator
Q_L	Loaded quality factor of a resonator
Q_u	Unloaded quality factor of a resonator
S	Order parameter of liquid crystal
σ	Material conductivity
$\tan\,\delta$	Loss tangent of a material
$\tan\,\delta_{\|}$	Loss tangent of liquid crystal in parallel state
$\tan\,\delta_{\perp}$	Loss tangent of liquid crystal in perpendicular state
T_c	Clearing point of liquid crystal
t_{fall}	the required time to tune from 90% to 10% of the maximum differential phase shift
T_m	Melting point of liquid crystal
t_{rise}	the required time to tune from 10% to 90% of the maximum differential phase shift
τ_{res}	Tunability of a resonator
V_0	Fixed voltage in a fully electric biasing scheme of liquid crystal
V_b	Tunable voltage in a fully electric biasing scheme of liquid crystal
$V_{\|}$	Tunable voltage to control the parallel state of the liquid crystal in a stripline phase shifter
$V_{\perp}$	Tunable voltage to control the perpendicular state of the liquid crystal in a stripline phase shifter
x_i	Reactance slope parameter for i-th resonator

LIST OF PUBLICATIONS, AWARD AND SUPERVISED THESIS

PUBLICATIONS

Journals

1. **A. E. Prasetiadi**, O. H. Karabey, C. Weickhmann, T. Franke, W. Hu, M. Jost, M. Nickel, and R. Jakoby, "Continuously tunable substrate integrated waveguide bandpass filter in liquid crystal technology with magnetic biasing," in *Electronics Letters*, vol. 51, no. 20, pp. 1584-1585, 10 1 2015.
2. H. Maune, M. Jost, A. Wiens, C. Weickhmann, R. Reese, M. Nikfalazar, C. Schuster, T. Franke, W. Hu, M. Nickel, D. Kienemund, **A. E. Prasetiadi** and R. Jakoby, "Tunable Microwave Component Technologies for SatCom-Platforms," in *Frequenz*, vol. 71, no.3-4, pp. 129-142, 2017.

Conferences

1. **A. E. Prasetiadi**, M. Jost, B. Schulz, M. Quibeldey, T. Rabe, R. Follmann and R. Jakoby, "Liquid-Crystal-Based Amplitude Tuner Fabricated in LTCC Technology," accepted in *47th European Microwave Conference (EUMC)*, Nürnberg, 2017.
2. **A. E. Prasetiadi**, S. Rahmawati, C. Weickhmann, M. Nickel, M. Jost, T. Franke, W. Hu, H. Maune and R. Jakoby., "Electrical biasing scheme for Liquid-Crystal-based tunable Substrate Integrated Waveguide structures," *German Microwave Conference (GeMiC)*, Bochum, 2016, pp. 136-139.
3. H. Maune, M. Nikfalazar, C. Schuster, T. Franke, W. Hu, M. Nickel, D. Kienemund, **A. E. Prasetiadi**, C. Weickhmann, M. Jost, A. Wiens and R. Jakoby, "Tunable microwave component technologies for SatCom-platforms," *German Microwave Conference (GeMiC)*, Bochum, 2016, pp. 23-26.
4. M. Jost, S. Strunck, A. Heunisch, A. Wiens, **A. E. Prasetiadi**, C. Weickhmann, B. Schulz, M. Quibeldey, O. H. Karabey, T. Rabe, R. Follmann, D. Koether and R. Jakoby, "Continuously tuneable liquid crystal based stripline phase shifter realised in LTCC technology," *10th European Microwave Integrated Circuits Conference (EuMIC)*, Paris, 2015, pp. 409-412.
5. M. Jost, C. Weickhmann, T. Franke, **A. E. Prasetiadi**, W. Hu, M. Nickel, O. Karabey and R. Jakoby, "Tuneable hollow waveguide devices for space applica-

tions based on liquid crystal," *SBMO/IEEE MTT-S International Microwave and Optoelectronics Conference (IMOC)*, Porto de Galinhas, 2015, pp. 1-5.

6. T. Franke, A. Gaebler, **A. E. Prasetiadi** and R. Jakoby, "Tunable Ka-band waveguide resonators and a small band band-pass filter based on liquid crystals," *44th European Microwave Conference*, Rome, 2014, pp. 339-342.
7. W. Hu, O. H. Karabey, A. Gäbler, **A. E. Prasetiadi**, M. Jost and R. Jakoby, "Liquid crystal varactor loaded variable phase shifter for integrated, compact, and fast beamsteering antenna systems," *9th European Microwave Integrated Circuit Conference*, Rome, 2014, pp. 660-663.
8. M. Jost, C. Weickhmann, S. Strunck, A. Gaebler, W. Hu, T. Franke, **A. E. Prasetiadi**, O. H. Karabey and R. Jakoby "Electrically biased W-band phase shifter based on liquid crystal," *39th International Conference on Infrared, Millimeter, and Terahertz waves (IRMMW-THz)*, Tucson, AZ, 2014, pp. 1-2.
9. W. Hu, O. H. Karabey, **A. E. Prasetiadi**, M. Jost and R. Jakoby, "Temperature Controlled Artificial Coaxial Line for Microwave Characterization of Liquid Crystal," *GeMiC 2014 - German Microwave Conference*, Aachen, Germany, 2014, pp. 1-4.

Poster Presentation

1. T. Franke, R. Follmann, D. Köther, T. Kässer, T. Rabe, A. Heunisch, A. Gäbler, **A. E. Prasetiadi**, and R. Jakoby, "LIQUIDA-Sky Project: Electronically Tunable Filters for K-Band Satellites based on Microwave Liquid Crystal Technology," *4. Nationale Konferenz - Satellitenkommunikation in Deutschland*, Bonn, Germany, Feb. 2015.

Workshop

1. **A. E. Prasetiadi**, T. Franke and R. Jakoby, "Electronically Tunable Filters based on Microwave Liquid Crystal Technology" workshop at the *European Microwave Conference*, Paris, Sep. 2015.

AWARD

1. Nomination for Young Engineer Prize, European Microwave Conference 2017 (Top 10%).

SUPERVISED THESIS

1. S. Rahmawati, ”Investigation of Electrical Biasing Schemes for Substrate Integrated Waveguide (SIW) Tunable Devices Based on Liquid Crystal (LC) Technology,” Master Thesis (D 2235-M), Technische Universität Darmstadt, Darmstadt, Germany, 2015.

CURRICULUM VITAE

Personal Information:

Name	Ananto Eka Prasetiadi
Date of birth	30.12.1989
Place of birth	Palo Alto, CA, USA
Nationality	Indonesian

Education:

2004–2006	High school education, SMA Labschool Kebayoran, Jakarta, Indonesia
2006–2010	Bachelor degree in Telecommunication Engineering, Institut Teknologi Bandung, Bandung, Indonesia
2010–2011	Master degree in Electrical Engineering, Institut Teknologi Bandung, Bandung, Indonesia
2012–2017	Research assistant at Institut für Mikrowellentechnik und Photonik, Technische Universität Darmstadt, Darmstadt, Germany

Darmstadt, 20.06.2017

Ananto Eka Prasetiadi